

# Probing matter created at RHIC heavy-ion collisions by di-muons and photons at mid and forward rapidities.

*By*

**Arindam Roy**

**Enrollment No. PHYS04201004007**

*Variable Energy Cyclotron Centre, Kolkata*

*A thesis submitted to*

*The Board of Studies in Physical Sciences*

*In partial fulfillment of requirements for the Degree of*

**DOCTOR OF PHILOSOPHY**

*of*

**HOMI BHABHA NATIONAL INSTITUTE  
Bhabha Atomic Research Centre  
Mumbai-400085, India**



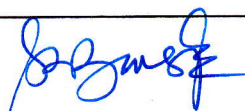
January, 2016

# Homi Bhabha National Institute<sup>1</sup>

## Recommendations of the Viva Voce Committee

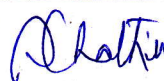
As members of the Viva Voce Committee, we certify that we have read the dissertation prepared by Mr. Arindam Roy entitled "Probing matter created at RHIC heavy-ion collisions by di-muons and photons at mid and forward rapidities" > and recommend that it may be accepted as fulfilling the thesis requirement for the award of Degree of Doctor of Philosophy.

Chairman – Prof. Sudhee Ranjan Banerjee



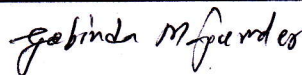
Date: 26/4/2016

Guide / Convener – Prof. Subhasis Chattopadhyay



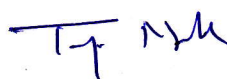
Date: 26/4/2016

Examiner – Prof. Gobinda Majumder



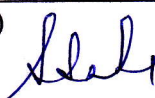
Date: 26/4/2016

Member 1- Prof. Tapan K. Nayak



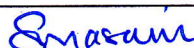
Date: 26/4/2016

Member 2- Prof. Satyajit Saha (SINP)



Date: 26/4/2016

Technology Adviser- Shri S. Ram Narayan



Date: 26/4/2016

Final approval and acceptance of this thesis is contingent upon the candidate's submission of the final copies of the thesis to HBNI.

I/We hereby certify that I/we have read this thesis prepared under my/our direction and recommend that it may be accepted as fulfilling the thesis requirement.

Date: 26/4/2016

Place: VECC-KOLKATA

Co-guide (if applicable)

  
Guide

<sup>1</sup> This page is to be included only for final submission after successful completion of viva voce.

## STATEMENT BY AUTHOR

This dissertation has been submitted in partial fulfillment of requirements for an advanced degree at Homi Bhabha National Institute (HBNI) and is deposited in the Library to be made available to borrowers under rules of the HBNI.

Brief quotations from this dissertation are allowable without special permission, provided that accurate acknowledgement of the source is made. Requests for permission for extended quotation from or reproduction of this manuscript in whole or in part may be granted by the Competent Authority of HBNI, when, in his or her judgment, the proposed use of the material is in the interests of scholarship. In all other instances, however, permission must be obtained from the author.

*Arindam Roy*  
Arindam Roy

## DECLARATION

I, hereby declare that the investigation presented in the thesis has been carried out by me. The work is original and has not been submitted earlier as a whole or in part for a degree/diploma at this or any other Institution/University.

Arindam Roy  
Arindam Roy



# List of Publications arising from the thesis

## In peer-reviewed Journal

1. “Calibration and performance of the STAR Muon Telescope Detector using cosmic rays”  
Yang C. et al for the STAR Collaboration  
[Nucl. Instrum. Meth. A762 \(2014\) 1](#) , [arXiv:1402.1078]
2. “Development of Multi-gap Resistive Plate Chamber (MRPC) for medical imaging”  
A. Banerjee, **A. Roy**, S. Biswas, S. Chattopadhyay, G. Das, S. Pal.  
[Nucl. Instrum. Meth. A718, 138 \(2013\)](#) , [arXiv:1408.0280]
3. “Performance simulation of a MRPC-based PET Imaging System”  
**A. Roy**, A. Banerjee, S. Biswas, S. Chattopadhyay, G. Das, S. Saha.  
[2014 JINST 9 C10030](#)
4. “Charged-to-neutral correlation at forward rapidity in Au+Au collisions at  $\sqrt{s_{NN}}=200$  GeV”  
Prithwish Tribedy , **Arindam Roy**, Subhasis Chattopadhyay as primary authors for the STAR Collaboration  
[Phys. Rev. C. 91, 034905 \(2015\)](#) , [arXiv:1408.5017]

## Conferences and Symposia

1. “Detection of Gamma rays with Multigap Resistive Plate Chamber”  
**A. Roy**, A. Banerjee, S. Biswas, S. Chattopadhyay, G. Das, S. Saha.  
[Proceedings of the DAE Symp. on Nucl. Phys. 59 \(2014\)](#)

# Acknowledgement

I express my sincerest gratitude towards my supervisor, Prof. Subhasis Chattopadhyay for his supervision, training and constant motivation. I thank you Sir, for your patience, enthusiasm and encouragement. My heartfelt thanks to Mr. S. Ramnarayan for his valuable time, immense patience and his constant motivation and encouragement. I have learnt a lot from you. I am grateful to Prof. Y. P. Viyogi for his encouragement and valuable suggestions. I take this opportunity to thank my seniors Dr. Saikat Biswas, Dr. Prithwish Tribedy and Mr. Arnab Banerjee for teaching me, guiding me and inspiring me throughout the course of this work. Thank you all for your valuable time, your support and for sharing your knowledge and experiences with me. I am indebted to Dr. Lijuan Ruan for her guidance and support and the valuable discussions. Special thanks to the entire STAR-MTD group, especially Dr. Rongrong Ma, Dr. Bingchu Huang, Shuai Yang and Xinjie Huang for sharing their knowledge and insights with me. I am grateful to Prof. D. K. Srivastava for giving me the opportunity to pursue my PhD at VECC. I am grateful to Prof. Tapan K. Nayak, Dr. Zubayer Ahammed, Dr. Susanta Pal, Dr. Anand K. Dubey, Dr. Partha Pratim Bhaduri, Mr. Sanjib Muhuri, Dr. Premomoy Ghosh, Mr. Jogendra Saini, Mr. Partha Bhaskar and Mr. Vikas Singhal for teaching me and for their valuable suggestions and discussions. I am truly indebted to Mr. Ganesh Das for his help and support throughout this work. I also thank Mr. Partha Dhara for his constant help. I thank my seniors Mr. Amal Sarkar, Dr. Mriganka M. Mondal, Dr. Subhash Singha, Dr. Chanaka De Silva and Mr. Shikshit Gupta for their immense help during my stay at BNL. I thank all my labmates at VECC. Thank you Kshitij, Ekata, Vivek Ji and Shaifali. I thank all my juniors at VECC for their help. I would like to thank Mr. Jayant Kumar for his constant help. I acknowledge the computing facilities of RCF at BNL, grid-peer Kolkata at VECC. None of this would have been possible without the constant, unwavering support of my family and friends. I do not have any words to thank my mother and sister. Without your immense love, sacrifice, patience, support and motivation I would not have come this far. My friends Balaram, Rajesh, Subikash and Sumit (named in alphabetical order) have been a constant source of enthusiasm and inspiration in my life. Thank you for all your help and support on and off the court.

# Contents

<b>Synopsis</b>	<b>8</b>
<b>List of Figures</b>	<b>13</b>
<b>List of Tables</b>	<b>21</b>
<b>1 Introduction</b>	<b>22</b>
1.1 Heavy Ion collisions at the Relativistic Heavy Ion Collider . . . . .	22
1.1.1 Signatures of the QGP phase . . . . .	24
1.2 Probing the matter created at RHIC with di-muons . . . . .	28
1.3 Probing the matter created at RHIC with photons . . . . .	30
1.4 Outline of this thesis work . . . . .	33
<b>2 Heavy Ion Collision Experiments at RHIC</b>	<b>40</b>
2.1 The Relativistic Heavy Ion Collider . . . . .	40
2.2 The Accelerators . . . . .	41
2.3 The STAR experiment . . . . .	45
2.3.1 The Time Projection Chamber – TPC . . . . .	47
2.3.2 The Time-Of-Flight detector – TOF . . . . .	50
2.3.3 The Photon Multiplicity Detector – PMD . . . . .	53
2.3.4 The Forward Time Projection Chamber – FTPC . . . . .	56
2.3.5 The Muon Telescope Detector – MTD . . . . .	57
2.3.6 Simulation results for the STAR-MTD . . . . .	58
2.3.7 Physics potential with the MTD . . . . .	61
<b>3 Development of Multi-gap RPCs (MRPC) for the STAR experiment</b>	<b>67</b>
3.1 Gaseous ionization detectors . . . . .	67
3.2 Evolution of the Parallel Plate Design in Gas detectors . . . . .	72
3.2.1 The Keuffel Spark Counter . . . . .	73
3.2.2 The Pestov Spark Counter (PSC) . . . . .	73
3.2.3 Parallel Plate Avalanche Chamber . . . . .	74
3.3 Resistive Plate Chamber (RPC) . . . . .	75
3.3.1 Choice of the Fill gas used in RPC's . . . . .	78
3.3.2 Avalanche Multiplication and Signal generation in RPC . . . . .	79

3.3.3	Modes of operation . . . . .	82
3.3.4	The advent of the Multi-gap RPC (MRPC) . . . . .	85
3.3.5	Applications of Resistive Plate Chambers - single gap and multi-gap . . . . .	88
3.4	Fabrication of 5-gap Glass MRPC modules at VECC for the STAR-MTD . . . . .	89
3.5	Test results of the MTD-MRPC modules at VECC with cosmic rays . . . . .	100
3.6	Cosmic ray Test results of the MTD-MRPC modules at STAR . . . . .	104
3.7	Detection of 511 keV photons with MRPC's as a proof-of-principle for TOF-PET . . . . .	108
3.7.1	Introduction . . . . .	109
3.7.2	Advantages of Time-of-Flight in PET . . . . .	111
3.7.3	Advantages of RPC's for use in PET . . . . .	113
3.7.4	Limitations of RPC-PET . . . . .	114
3.7.5	Fabrication and testing of the six-gap MRPC prototype . . . . .	115
3.7.6	Experimental Results with the 6-gap MRPC prototype . . . . .	116
3.7.7	Fabrication and testing of the two-MRPC coincidence system . . . . .	118
3.7.8	Preliminary timing resolution measurement . . . . .	119
3.8	Conclusions and Outlook . . . . .	121
<b>4</b>	<b>Charged-neutral correlation Analysis at forward rapidity</b>	<b>127</b>
4.1	Introduction . . . . .	127
4.2	Method of analysis . . . . .	128
4.2.1	Choice of suitable observables for ch- $\gamma$ correlation . . . . .	130
4.2.2	Detectors used for the analysis . . . . .	132
4.2.3	Datasets and Kinematic Cuts for the BES energies . . . . .	134
4.2.4	Quality Assurance (QA) plots and Run-by-Run QA for the BES energies . . . . .	135
4.2.5	Correction of the Bin-width effect . . . . .	141
4.2.6	Error Analysis . . . . .	143
4.2.7	Limitations of the ch- $\gamma$ correlation analysis . . . . .	145
4.3	Results for Au+Au collisions at $\sqrt{s_{NN}} = 200$ GeV and at BES energies . . . . .	146
4.4	Conclusions . . . . .	156
<b>5</b>	<b>Results and Discussions</b>	<b>164</b>
5.1	Fabrication and testing of Multi-gap Resistive Plate Chambers (MRPC) for the STAR-MTD project . . . . .	165
5.2	Charged-neutral ( $\gamma$ ) correlation analysis for the STAR experiment . . . . .	166
5.3	Use of MRPC for TOF-PET (Time-of-Flight Positron Emission Tomography) . . . . .	169

# Synopsis

The primary physics objective of the Relativistic Heavy Ion Collisions is to create and explore primordial matter that is believed to have existed at the early stages of the Universe, less than a few microseconds after the Big Bang. According to the predictions of Quantum Chromodynamics (QCD), at high temperature and densities expected to be achieved at the RHIC and the LHC heavy ion collisions, a new phase of de-confined matter commonly known as Quark Gluon Plasma (QGP) can be experimentally created in the laboratory. Measurements at RHIC over more than a decade have set forth compelling evidences of the formation of a strongly coupled QGP.

When two Lorentz-contracted heavy ion nuclei travelling at relativistic speeds are smashed with each other, it leads to the creation of a hot and dense fireball with an extremely short lifetime. The fireball is a region of space of nuclear dimensions ( $\sim 10$  fm) characterised by enormous temperature and energy density ( $\sim 300$  MeV and  $5$  GeV/fm<sup>3</sup> for central Au+Au collisions at  $\sqrt{s_{NN}} = 200$  GeV). This fireball eventually thermalizes to form a medium where the relevant degrees of freedom are asymptotically free quarks and gluons. This new state of matter in which quarks and gluons are deconfined over nuclear dimensions and show an overall color neutrality is called the Quark Gluon Plasma. The deconfined matter expands in volume and cools rapidly, followed by a cross-over phase transition to hadronic matter. The hadrons finally stream towards the detectors without any further interactions. Each such collision results in the formation of several hundred produced particles at the final stage where specialised detectors play the crucial role of detection and identification of the particles along with the measurement of their properties to gather information about the various stages of heavy-ion collisions.

The STAR (Solenoidal Tracker at RHIC) experiment is one of the four experiments at RHIC, designed to search for the existence of QGP and to study its properties. The experimental study of QGP includes the detection of the products of heavy-ion collisions and understanding the underlying mechanisms using suitable observables constructed out of the properties of the detected particles. This thesis is mainly aimed at exploring the matter created at RHIC heavy-ion collisions using probes at mid and forward rapidities. At mid-rapidity, I have worked on the detection of di-muons, with the emphasis on building a muon detector as an upgrade of STAR. Data taking is ongoing with this detector. At forward rapidity, correlations between charged particles and photons have been studied at various collision energies. The two topics are expanded briefly below :

- Development, fabrication and testing of Multigap Resistive Plate Chambers (MRPC) as detecting elements of MTD – the Muon Telescope Detector at STAR.

The objective of the STAR - MTD is the detection of di-muons using precise timing and hit position measurement. The MRPC modules have been installed at STAR and the MTD is taking data at present. This thesis includes details of the fabrication and testing of the MRPC modules.

- Measurement of Correlations between charged and neutral particle multiplicities at forward rapidity using STAR data.

The Photon Multiplicity Detector (PMD) and the Forward Time Projection Chamber (FTPC) , two detectors at the forward rapidity region at STAR measure photons and charged particles respectively. Data taken at a wide range of energies for studying the correlations of the mutiplicities of charged and neutral particles have been analysed. The correlations give useful information about isospin fluctuations on an event-by-event basis that might shed light on the nature of the QCD chiral phase transition.

**Development, fabrication and testing of MRPCs as detecting elements of the**



## STAR-MTD

Muons being weakly interacting, remain unaffected by the strongly interacting medium and act as one of the cleanest probes to study QGP. The objective of the MTD upgrade for the STAR experiment is to study the di-muon spectra at mid-rapidity at different mass regions. Muons are advantageous over electrons and photons as they have significantly reduced backgrounds from hadronic decays,  $\pi^0$  and  $\eta$  Dalitz decays and gamma conversions in materials. The STAR detector is capable of triggering and detecting di-electrons coming from  $J/\psi$  at mid-rapidity using a combination of the Time Projection Chamber (TPC) , Time-Of-Flight (TOF) and Barrel Electromagnetic Calorimeter (BEMC) detectors. The limitations to this measurement come from large backgrounds in case of electrons and the lack of effective triggering especially at low transverse momentum ( $p_T$ ). The capability of the STAR-MTD to provide a high efficiency and excellent triggering for di-muons from  $J/\psi$  over a large acceptance at mid-rapidity is expected to help us understand the color screening properties of the medium better with the increased number of detected  $J/\psi$  samples. The higher muon mass ensures less Bremsstrahlung radiation loss in detector material budget. This improves the invariant mass resolution, previously unachievable with electrons and helps in separating the different  $\Upsilon$  states (1S, 2S, 3S). This feature of the MTD can help us to determine the temperature of the QGP medium.

Conventional Muon detectors used in other high energy physics experiments rely upon tracking stations, trigger detectors and absorbers. In case of the MTD, the STAR magnet backlegs act as the absorber and the tracks from the TPC projected onto the MRPCs – known for their excellent timing and position resolutions – are used for muon identification. The requirement for the MTD physics goals have been estimated to be  $<100$  ps in timing and  $\sim 1$  cm in position resolution for identifying muons having a few GeV/c momentum. Installation of the proposed 122 five-gap MRPC modules for the STAR MTD at mid-rapidity ( $|\eta| < 0.5$ ) has been completed successfully in 2014, covering 45% in azimuth over a large area. Ten such MRPC modules ( $\sim 10\%$  of the total modules for the STAR - MTD) of dimensions  $87\text{ cm}(z) \times 52\text{ cm}(\phi)$  and  $250\text{ }\mu\text{m}$  gas gaps have been fabricated at VECC, Kolkata, India. The modules have been tested in the

avalanche mode with a gas mixture of Freon (R-134A) and Iso-butane ( $i-C_4H_{10}$ ) in the volume ratio of 95 : 5. The modules have double-ended, 3.8 cm wide readout PCB strips with 0.6 cm gaps in between. A timing resolution  $<100$  ps and a spatial resolution of  $\sim 1$  cm, which are suitable for the MTD physics goals have been measured in cosmic ray tests and with test beams. The testing and characterization, including detector seasoning, data taking on efficiency, noise rate, charge spectra and timing resolution measurement of the modules have been performed as a part of this thesis work.

As a spin-off benefit of the Detector development for STAR, parallel R & D with similar detectors (MRPC) have been undertaken for Positron Emission Tomography (PET) Imaging. The time-of-flight PET (TOF-PET) Imaging system using MRPCs helps in localising the annihilation point and improves the image quality. Several glass-based, small sized MRPC's have been fabricated and a system of 511 keV photon-pair detection using a  $^{22}\text{Na}$  source has been setup. The setup has a plastic scintillator on one side and a six-gap MRPC on the other side to detect the pair of coincident photons coming from the  $^{22}\text{Na}$  source. The efficiency and timing resolution of the detection of the pair of 511 keV photons has been measured. The scintillator and MRPC setup detected a clear signal of photon pairs with the  $^{22}\text{Na}$  source, above background.

### **Measurement of Correlations between charged and neutral particle multiplicities at forward rapidity using STAR data.**

The phase transition from QGP to Hadron Gas is associated with the confinement and the chiral phase transitions. During QCD chiral phase transition, theoretical predictions indicate that there could be formation of metastable domains of disoriented chiral condensate (DCC). Generic production of pions leads to equal abundance of pions of different isospin. The formation and decay of DCC domains result in anomalous production of pions of a certain isospin, in contrast to the generic production of pions. The correlation of the multiplicity of measured charged particles (representing charged pions) and decay photons (representing neutral pions), serves as an indirect probe of the QCD chiral phase transition. This thesis discusses the mea-

surement of event-by-event correlations between photons and charged particle multiplicities in the pseudo-rapidity range  $-3.7 < \eta < -2.8$ , using the two forward detectors, the PMD and the FTPC respectively. This measurement has been done for the RHIC Beam Energy Scan (BES) data over an energy range of 19.6 to 200 GeV. This analysis presents a measurement of charged - neutral correlations over the wide range of energies (200 GeV-19.6 GeV) which is a first such effort at RHIC. As a part of this thesis, extensive cleanup of the datasets have been performed, error analysis and model calculations have been done. A detailed study on the choice of suitable observables for this analysis have also been performed. The objective of this analysis is to find possible evidences of dynamical charged-neutral correlations and look for deviation from expectation based on a generic pion production model. Comparison of charged-neutral correlations with net-charge correlations for all energies have also been performed. It has been concluded using two observables called  $\nu_{dyn}$  and  $r_{m,1}$ , that the amount of correlation observed between charged and neutral particles at the top RHIC energy is beyond model predictions. It has been seen that charged-neutral correlation differs from net-charge correlation both in sign and magnitude. The energy, collision centrality and charge dependence of charged-neutral correlation for the energies 200, 62.4, 39, 27, 19.6 GeV have been studied and details will be presented in this thesis.

# List of Figures

1.1	A schematic diagram showing the collision of two Lorentz-contracted nuclei and the subsequent evolution of the collision [6] . . . . .	23
1.2	The space-time evolution of a heavy-ion collision [7] . . . . .	24
1.3	Schematic diagram highlighting the di-muon (dilepton) production sources as a function of the di-muon (dilepton) invariant mass in heavy ion collisions [35]. . .	29
1.4	Metastable DCC domains characterised by a misalignment of the four-component ( $\sigma, \pi$ ) chiral condensate relative to its true vacuum orientation during chiral phase transition [30]. . . . .	32
2.1	Aerial view of the RHIC complex . . . . .	41
2.2	A schematic showing the locations of the 4 different experiments and the accelerators at RHIC [8]. . . . .	42
2.3	A schematic showing the acceleration scheme for Au ion beams at RHIC [9]. . . .	43
2.4	A schematic of the QCD phase diagram taken from the reference [13]. . . . .	44
2.5	The STAR detector and its subsystems. This is an old picture of the experimental setup from the year 2012 taken from Ref. [15], where most of the subsystems are shown together. Detector R&D and installation has been completed for all subsystems. The PMD detector has been dismantled in the year 2011. The FGT replaced the FTPC detector in 2012. . . . .	45
2.6	The co-ordinate system of the STAR experiment [16] . . . . .	46

2.7	The STAR Time Projection Chamber [17] . . . . .	48
2.8	The TPC Anode pad plane showing the inner and outer sectors [17]. . . . .	49
2.9	The geometry of the TOF detector, including readout pad design taken from reference [22] . . . . .	51
2.10	Particle identification performance of the first 5 TOF MRPC trays during RHIC p+p collisions in 2008 [23]. . . . .	53
2.11	The STAR Photon Multiplicity Detector [24]. . . . .	54
2.12	Working principle of the Photon Multiplicity Detector . . . . .	55
2.13	The STAR Forward Time Projection Chamber [27] . . . . .	56
2.14	Location of the STAR MTD [32] . . . . .	58
2.15	Schematic diagram of a 5-gap MRPC module for the STAR-MTD . . . . .	59
2.16	Simulation of central Au+Au collisions in the framework of the STAR geometry and material budget using the HIJING event generator [32] . . . . .	60
2.17	Detection efficiency for muons compared to the probability of misidentification for pions, kaons and protons [32]. . . . .	61
2.18	$J/\psi$ efficiency as a function of $p_T$ at mid-rapidity using the di-electron decay channel at PHENIX [36] and STAR [32] . . . . .	62
2.19	Signal to background ratio for the $J/\psi$ invariant mass distribution obtained from simulation [32]. . . . .	63
2.20	Simulation result highlighting the separation of the different $\Upsilon$ states using the di-muon decay channel [32]. . . . .	63
3.1	Modes of operation of gas detectors, in terms of the number of ions collected as a function of the applied voltage [3]. . . . .	70
3.2	Schematic diagram of the Pestov Spark Counter [14]. . . . .	74
3.3	Schematic diagram of a basic Resistive Plate Chamber taken from [8] . . . . .	76
3.4	Illustration of the difference in avalanche growth and signal generation between a) a cylindrical wire chamber and b) a parallel plate detector [14] . . . . .	77

3.5	Schematic diagram of a liquid-drop shaped avalanche [25]. . . . .	80
3.6	Charge development in a 2 mm gap RPC with the avalanche multiplication starting at two different positions a) the avalanche starts at $x = 0$ and traverses the entire 2 mm gas gap and b) the avalanche creation is at $x = 0.5$ mm from the cathode and travels 1.5 mm in the gas gap [14] . . . . .	81
3.7	Avalanche development in an RPC detector a) Primary ionization of gas atoms by through-going radiation culminating in a Townsend Avalanche in an electric field $E_0$ b) Avalanche dynamics starting to influence the electric field c) Owing to the large differences in mass, electron drift velocity is considerably higher than ions and the electrons and ions reach respective electrodes at different times. d) When ions finally reach the cathode, the discharge affects a small area of the electrodes due to its high resistivity, around the region of avalanche development [8]. . . . .	82
3.8	Development of a streamer in an RPC a) A townsend avalanche developing after the passage of radiation b) At such high values of gas gain, enormous charge in the sensitive volume of the detector modifies the external electric field strongly. Photons also play a major role in spreading the avalanche and streamer evolution c) Formation of a conductive channel between the electrodes leads to sparks and discharge of wider regions of the electrodes d) The discharge causes a reduction of the electric field at the avalanche spot creating a dead area [8]. . . . .	84
3.9	Schematic diagram of a Multi-gap RPC [14] . . . . .	86
3.10	A schematic diagram of the Type B MRPC. The different components used for detector fabrication have been highlighted in different colors. Honeycomb boards are in yellow, Read-out strips are in red, Printed Circuit Boards (PCB) are shown in green, the Mylar insulating foil is colored light yellow while the glass plates are sky blue in color. Diagram not to scale. The vertical dimension has been enhanced to get a clear view [51]. . . . .	90



3.11 A flowchart summarising the fabrication procedure of the MTD-MRPC modules at VECC. . . . .	91
3.12 Printed Circuit Board (PCB) with metallic (Cu) readout strips. . . . .	92
3.13 Putting the double-sided tape on the honeycomb board before attaching the PCB board to it. . . . .	93
3.14 PCB pasted on the honeycomb boards with double-sided tape. . . . .	93
3.15 Old design with a part of the Mylar foil at the edge completely removed. This led to improper insulation and arcing of the glass electrodes. The process was subsequently discontinued. . . . .	94
3.16 New Mylar design with just a small gap for graphite tape. . . . .	94
3.17 Graphite electrode placed on the bottom honeycomb board. . . . .	95
3.18 Cleaning of the bottom electrode with a spray gun. The nylon screws and spacers are also in position. . . . .	95
3.19 250 $\mu\text{m}$ nylon monofilament fishing line defining one of the gas gaps on a glass plate . . . . .	96
3.20 A Nylon screw holding the fishing lines in position for the 5 gas gaps. The picture shows all the components in place, from the bottom honeycomb board and PCB and the (outer and inner) glass plates, to the nylon screw and the fishing line. . .	96
3.21 A completed module with the twisted pair cables connected. . . . .	97
3.22 The module is placed in the ingeniously built, gas-tight Aluminium box for testing.	97
3.23 Gas mixing and distribution system. . . . .	98
3.24 Summarising the components required for the fabrication of a MTD-MRPC module including their dimensions and respective quantities. . . . .	99
3.25 V-I characteristic of VECC MTD-MRPC module #9 as a function of high voltage.	100
3.26 Electrical equivalent circuit diagram of a glass RPC gas gap [6] . . . . .	101
3.27 A schematic diagram showing the cosmic ray trigger scheme for the MRPC test.	102
3.28 Efficiency of VECC MTD-MRPC module #9 as a function of high voltage. . . .	103

3.29 Strip-by-strip noise rate variation of the VECC MTD-MRPC module #9 at the operating voltage of $\pm 6300$ Volts. . . . .	103
3.30 Strip-by-strip noise rate measurement of the VECC MTD-MRPC module #9 at the operating voltage of $\pm 6300$ Volts at UT Austin. . . . .	105
3.31 A correlation plot showing the noise correlation of the VECC MTD-MRPC module #9 at the operating voltage of $\pm 6300$ Volts at UT Austin. . . . .	105
3.32 Schematic representation of a cosmic ray event at STAR [51] . . . . .	106
3.33 The $\Delta Z$ distribution shown in the left panel and the $\Delta\phi$ distribution show in the right panel. The standard deviation of the Gaussian fits (solid curves) gives the detector spatial resolution [51]. . . . .	107
3.34 Timing Resolution . . . . .	108
3.35 Factors degrading PET resolution a) Random coincidences, b) Compton scattering of the photons c) Effect of Parallax error [57]. . . . .	109
3.36 a) The positron emitted by the administered radionuclide emits two coincident back-to-back 511 keV gamma rays upon annihilation with an electron. The arrival time difference of the photons ( $t_2-t_1$ ) helps localize the annihilation event along the line of response (LOR) joining the two detectors X and Y, b) Event reconstruction using TOF information is done within a reduced back-projected region ( $\Delta L$ ) of the LOR determined by the system time resolution [56]. . . . .	112
3.37 Experimental Set-up for testing the prototype MRPC with the $^{22}\text{Na}$ source [69][70].	115
3.38 The coincidence count rate as a function of the high voltage [69][70]. . . . .	116
3.39 The pair detection efficiency as a function of the high voltage [69][70]. . . . .	117
3.40 Calculated and measured time difference as a function of source distance [69][70].	118

3.41	Steps of fabrication of the 18 cm $\times$ 18 cm prototype MRPC module a) The graphite coated electrode is placed on the frame made of “Perspex”. The nylon screws are placed to define the gas gaps and the provision for the application of High Voltage has also been made. b) The 250 $\mu$ m fishing line is used to define the gas gap c) Four inner glass plates are subsequently stacked and the outer electrode is placed at the top d) The top part of the frame is placed and the complete gas-tight module is then flushed with gas, ready to be operated in the avalanche mode. . . . .	119
3.42	The two-MRPC coincidence setup for testing the detector timing resolution. . . .	120
3.43	Timing resolution measured with Scintillator 3-fold as TDC-Start and delayed detector logic pulse as TDC-Stop. The error bars are within marker size. . . . .	121
4.1	A schematic diagram of the common PMD-FTPC acceptance for the measurement of $\gamma$ -ch correlation. . . . .	133
4.2	QA plots for $\sqrt{s_{NN}} = 62.4$ GeV . . . . .	136
4.3	QA plots for $\sqrt{s_{NN}} = 39$ GeV . . . . .	137
4.4	QA plots for $\sqrt{s_{NN}} = 27$ GeV . . . . .	138
4.5	QA plots for $\sqrt{s_{NN}} = 19.6$ GeV . . . . .	139
4.6	Run-by-Run QA plots for $\sqrt{s_{NN}} = 19$ GeV . . . . .	140
4.7	Run-by-Run QA plots for $\sqrt{s_{NN}} = 27$ GeV . . . . .	141
4.8	Run-by-Run QA plots for $\sqrt{s_{NN}} = 39$ GeV . . . . .	142
4.9	Run-by-Run QA plots for $\sqrt{s_{NN}} = 62.4$ GeV . . . . .	143
4.10	The observable $\nu_{\text{dyn}}$ and the three individual terms plotted as a function of the multiplicity variable in the acceptance of interest $\sqrt{\langle N_{\text{ch}} N_{\gamma} \rangle}$ at $\sqrt{s_{NN}} = 200$ GeV. The statistical and systematic uncertainties are represented by vertical lines and boxes respectively. For model calculations, the statistican uncertainties are represented by bands [8]. . . . .	147

4.11	Measurement of $\nu_{dyn}^{\gamma\text{-ch}}$ from charged particles and photons at $\sqrt{s_{NN}} = 200$ GeV in the same pseudorapidity range $-3.7 < \eta < -2.8$ (same side) is compared to photons measured in the range $-3.7 < \eta < -2.8$ and charged particles measured in the range of $2.8 < \eta < 3.7$ (away-side). Values of $\nu_{dyn}^{\gamma\text{-ch}}$ measured for the same side are significantly different for data and model calculations, whereas, $\nu_{dyn}^{\gamma\text{-ch}}$ values for the away side are in good agreement, ruling out detector effects as the reason and hinting strongly at dynamical origin [8]. . . . .	148
4.12	$\omega_\gamma$ as a function of multiplicity at all energies ( $\sqrt{s_{NN}} = 200$ GeV - 19 GeV). The statistical error is shown by vertical lines and systematic error is represented by boxes. . . . .	149
4.13	$\omega_{ch}$ as a function of multiplicity at all energies. The statistical error is shown by vertical lines and systematic error is represented by boxes. . . . .	150
4.14	$\text{corr}_{\gamma\text{-ch}}$ as a function of multiplicity at all energies. The statistical error is shown by vertical lines and systematic error is represented by boxes. . . . .	150
4.15	A comparison plot of the multiplicity dependence of the observable $\nu_{dyn}^{\gamma\text{-ch}}$ as a function of the multiplicity term $\sqrt{\langle N_{ch} N_\gamma \rangle}$ in the acceptance of interest at all energies. The statistical error is shown by vertical lines and the systematic error is represented by boxes. . . . .	151
4.16	Charge dependence of the observable $\nu_{dyn}$ at $\sqrt{s_{NN}} = 200$ GeV as a function of multiplicity. The correlation between the charged particles and photons have been measured using the FTPC and PMD detectors in the pseudorapidity region $-3.7 < \eta < -2.8$ . The statistical uncertainties have been represented by vertical lines while systematic uncertainties have been represented by boxes [8]. . . . .	152
4.17	Charge dependence of the observable $\nu_{dyn}$ for $\sqrt{s_{NN}} = 62$ GeV as a function of multiplicity. . . . .	153
4.18	Charge dependence of the observable $\nu_{dyn}$ for $\sqrt{s_{NN}} = 39$ GeV as a function of multiplicity. . . . .	154

4.19	Charge dependence of the observable $\nu_{\text{dyn}}$ for $\sqrt{s_{NN}} = 27$ GeV as a function of multiplicity. . . . .	154
4.20	Charge dependence of the observable $\nu_{\text{dyn}}$ for $\sqrt{s_{NN}} = 19$ GeV as a function of multiplicity. . . . .	155
4.21	The first three orders of the observable $r_{m,1}$ ( $m = 1 - 3$ ) as a function of multiplicity at $\sqrt{s_{NN}} = 200$ GeV. Results obtained from real data, mixed-events and simulation results using HIJING and GEANT+HIJING have been compared. Statistical errors are represented by vertical lines and systematic errors are represented by boxes. The statistical errors for simulation results have been represented by bands [8]. . . . .	156
4.22	$r_{m,1}$ plotted as a function of its order $m$ within the multiplicity range $47 < \sqrt{\langle N_{\text{ch}} N_{\gamma} \rangle} < 54$ compared with mixed events , HIJING and GEANT+HIJING results for $\sqrt{s_{NN}} = 200$ GeV [8]. . . . .	157
4.23	$r_{1,1}$ as a function of multiplicity for the BES energies compared to $\sqrt{s_{NN}} = 200$ GeV. . . . .	158
4.24	$r_{2,1}$ as a function of multiplicity for the BES energies compared to $\sqrt{s_{NN}} = 200$ GeV. . . . .	158
4.25	$r_{3,1}$ as a function of multiplicity for the BES energies compared to $\sqrt{s_{NN}} = 200$ GeV. . . . .	159

# List of Tables

4.1	Summary of data sets and different kinematic cuts used in this analysis. . . . .	134
-----	--	-----



# Chapter 1

## Introduction

### 1.1 Heavy Ion collisions at the Relativistic Heavy Ion Collider

The primary objective of Relativistic Heavy Ion Collisions that have been undertaken for the last two decades at dedicated experiments around the world [AGS (BNL, USA), SPS (CERN, Switzerland), RHIC (BNL, USA), LHC (CERN, Switzerland)], is to create and explore primordial matter that is believed to have existed at the earliest stages of the Universe, less than a few microseconds after the Big Bang. According to predictions of Quantum Chromodynamics (QCD), the theory of strong interactions, at high temperature and densities expected to be achieved in heavy ion collisions, a new phase of de-confined matter commonly known as Quark Gluon Plasma (QGP) [1] can be experimentally created in the laboratory. This new state of experimentally created matter with quark and gluon degrees of freedom is analogous to the matter existent at the earliest stages after the creation of the Universe. Measurements at RHIC over the last 15 years have set forth compelling evidences of the formation of a strongly coupled QGP (sQGP) [2–5]. When two Lorentz-contracted heavy ion nuclei travelling at relativistic speeds are smashed with each other, it leads to the creation of a hot and dense fireball with an extremely short lifetime. Figs 1.1 and 1.2 schematically show the different stages of a heavy-ion collision and their space-time evolution.

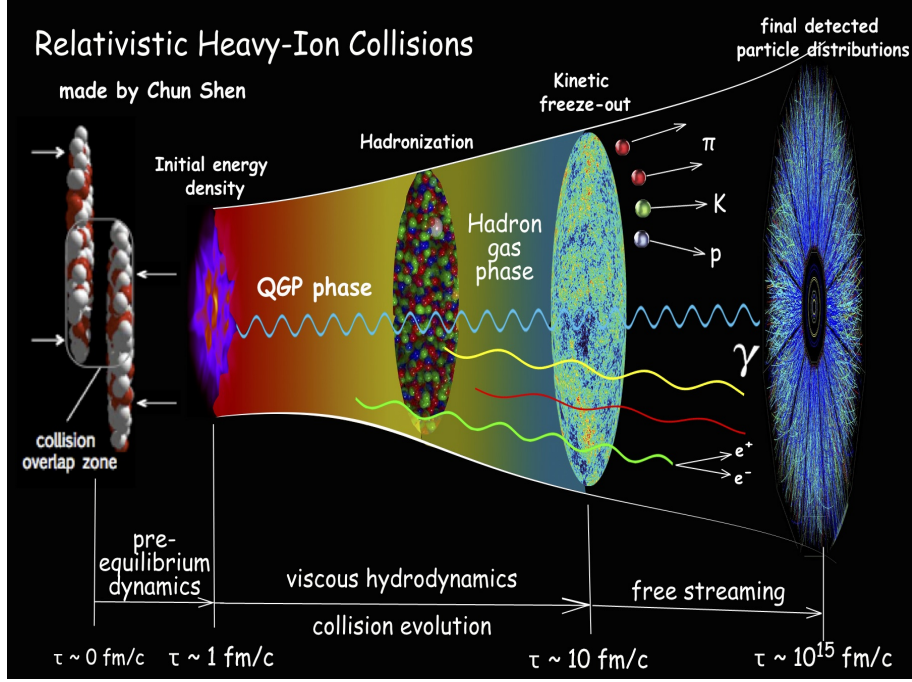


Figure 1.1: A schematic diagram showing the collision of two Lorentz-contracted nuclei and the subsequent evolution of the collision [6]

The process of heavy-ion collisions starts with the collision of the two Lorentz-contracted nuclei at time,  $t=0$ . This leads to the creation of a fireball, which is a region of space of nuclear dimensions ( $\sim 10$  fm), characterised by enormous temperature and energy density ( $\sim 300$  MeV and  $5 \text{ GeV/fm}^3$  for central Au+Au collisions at  $\sqrt{s_{NN}} = 200$  GeV). There are several stages during the evolution of the fireball. The pre-equilibrium stage is characterised by weakly interacting asymptotically free quarks and gluons created due to the deconfinement phase transition. In this extremely short lived stage, the medium has high viscosity due to the large partonic mean free path. The partonic matter eventually cools down and thermalizes to form a medium where asymptotically free quarks and gluons interact strongly and have a short mean free path. This new state of matter in which quarks and gluons are deconfined over nuclear dimensions and shows an overall color neutrality is called the Quark Gluon Plasma. The medium expands in volume and cools rapidly, causing a decrease in the energy density followed by a cross-over phase transition to hadronic matter. At the freeze-out stage, when the interaction between hadrons

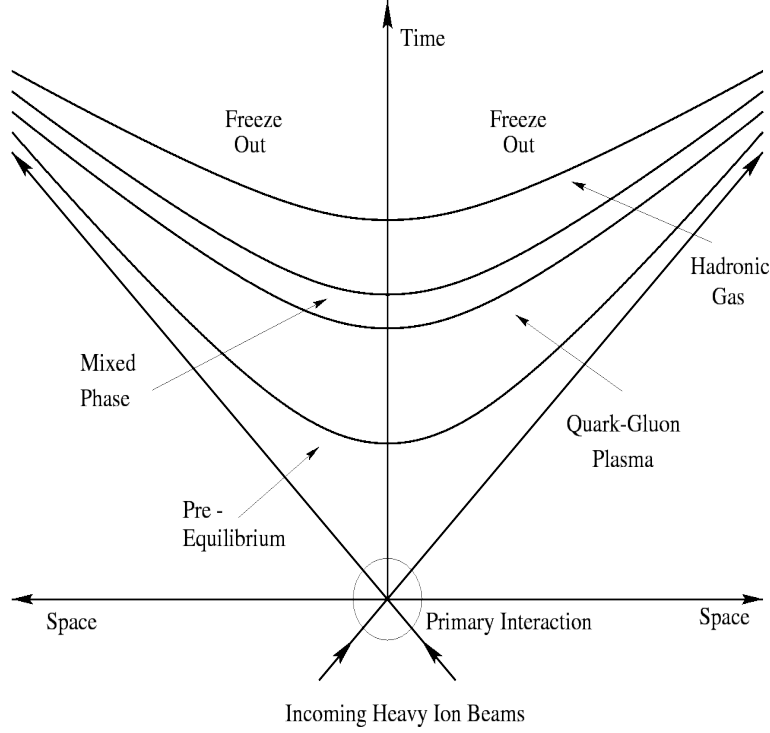


Figure 1.2: The space-time evolution of a heavy-ion collision [7]

ceases to exist, they stream towards the detectors freely. Several hundred particles are produced at the final stage where specialised detectors play the crucial role of detection and identification of the particles along with the measurement of their properties to gather information about the various stages of heavy-ion collisions and to explore the existence of the deconfined stage of matter.

### 1.1.1 Signatures of the QGP phase

- Thermal property of the medium or dilepton/photon emission : Dileptons (lepton pairs:  $e^+, e^-$  and  $\mu^+, \mu^-$ ) and direct photons are excellent probes of the strongly interacting QGP medium [8–13] since they do not take part in strong interactions and hence travel through the medium unaffected. These electromagnetic probes carry sensitive information about the early stages of the collisions. The momentum distribution of the photons are dictated by the temperature of the different constituents of the plasma formed in heavy-ion collisions

[7]. The high momentum region of the photon spectra is predominately due to direct photons produced as a result of hard-parton scattering. The dominant contribution to the intermediate range of the spectra is from photons created in the medium via Compton Scattering, annihilation or Bremsstrahlung radiation, while the lower region comprises mostly of thermal photons from the QGP medium or produced from hadronic matter. The WA98 experiment at the SPS revealed the first measurement of direct photons in central Pb+Pb collisions at 158A GeV. The PHENIX collaboration at RHIC has also reported an excess yield in direct photon spectra in central (0-20%) Au+Au collisions at  $\sqrt{s_{NN}} = 200$  GeV) when results were compared to p+p collisions in the transverse momentum range  $1 < p_T < 4$  GeV/c [14]. A similar trend is also observed in central (0-40%) Pb+Pb collisions at  $\sqrt{s_{NN}} = 2.76$  TeV [15]. The temperature values extracted from exponential fits to the  $p_T$  spectra at RHIC and LHC using the two abovementioned results indicate medium formation at a temperature of  $\sim 300$ -600 MeV [14][15]. Different regimes of the di-lepton invariant mass spectra are sensitive to the various stages of evolution of the medium formed in heavy-ion collisions. Information about the early stages of the heavy-ion collisions are carried by massive di-leptons ( $M > M_{J/\psi}$ ). Dileptons in the intermediate mass range ( $M_{J/\psi} > M > M_\phi$ ) come predominately from QGP emission and carry sensitive information about the thermal properties of the QGP. The low-mass dileptons ( $M < M_\phi$ ) are sensitive to the QCD chiral phase transition. An enhancement in the yields of low mass and intermediate mass dileptons have been observed at SPS energies [16].

- Quarkonia suppression or de-confinement transition of the medium : Quarkonia are the bound states of a quark and anti-quark pair. Quarkonium suppression is one of the signatures of the formation of the QGP phase in heavy-ion collisions [17]. In the presence of the QGP medium, Debye-screening of the quark-antiquark binding potential leads to the dissociation of the quarkonia bound pairs. Since different quarkonium states have different binding energies, their dissociation due to this color screening will be at different temperatures. An understanding of the dissociation pattern can be used to investigate the

temperature and energy density of the medium. Quarkonia yields depend not just on the formation of the QGP medium, but substantially on effects like initial state scattering, finite  $J/\psi$  formation time, regeneration due to recombination effects. A systematic study of dilepton, open charm and charmonium production in p-p, p-A or d-A collisions in addition to A-A collisions is necessary to clearly understand these effects. The NA50 collaboration at SPS was the first to observe  $J/\psi$  suppression in Pb+Pb collisions at  $\sqrt{s_{NN}} = 17.3$  GeV [18]. The nuclear modification factor,  $R_{AA}$  [19] is defined as the ratio of the inclusive yield of hadrons in A-A collisions to the inclusive yield of hadrons in p-p collisions, scaled by the number of binary nucleon collisions. Measurement of  $R_{AA}$  at the LHC in central Pb+Pb collisions at  $\sqrt{s_{NN}} = 2.76$  TeV indicates relatively lower  $J/\psi$  suppression compared to central Au+Au collisions at  $\sqrt{s_{NN}} = 200$  GeV at RHIC [20]. Recent results on quarkonia suppression can be found in Ref.[21].

- Fluid-like property of the medium or Collective motion : A study of the collective motion of the medium formed in heavy-ion collisions can shed light on the nature of the medium and serve as excellent probes of the fluid-like nature of the QGP medium. During the event of a non-central heavy-ion collision, the initial spatial anisotropy is converted to an anisotropy in the transverse momentum space. The co-efficients  $v_n$  of the Fourier decomposition of the distribution of the azimuthal angle of the emitted particles w.r.t the reaction plane are defined as the flow co-efficients. The first two co-efficients  $v_1$  and  $v_2$  are referred to as the directed flow and elliptic flow co-efficients. Results obtained at the Pb+Pb collisions at the SPS [22] and Au+Au collisions at RHIC [23] indicate the presence of radial and elliptic flow in central and non-central collisions respectively. Elliptic flow ( $v_2$ ) values measured at RHIC are 50% higher than the values obtained at SPS energies. The measurement in Pb+Pb collisions at the LHC have also revealed high elliptic flow values. The strong signal of collective motion seen in heavy-ion collisions clearly establishes the fluid-like nature of the medium formed. Constituent quark number scaling of the observed  $v_2$  values at RHIC for mesons and baryons resulted in an universal curve [24] which is

indicative of the deconfined nature of the medium where thermalized quarks undertake collective motion before hadronization [25].

- **Opacity of the medium or Jet quenching :** The suppression of high transverse momentum particles created via hard parton scattering in heavy-ion collisions bears sensitivity to the opacity of the medium. This phenomenon is known as jet quenching and is a direct consequence of the interactions of highly energetic partons with the created medium. The first measurement of jet suppression was in central Au+Au collisions at RHIC at  $\sqrt{s_{NN}} = 130$  GeV [26] and similar results were also obtained in Pb+Pb collisions at  $\sqrt{s_{NN}} = 2.76$  TeV [27] at the LHC. A strong suppression was noticed in hadronic spectra and for particles having transverse momentum  $p_T > 2$  GeV/c, the nuclear modification factor,  $R_{AA}$  turned out to be lower than its baseline value of unity ( $R_{AA} = 1$  indicates the absence of medium formation [28]). A similar measurement in case of d-Au collisions at RHIC at  $\sqrt{s_{NN}} = 200$  GeV failed to reveal any such suppression [29].
- **Correlations and fluctuations:** Sensitive information about the various stages of heavy-ion collisions are reflected in the correlations and fluctuations of the observables used to study heavy-ion collisions. Some of the relevant observables are particle multiplicity, transverse momentum, transverse energy and flow harmonics ( $v_n$ ) [30]. One of the objectives of this thesis is to study the fluctuation of charged-to-neutral pion multiplicities as discussed later. Hence, we have limited this discussion only to multiplicity fluctuations. Fluctuations in inclusive particle multiplicity in the context of heavy-ion collisions arises primarily during the early stages of the collision and during the pre-equilibrium stage. These fluctuations are sensitive to the pre-equilibrium dynamics of the system [30]. The evolution of the medium and the subsequent QCD chiral phase transition introduces event-by-event fluctuations in conserved quantities which is reflected in the form of multiplicity fluctuations of various particle species. In addition to this, resonance decay in the later stages of the collision can also introduce multiplicity fluctuations [30]. Measurement artefacts due to detector



efficiency and acceptance alongwith particle misidentification are some other sources of multiplicity fluctuations [30].

## 1.2 Probing the matter created at RHIC with di-muons

Muons are weakly interacting particles that remain unaffected by the strongly interacting medium that is created in heavy-ion collisions at extreme conditions of temperature and energy density. Muons are produced in all stages of heavy ion collisions [31][32] and are one of the cleanest probes to study heavy-ion collision dynamics and the different properties of the Quark Gluon Plasma (QGP) [33]. The stages of evolution of the fireball created in heavy-ion collisions can be explored by studying the invariant mass spectrum (M) and the transverse momentum of di-muons [35]. Di-muons of different mass are created in different stages of the collision, depending on their invariant mass and transverse momentum. Di-muons of higher invariant mass and transverse momenta are created at the earliest stages of the collision when the system temperature is high, while low mass di-muons are emitted at later stages when the system cools down [35]. In the chirally symmetric, deconfined QGP medium, quarks (q) and anti-quarks ( $\bar{q}$ ) interact among themselves to produce a virtual photon ( $\gamma^*$ ) followed by its decay into a lepton ( $l^+$ ) - anti-lepton ( $l^-$ ) pair, commonly referred to as a dilepton pair [35]. The creation of  $\mu^+$ ,  $\mu^-$  or a di-muon pair is pertinent to the topic of discussion. After the subsequent phase transition into the Hadronic gas phase, di-muons are created from several processes like interactions between opposite pairs of charged hadrons, resonance decays of hadrons ( $\rho$ ,  $\omega$ ,  $\phi$ ,  $J/\psi$ ) and also due to the Drell-Yan process [35]. The Drell-Yan process happens via the production of a virtual photon during the interaction between the valence quark of a nucleon that is part of the projectile nucleus with the sea anti-quark of the target nucleus and its subsequent decay into a di-muon pair [35]. A schematic diagram illustrating the various sources of di-muon (dilepton) production as a function of the invariant mass has been shown in Fig. 1.3.

The di-muon invariant mass spectrum can be broadly categorized as follows :

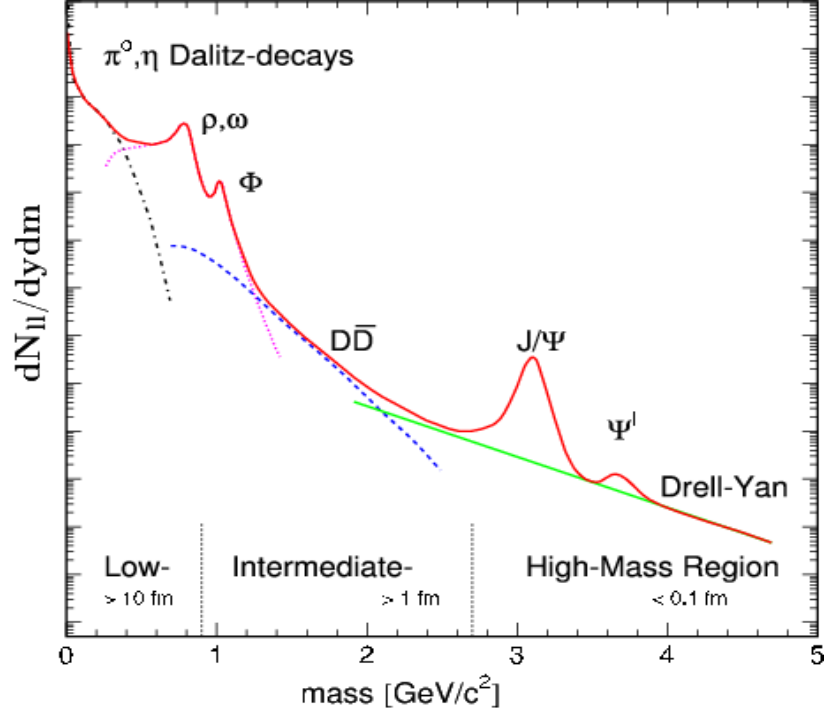


Figure 1.3: Schematic diagram highlighting the di-muon (dilepton) production sources as a function of the di-muon (dilepton) invariant mass in heavy ion collisions [35].

- **High Mass Range (HMR):**  $M \geq M_{J/\psi} (= 3.1 \text{ GeV})$  : The production of di-muons in this mass regime occurs at the earliest stages of the collision and carry vital information about primordial emission. The dominant contribution to di-muons in this regime come from the decay of quarkonia ( $q\bar{q}$ ) like  $J/\psi$  ( $c\bar{c}$ ) and  $\Upsilon$  ( $b\bar{b}$ ) and from Drell-Yan processes. In the presence of the deconfined medium created in heavy-ion collisions, the  $q\bar{q}$  binding potential is screened which leads to the dissociation of quarkonia and hence quarkonium suppression is one of the signatures of the formation of a QGP medium [17]. Quarkonium states differ in their binding energies and they predictably melt at different temperatures due to the color screening. The measurement and study of quarkonia like  $J/\psi$  and  $\Upsilon$  over a wide range of transverse momentum helps to investigate the color screening property of

the QGP in detail alongside the medium temperature and energy density [33][34][36].

- Intermediate Mass Range (IMR):  $M_\phi < M < M_{J/\psi}$ : The dominant contribution to the intermediate mass range of the di-muon invariant mass spectrum is predicted to come from the QGP thermal radiation [32]. An enhancement in di-muon production in this mass regime serves as a signal of QGP formation. In order to obtain a clean measurement of the thermal dimuon spectrum, the contribution due to open flavor ( $c\bar{c}$ ) decay has to be removed.
- Low Mass Range (LMR):  $M \leq M_\phi (= 1.020 \text{ MeV})$ : Di-muon production in the low mass range is influenced by the decay of vector mesons [ $\rho(770)$ ,  $\omega(782)$  and  $\phi(1020)$ ]. Investigation of the low mass range of the di-muon spectrum provides information about the in-medium modifications of the vector mesons. This is an important property of the medium that needs to be addressed to understand how hadronic mass is generated through the spontaneous breaking of the QCD chiral symmetry [32].

The properties of the QGP can be suitably studied using electrons and photons. However, muons offer significantly reduced backgrounds from hadronic decays,  $\pi^0$  and  $\eta$  Dalitz decays ( $\pi^0 \rightarrow \gamma\gamma$ ,  $\eta \rightarrow \gamma\gamma$ ) and gamma conversions in materials compared to electrons and photons. The higher muon mass will also ensure less Bremsstrahlung radiation loss in detector material budget which will improve the invariant mass resolution previously unachievable with electrons.

### 1.3 Probing the matter created at RHIC with photons

The Relativistic Heavy Ion Collider (RHIC) has been designed to search for the existence of the Quark Gluon Plasma (QGP) [2–5], created under extreme conditions of temperature and energy density in heavy-ion collisions and to study its properties. The experimental study of QGP includes the detection of the products of heavy-ion collisions by particle detectors and understanding the underlying mechanisms using suitable observables constructed out of the properties

of the detected particles. The primary physics goal is to explore the properties of the strongly interacting QGP (sQGP) via its subsequent transition to the hadron gas (HG) phase [2–5]. The phase transition from the chirally symmetric sQGP to the chirally broken Hadronic Gas phase is associated with the confinement and the chiral phase transitions. This is characterised by an enhancement in the fluctuations of several conserved quantities, viz. net-electric charge, net-strangeness and net-baryon number [39–42]. In the experimental scenario, after phase transition into the hadronic phase, the hadrons free stream in all possible  $4\pi$  directions towards the detectors. The acceptance of the detectors in an experiment, however, is limited to a fraction of the  $4\pi$  phase space. Measurement of the dynamical fluctuations of the aforementioned conserved quantities in limited phase space, following the Grand Canonical Ensemble (GCE) prescription is well suited to act as probes of the phase transition [39][40]. Theoretical predictions suggest that dynamical fluctuations of the ratio of charged-to-neutral pions [43–46] is sensitive to the chiral phase transition and can be used as an excellent indirect probe. During the chiral phase transition, when the system created in heavy-ion collisions evolves and is rapidly cooled, the possibility of the formation of metastable domains has been predicted and this has been schematically shown in Fig. 1.4. The metastable domains are characterised by a misalignment of the four-component  $(\sigma, \pi)$  chiral condensate relative to its true vacuum orientation and is hence referred to as Disoriented Chiral Condensates (DCC) [43–46]. The event-by-event neutral pion fraction ( $f$ ) is defined as the ratio of the neutral pion multiplicity to the total multiplicity of pions (charged and neutral) in an event.

$$f = N_{\pi^0} / (N_{\pi^0} + N_{\pi^\pm}) \quad (1.1)$$

Generic pion production according to the isospin symmetry from a medium in thermal equilibrium, leads to the production of pions of different isospin in equal abundances [44][46]. The distribution of  $f$  in that case should naturally show a peak at  $1/3$ . The decay of the metastable

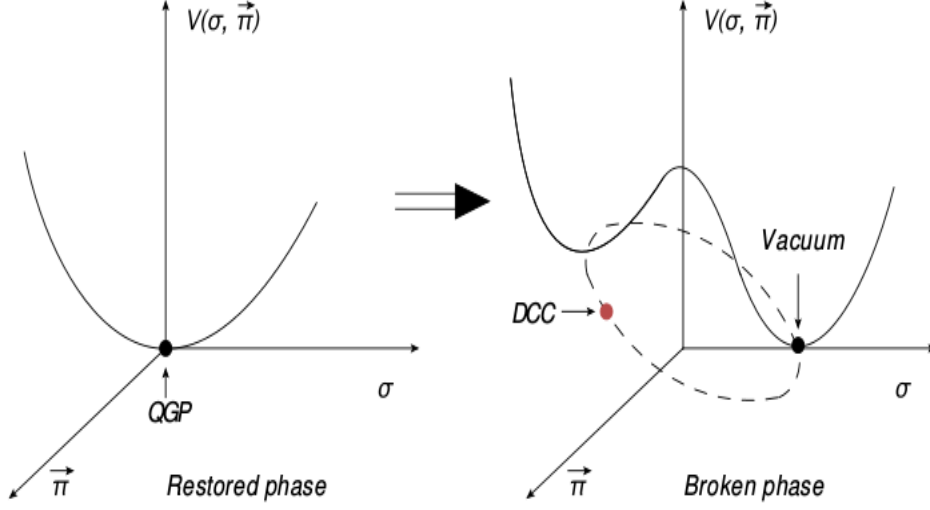


Figure 1.4: Metastable DCC domains characterised by a misalignment of the four-component  $(\sigma, \pi)$  chiral condensate relative to its true vacuum orientation during chiral phase transition [30].

DCC domains completely changes this scenario and causes anomalous production of pions of a particular isospin. The probability density function of  $f$  in this case is predicted [44][46] to be

$$P(f) = \frac{1}{2\sqrt{f}} \quad (1.2)$$

Therefore, if we observe the dynamical fluctuation of the charged-to-neutral pion ratio or the neutral pion fraction ( $f$ ) on an event-by-event basis, there is bound to be a difference for DCC and non-DCC cases. The dominant contribution to charged and neutral particle multiplicity in heavy-ion collisions comes from pions ( $\pi^\pm, \pi^0$ ) [47] and neutral pions promptly decay into photons ( $\gamma$ ). As a result, the observable of interest is the correlation of the charged particle multiplicity (representing charged pions) and photon multiplicity (representing neutral pions), which now serves as the indirect probe of the QCD chiral phase transition. It can be shown that the neutral pion fraction bears a close resemblance with the inclusive charged particle and

photon multiplicity ratio ( $f^{ch-\gamma}$ ) which can be expressed as

$$f^{ch-\gamma} = \frac{1}{(1 + 2N_{ch}/N_{\gamma})} \quad (1.3)$$

Thus, the dynamical (anti-)correlation that can exist between charged and neutral pions [45] is reflected in the correlation of charged particles (ch) and photons ( $\gamma$ ). It has been predicted theoretically that DCC domain size is inversely proportional to average pion momentum [48], causing the lower range of the pion spectrum to be more sensitive towards DCC formation. Attempts to study this phenomenon in heavy-ion and proton-proton collisions have already been performed. Measurements in heavy-ion collisions at  $\sqrt{s_{NN}} = 17.3$  GeV at the SPS [49] and in  $p + \bar{p}$  collisions at the Tevatron by the Minimax Collaboration [50] at  $\sqrt{s_{NN}} = 1.8$  TeV have revealed that formation of DCC domains of large size in these two scenarios is not possible. This brings us to heavy-ion collisions at RHIC at much higher energies where the possibility of DCC formation is predicted theoretically [51–53].

## 1.4 Outline of this thesis work

This thesis is aimed at exploring the matter created at RHIC heavy-ion collisions using probes at mid and forward rapidities. At mid-rapidity, the work is on the detection of di-muons, with the emphasis on building a muon detector as an upgrade of the STAR experiment at RHIC. The large area muon detector at STAR wishes to use Multigap Resistive Plate Chamber(MRPC) technology for the precise timing and hit position measurement of di-muons to explore the properties of the new state of matter. The objective of this thesis is to build MRPC's for the STAR detector upgrade. Data taking is ongoing with this detector. At forward rapidity, correlations between charged particles and photons have been studied at various collision energies using simultaneous measurement of charged particles and photons in the common geometric acceptance of two forward detectors of the STAR experiment. In the 2<sup>nd</sup> chapter of this thesis,

a brief introduction to the STAR experiment at RHIC is given. In the 3<sup>rd</sup> chapter, a general discussion about gaseous detectors is followed by an introduction to Multi-gap Resistive Plate Chambers, the fabrication and testing of MRPC's for the STAR-MTD upgrade and later on, the possible application of MRPC's in TOF-PET Imaging have been discussed in detail. The 4<sup>th</sup> chapter consists of the details of the event-by-event measurement of the charged-neutral correlation at a wide range of collisional energies at RHIC, the experimental observables used, the analysis methodology and a discussion of the results obtained. In the 5<sup>th</sup> chapter, conclusions and outlook have been presented.

# Bibliography

- [1] E.V. Shuryak, Phys. Rept. 61, 71 (1980); L. McLerran , Rev. Mod. Phys. 58, 1021 (1986).
- [2] J. Adams et al. (STAR Collaboration), Nucl. Phys. A 757, 102 (2005).
- [3] B. B. Back et al. (PHOBOS Collaboration), Nucl. Phys. A 757, 28 (2005).
- [4] K. Adcox et al. (PHENIX Collaboration), Nucl. Phys. A 757, 184 (2005).
- [5] I. Arsene et al. (BRAHMS Collaboration), Nucl. Phys. A 757, 1 (2005).
- [6] <http://snelling.web.cern.ch/snelling/my-research.html>
- [7] <http://www.star.bnl.gov/~gorbunov/main/node5.html>
- [8] E. V. Shuryak, Phys. Lett. B 78, 150 (1978) [Sov. J. Nucl. Phys. 28, 408 (1978)] [Yad. Fiz. 28, 796 (1978)].
- [9] B. Sinha, Phys. Lett. B 128, 91 (1983).
- [10] L. D. McLerran and T. Toimela, Phys. Rev. D 31, 545 (1985).
- [11] C. Gale and J. I. Kapusta, Phys. Rev. D 43, 3080 (1991).
- [12] D. K. Srivastava, B. Sinha, M. Gyulassy and X. -N. Wang, Phys. Lett. B 276, 285 (1992).
- [13] H. A. Weldon, Phys. Rev. Lett. 66, 293 (1991).



- [14] A. Adare et al. [PHENIX Collaboration], Phys. Rev. Lett. 104, 132301 (2010) [arXiv:0804.4168 [nucl-ex]].
- [15] M. Wilde [ALICE Collaboration], Nucl. Phys. A 904-905, 573c (2013) [arXiv:1210.5958 [hep-ex]].
- [16] G. Agakichiev et al., CERES collaboration, Phys. Rev. Lett. 75, 1272 (1995); Phys. Lett. B422, 405 (1998); Nucl. Phys. A661, 23 (1999); N. Masera et al. (HELIOS-3 collaboration), Nucl. Phys. A590, 93c (1995); A.L.S. Angelis et al. (HELIOS-3 collaboration), preprint CERN-EP/98-82; M.C. Abreu et al. (NA38/NA50 collaboration), preprint CERN-EP/99-112; E. Scomparin et al. (NA50 collaboration), J. Phys. G25, 235 (1999); P. Bordalo et al. (NA50 collaboration), Nucl. Phys. A661, 538 (1999).
- [17] T. Matsui and H. Satz, Phys. Lett. B 178, 416 (1986).
- [18] M. C. Abreu et al. [NA50 Collab.], Phys. Lett. B 410 (1997) 327, 337; M. Gonin et al. (NA50 Collab.), Nucl. Phys. A 610 (1996) 404c. ; M. C. Abreu et al. [NA50 Collaboration], Phys. Lett. B 477, 28 (2000).
- [19] C. Adler et al., Phys. Rev. Lett. 89, 202301 (2002).
- [20] B. Abelev et al. [ALICE Collaboration], Phys. Rev. Lett. 109, 072301 (2012) [arXiv:1202.1383 [hep-ex]]; P. Pillot [ALICE Collaboration], J. Phys. G 38, 124111 (2011) [arXiv:1108.3795 [hep-ex]].
- [21] A. Mocsy, P. Petreczky and M. Strickland, Int. J. Mod. Phys. A 28, 1340012 (2013) [arXiv:1302.2180 [hep-ph]].
- [22] H. Appelshauser et al. [NA49 Collaboration], Phys. Rev. Lett. 80, 4136 (1998) [nucl-ex/9711001]; J. Bachler et al. [NA49 Collaboration], Nucl. Phys. A 661, 45 (1999); C. Pinkenburg et al. [E895 Collaboration], Phys. Rev. Lett. 83, 1295 (1999) [nucl-ex/9903010].

- [23] K. H. Ackermann et al. [STAR Collaboration], Phys. Rev. Lett. 86, 402 (2001) [nucl-ex/0009011].
- [24] A. Adare et al. [PHENIX Collaboration], Phys. Rev. Lett. 98, 162301 (2007) [nucl-ex/0608033]; B. Abelev et al. [STAR Collaboration], Phys. Rev. Lett. 99, 112301 (2007) [nucl-ex/0703033].
- [25] D. Molnar and S. A. Voloshin, Phys. Rev. Lett. 91, 092301 (2003) [nucl-th/0302014]; R. J. Fries, B. Muller, C. Nonaka and S. A. Bass, Phys. Rev. C 68, 044902 (2003) [nucl-th/0306027].
- [26] K. Adcox et al. [PHENIX Collaboration], Phys. Rev. Lett. 88, 022301 (2002) [nucl-ex/0109003]; C. Adler et al. [STAR Collaboration], Phys. Rev. Lett. 89, 202301 (2002) [nucl-ex/0206011].
- [27] K. Aamodt et al. [ALICE Collaboration], Phys. Lett. B 696, 30 (2011) [arXiv:1012.1004 [nucl-ex]]; S. Chatrchyan et al. [CMS Collaboration], Eur. Phys. J. C 72, 1945 (2012) [arXiv:1202.2554 [nucl-ex]].
- [28] X. N. Wang, M. Gyulassy and M. Plumer, Phys. Rev. D 51, 3436 (1995) [hep-ph/9408344].
- [29] S. S. Adler et al. [PHENIX Collaboration], Phys. Rev. Lett. 91, 072303 (2003) [nucl-ex/0306021]; J. Adams et al. [STAR Collaboration], Phys. Rev. Lett. 91, 072304 (2003) [nucl-ex/0306024].
- [30] P. Tribedy, PhD Thesis, Homi Bhabha National Institute, India, 2014.
- [31] C. Y. Wong, Introduction of High Energy Heavy Ion Collisions, World Scientific, Singapore, 1994.
- [32] G. David et al., Physics Reports 462 (2008) 176–217.
- [33] STAR Muon Telescope Detector Proposal:  
[http://www.star.bnl.gov/~ruanlj/MTDreview2010/MTD\\_proposal\\_v14.pdf](http://www.star.bnl.gov/~ruanlj/MTDreview2010/MTD_proposal_v14.pdf).

- [34] L. Ruan et al., J. Phys. G 36, 095001 (2009).
- [35] Rupa Chatterjee et al., Lect.Notes Phys. 785 (2010) 219-264 arXiv:0901.3610 [nucl-th].
- [36] Frank Geurts, Rice University, MTD Physics, STAR Collab. Mtng, LBNL, 2013,  
[https://drupal.star.bnl.gov/STAR/system/files/LBNL2013\\_MTDphysics\\_0.pdf](https://drupal.star.bnl.gov/STAR/system/files/LBNL2013_MTDphysics_0.pdf)
- [37] G Lin (for the STAR Collaboration) 2006 A New Large-area Muon Telescope Detector at Mid-rapidity at RHIC, talk presented at DNP 2006, Nashville, TN, 25–28 October.
- [38] S S Adler et al 2004 Phys. Rev. C 69 014901.
- [39] S. Jeon and V. Koch, Phys. Rev. Lett. 83, 5435 (1999).
- [40] S. Jeon and V. Koch, Phys. Rev. Lett. 85, 2076 (2000).
- [41] V. Koch, A. Majumder, and J. Randrup, Phys. Rev. Lett. 95, 182301 (2005).
- [42] M. Asakawa, U. W. Heinz, and B. Muller, Phys. Rev. Lett. 85, 2072 (2000).
- [43] J.D. Bjorken, What lies ahead?, SLAC-PUB-5673, 1991.
- [44] J. P. Blaizot and A. Krzywicki, Phys. Rev. D 46, 246 (1992).
- [45] K. Rajagopal and F. Wilczek, Nucl. Phys. B 399, 395 (1993).
- [46] K. Rajagopal, in Quark-Gluon Plasma 2 (World Scientific, Singapore, 1995), Chap 9, pp. 484–554.
- [47] J. Adams et al. [STAR Collaboration], Phys. Rev. Lett. 95, 062301 (2005).
- [48] R. Bellwied, S. Gavin, and T. Humanic, in Advances in Nuclear Dynamics 4, edited by W. Bauer and H.-G. Ritter (Springer, New York, 1998), pp. 43–53.
- [49] M. M. Aggarwal et al. (WA98 Collaboration), Phys. Lett. B 420, 169 (1998); M. M. Aggarwal et al. (WA98 Collaboration), Phys. Rev. C 64, 011901 (2001); M. M. Aggarwal et

- al. (WA98 Collaboration), Phys. Rev. C 67, 044901 (2003); M. M. Aggarwal et al., Phys. Lett. B 701, 300 (2011).
- [50] T. C. Brooks et al. (MiniMax Collaboration), Phys. Rev. D 61, 032003 (2000); T. C. Brooks et al. (MiniMax Collaboration), Phys. Rev. D 55, 5667 (1997).
- [51] K. Rajagopal, Nucl. Phys. A 680, 211 (2001);
- [52] M. Asakawa, H. Minakata, and B. Muller, Nucl. Phys. A 638, 443c (1998); ,Phys. Rev. C 65, 057901 (2002).
- [53] S. Gavin, A. Gocksch, and R. D. Pisarski, Phys. Rev. Lett. 72, 2143 (1994) ; S. Gavin and B. Muller, Phys. Lett. B 329, 486 (1994); S. Gavin, Nucl. Phys. A 590, 163 (1995); S. Gavin and J. I. Kapusta, Phys. Rev. C 65, 054910 (2002).

## Chapter 2

# Heavy Ion Collision Experiments at RHIC

### 2.1 The Relativistic Heavy Ion Collider

The Relativistic Heavy Ion Collider (RHIC) [1], located at the Brookhaven National Laboratory in Upton, New York, USA, is an intersecting storage ring that has been colliding heavy-ions (AA), protons (pp) and protons with heavy-ions (pA) since 2000 to create and explore primordial matter that is believed to have been existing in the Universe, a few microseconds after the Big Bang. RHIC is the first dedicated collider in the world. In terms of center of mass energy achieved during collisions, it is the 2nd largest collider in the world, next only to the Large Hadron Collider (LHC) at CERN (European Organization for Nuclear Research) [2]. It is also the only facility in the world capable of colliding polarized proton beams to study the nucleonic spin structure [3].

Collisions occur at RHIC between counter-rotating heavy ions and/or protons (polarized) traversing at maximum speeds of  $0.99995c$ , where  $c$  is the speed of light, in a pair of quasi-circular, concentric, superconducting rings inside the 3.8 km long underground tunnel. During the last 15 years of data taking, RHIC has collided a wide range of particle and ion species,  $\text{Au} + \text{Au}$ ,  $\text{p}$

+ p, d + Au, He + Au, Cu + Cu, Cu + Au, U + U and p + Au. The center of mass collision energy ranges for heavy ions are vast, ranging from 7.7 - 200 GeV per nucleon pair, while polarised protons have been collided at the center of mass energy of upto 500 GeV per nucleon pair [3]. The two independent RHIC rings have six intersections, also called interaction points. Four major experiments had been set-up at these points of intersection, STAR [4] (Solenoidal Tracker At RHIC) at 6 o'clock, PHENIX [44] (Pioneering High Energy Nuclear Interaction eXperiment) at 8 o'clock, PHOBOS [6] is located at 10 o'clock and BRAHMS [7] (Broad RAnge Hadron Magnetic Spectrometers) at 2 o'clock. STAR and PHENIX are the currently operational experiments as PHOBOS and BRAHMS have been discontinued after the experiments met their respective physics goals. Fig. 2.1 shows an aerial view of RHIC highlighting the location of the four experiments and the different particle accelerators that have been described in the next section.

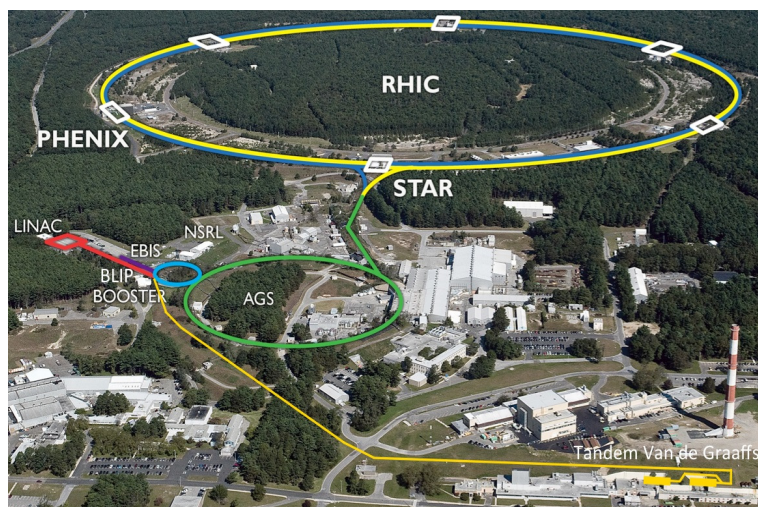


Figure 2.1: Aerial view of the RHIC complex

## 2.2 The Accelerators

The production of high intensity heavy ion beams at RHIC is a non-trivial procedure that goes through three stages of acceleration [8][9], in a chain of injectors, the Tandem Van de Graaff, the

Booster Synchrotron and the AGS (Alternate Gradient Synchrotron) in the order of sequence. A schematic of the locations of the 4 different experiments and the accelerators at RHIC are shown in Fig. 2.2 while the acceleration of Gold (Au) ion beams at RHIC is shown schematically in Fig. 2.3. The acceleration of Gold ions at RHIC begins at the Tandem Van de Graaff. The Tandem is a dual stage linear electrostatic accelerator, where two Van de Graaff accelerators are connected in series with the joining region at a common potential of +14 MV and the ends at ground potential. Under the effect of an electric field, the singly negative Gold ion beam ( $Au^{-1}$ ) from the Cesium Sputter Ion source is accelerated to the Tandem terminal where it is stripped to a charge state of +12 by a stripper foil. It is then transferred to the Booster Synchrotron after being accelerated to 1 MeV/nucleon by the Tandem via the Tandem-To-Booster (TTB) line. During the transfer, the beam is stripped to +32 charge state by a stripper foil in the Tandem-To-Booster (TTB) line.

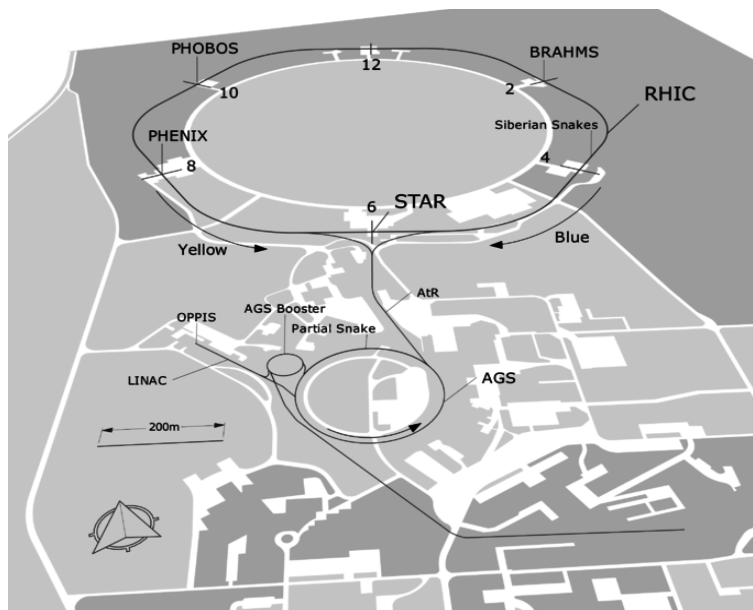


Figure 2.2: A schematic showing the locations of the 4 different experiments and the accelerators at RHIC [8].

After a successful 40 years' of operation, the Tandem Van de Graaf accelerator[10] which used to be the primary ion source and pre-injector for collisions at RHIC till 2011 and has since been

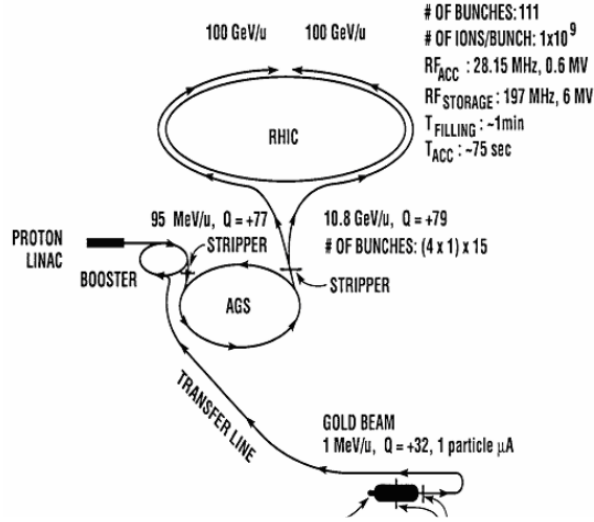


Figure 2.3: A schematic showing the acceleration scheme for Au ion beams at RHIC [9].

replaced by a more versatile and compact Electron Beam Ion Source (EBIS) since 2012. The capability of the EBIS to create ion beams starting with neutral atoms or positive ions is a huge advantage as this has led to creation of ion beams from nearly every element on the periodic table. The EBIS brings Gold ions to a net charge of +32. This unique feature of the EBIS culminates in the Gold ions reaching a higher energy over a smaller applied voltage and over shorter distances traversed. The use of new generation sophisticated accelerator technologies compounded with the compactness of the EBIS makes the job of pre-injecting beams, relatively simpler, more reliable and a profitable process. Gold ions are accelerated to 2 MeV/nucleon by the EBIS while polarised proton beams are accelerated to 200 MeV by the LINAC and fed to the 2nd stage of acceleration, the Booster Synchrotron. The Booster is a powerful circular accelerator that strips Gold ions to a charge state of +77 and further accelerates them to 95 MeV/nucleon before injecting them to the final accelerating stage, the AGS, at a speed of 37% of the speed of light. The AGS accelerates the ions to an injection energy of 10.8 GeV/nucleon, strips the two remaining electrons to take the ion beam to the highest charge state of +79. After acceleration, the beams from the AGS are transferred to the RHIC storage ring via the AGS-to-RHIC transfer line (AtR), at relativistic speeds of 99.7% of the speed of light. The



beams are then accelerated to the required collision energies and stored in the RHIC storage rings, namely the Blue (clockwise) ring and the Yellow (counter-clockwise) ring, before actual collisions take place. The technicalities of the process of acceleration of the beams are beyond the scope of this thesis and can be found detailed in the reference [11].

In order to probe the QCD (Quantum Chromodynamics, the theory that describes strongly interacting nuclear matter) [12] phase diagram as shown schematically in Fig. 2.4, RHIC has undertaken the programme of a beam energy scan, to look for signatures of the conjectured phase transition and to ascertain the existence of the critical end point. Thus far, heavy ion collisions at the energies  $\sqrt{s_{NN}}$  values of 7.7, 11.5, 14.5, 19.6, 27, 39, 62.4, 130 and 200 GeV have been undertaken at RHIC.

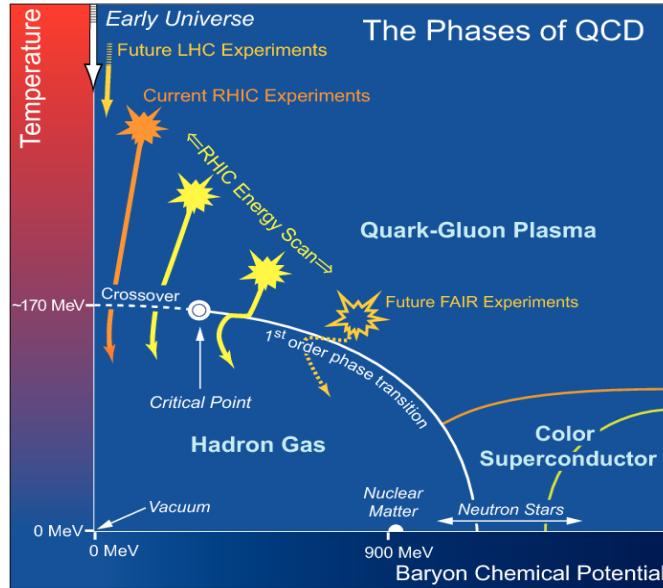


Figure 2.4: A schematic of the QCD phase diagram taken from the reference [13].

The advancement in accelerator technologies has led to a factor of 25 increase in peak luminosity ( $50 \times 10^{26} \text{ cm}^{-2} \text{ s}^{-1}$ ) for heavy ions, and a factor of 15 increase in the average store luminosity ( $30 \times 10^{26} \text{ cm}^{-2} \text{ s}^{-1}$ ) [9] over the design luminosity ( $2 \times 10^{26} \text{ cm}^{-2} \text{ s}^{-1}$ ) [14] of RHIC

using the novel method of stochastic cooling of the beams.

## 2.3 The STAR experiment

The fabrication and testing of Multigap RPC's and the data analysis described in the subsequent chapters of this thesis are parts of the STAR (Solenoidal Tracker at RHIC) experiment at RHIC. A brief introduction to the STAR experiment and the detector subsystems relevant to the works presented in this thesis have been discussed in this section.

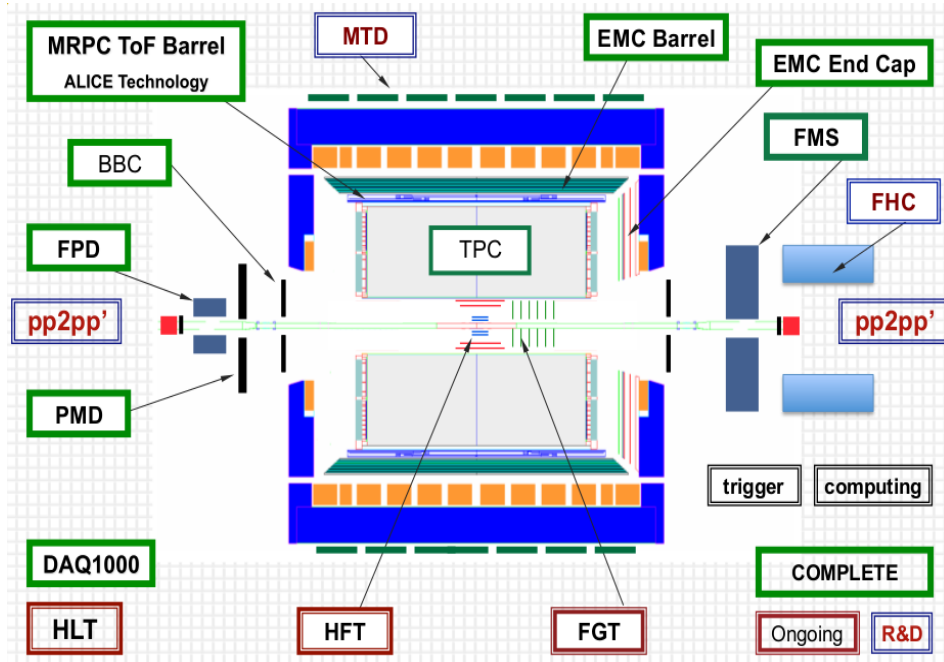


Figure 2.5: The STAR detector and its subsystems. This is an old picture of the experimental setup from the year 2012 taken from Ref. [15], where most of the subsystems are shown together. Detector R&D and installation has been completed for all subsystems. The PMD detector has been dismantled in the year 2011. The FGT replaced the FTTPC detector in 2012.

The detector subsystems of the STAR experiment are focussed on the detection and measurement of hadrons over a wide acceptance ( $0 \leq \phi \leq 2\pi$  in azimuth,  $|\eta| < 1.8$  and  $2.5 \leq \eta \leq 4.0$  in pseudorapidity) to meet with its principal objective of characterizing the properties of the Quark Gluon Plasma, the new state of matter created under extreme conditions during

heavy-ion collisions at RHIC. Located at 6 o'clock in the RHIC complex, the experiment gets its name for the fact that it is surrounded by a solenoidal magnet [19] with a maximum axial magnetic field 0.5 Tesla and its capability of high-precision tracking of particles alongwith the measurement of momentum and identification of particles. By definition, the beam-axis and the direction of the applied magnetic field is the z-axis in STAR. The magnetic field is responsible for bending the charged particle trajectories for momentum measurement.

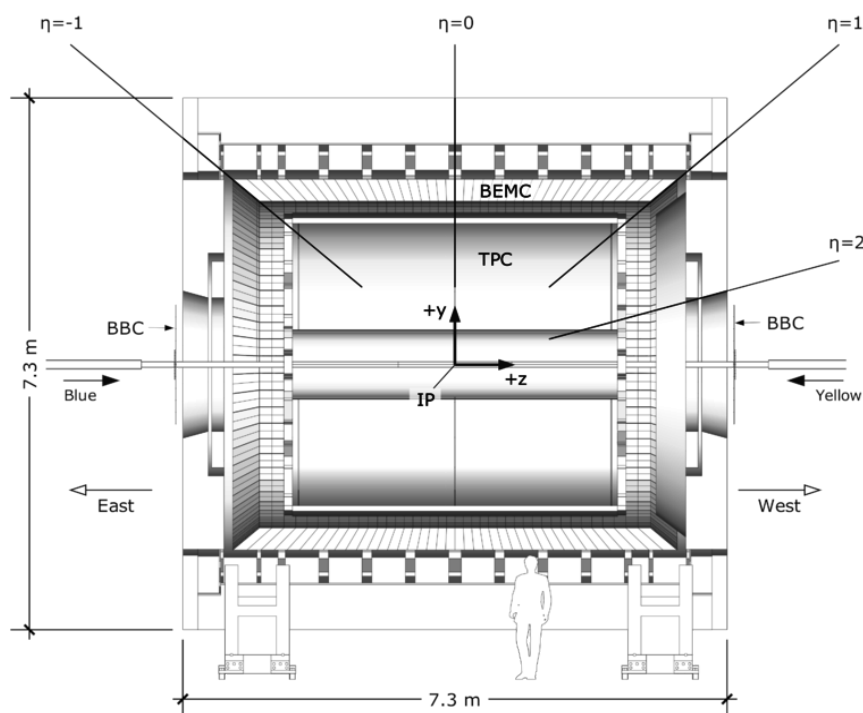


Figure 2.6: The co-ordinate system of the STAR experiment [16]

The STAR experiment consists of several detector subsystems. Fig 2.5 shows a schematic of the longitudinal section of the STAR detector with the different subsystems. The schematic in Fig. 2.6 does not indicate all the subsystems and is used just to illustrate the co-ordinate system of STAR. The central Time Projection Chamber is the main detector performing the dual tasks of charged particle tracking and particle identification within  $|\eta| < 1.8$  and complete azimuthal acceptance. The limitations in the TPC particle identification capability of charged

hadrons  $\pi$  and  $K(p)$  beyond a momentum range  $\sim 0.7(1.0)$  GeV/c led to the construction of the Time-of-Flight (TOF) detector. The large-area TOF detector based on Multigap Resistive Plate Chambers (MRPCs) technology surrounds the TPC and enhances charged hadron identification capability of the STAR experiment. The TOF acceptance is identical to that of the TPC. The two azimuthally symmetric Electromagnetic Calorimeters (EMC), the Barrel EMC (BEMC) covering the pseudorapidity region  $|\eta| < 1$  and the Endcap EMC (EEMC) covering the pseudorapidity region  $1 \leq \eta \leq 2$ , are suited for transverse energy measurement of electrons and photons. The Photon Multiplicity Detector (PMD) installed in the forward direction within the pseudorapidity coverage  $-3.7 \leq \eta \leq -2.3$  and  $2\pi$  in azimuth, is a preshower detector that measures event-by-event multiplicity and spatial distribution of photons. The PMD was dismantled in the year 2011. As an extension to STAR's capability of charged particle tracking in the forward region, two azimuthally symmetric Forward Time Projection Chambers (FTPC) were installed in STAR and cover  $2.5 \leq \eta \leq 4.0$  in pseudorapidity. The FTPC detector has been subsequently dismantled in the year 2011. Additionally, for event triggering, two Zero Degree Calorimeters (ZDC), two Beam Beam Counters (BBC) and two upgraded Pseudo Vertex Position Detectors (up-VPD) are positioned on either side of the interaction point at STAR.

The subsystems relevant to this thesis have been discussed in the following subsections.

### 2.3.1 The Time Projection Chamber – TPC

At the heart of STAR is the main tracking detector, the Time Projection Chamber (TPC) [17]. Initially built at the Lawrence Berkeley National Laboratory in California, the TPC was then transported to the Brookhaven National Laboratory in November 1997. The STAR TPC is a unique detector in the sense that it has a large cylindrical gas volume that works as a drift chamber and the readout endcaps are based on Multi Wire Proportional Chamber technology. The TPC that surrounds the STAR interaction point, is 4.2m in length, with its inner and outer drift volumes having radii of 50 cm and 200 cm, respectively. The TPC is positioned inside the solenoidal STAR magnet [19] in a 0.5T magnetic field, provides complete azimuthal coverage and

a pseudorapidity coverage of  $\pm 1.8$  units over the entire range of multiplicities. A schematic of the detector is shown in Fig. 2.7. The main purpose of the TPC is a 3-dimensional reconstruction of particle tracks, momentum measurement over a range of 0.1 GeV/c to 30 GeV/c and ionization energy loss ( $dE/dx$ ) measurement for particle identification over a range of 0.1 GeV/c to 0.7 GeV/c for pions and kaons and upto 1 GeV/c for protons.

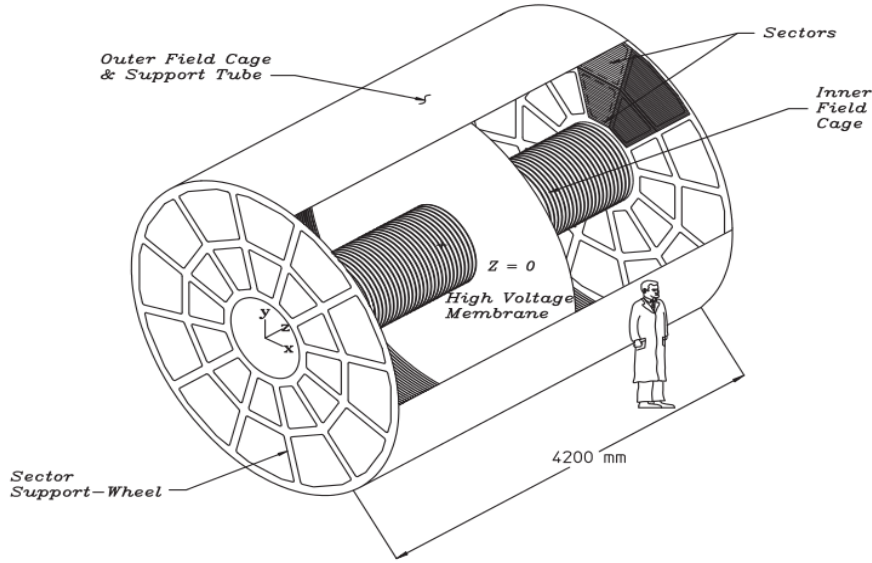


Figure 2.7: The STAR Time Projection Chamber [17]

The TPC is a gas detector in which a charged particle traversing the volume creates primary ionization along its track. The central cathode membrane, maintained at -28 kV divides the detector into two identical halves with readout pads on both sides. The electric field in the drift volume is  $\sim 135$  V/cm. The drift field prevents the electron-ion pairs from recombining and is kept reasonably low to prohibit secondary ionisation. The ionization electrons drifting towards the anodes under the influence of this field are prevented from diffusion by the magnetic field applied parallel to it. Under the effect of the Lorentz force, the electrons follow a helical path that enables the measurement of their momentum. The homogeneity of the electric field is extremely essential as any distortions in the electric field would lead to a degradation of the sub-millimeter track reconstruction resolution. This is maintained by equally-spaced inner and

outer field cages which are concentric equipotential rings. The rings maintain a uniform gradient between the central cathode membrane and the end caps that are at ground potential.

A gas mixture of Argon and Methane in the ratio 90 : 10 [18], that goes under the trade name P10, is used as the sensitive medium of the TPC. The detector is maintained at a pressure of 2 mbar above atmospheric pressure [18]. The Argon gas is used as the ionizer while methane acts as the quencher preventing UV photons from propagating inside the sensitive medium. P10 is chosen as the sensitive medium due to the fact that the drift velocity ( 5.45 cm/microsec) of ionization electrons in this gas mixture reaches its peak and saturates at the applied TPC drift field ( 130 V/cm). This helps in minimizing the variations of the drift velocity due to pressure and temperature changes. A laser calibration system has been set up to periodically measure the drift velocity.

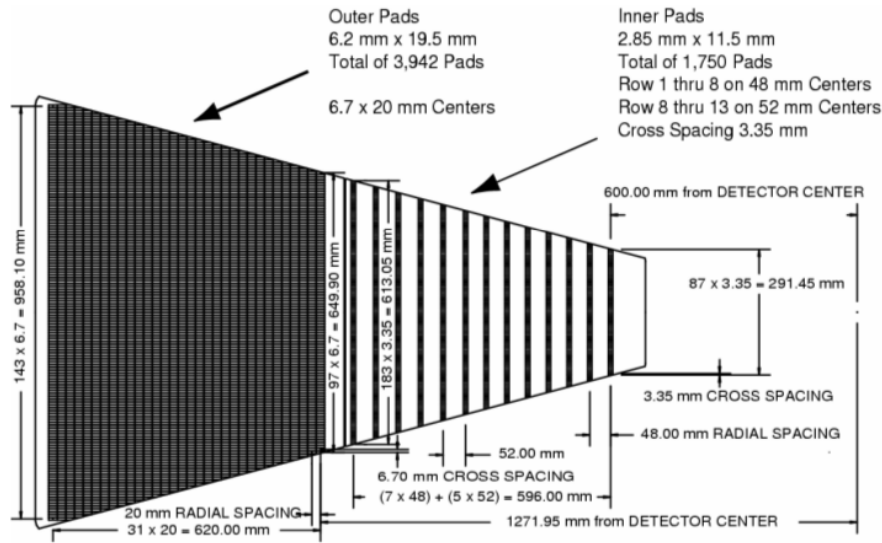


Figure 2.8: The TPC Anode pad plane showing the inner and outer sectors [17].

Signal readout of the TPC is based on MWPC technology with readout pads segmented perpendicular to the direction of drift of the electrons. The electron signal due to primary ionization is weak and detection requires signal amplification. An avalanche amplification (discussed in detail in Sec. 3.3.2) takes place in the vicinity of the 20 micron anode wires due to

the high electric fields. A plane of wires called the gating grid electrostatically separate the drift region from the readout region and allow electrons to pass through selectively, depending on the trigger, by taking on the necessary voltages. The grid also prevents ions created in the amplification region from drifting back to the drift volume and thereby protect the drift field from any unwanted distortions. The anode wires are positioned between a grounded shielding wire plane and the anode pad plane. Inner and outer sectors of the anode grids are maintained at different voltages, 1.1 kV and 1.39 kV respectively. The gain of the TPC, which is defined as the ratio of the number of avalanche electrons created via secondary ionisation to the initial number of drift electrons, is 1230 and 3770 for the inner and outer anode sectors respectively. The MWPC has 12 sectors on both sides, each sector being divided into 45 padrows. The inner sectors have 13 padrows and since regions of smaller radius have much higher track-densities, their design is optimized for providing closer space points for a better two-track resolution. The outer sectors on the other hand have 32 padrows to provide a continuous coverage of the pads for optimal energy deposition resolution. The anode pad plane with the inner and outer sectors are schematically shown in Fig. 2.8. Each hit inside the TPC sensitive volume is recorded in three dimensions, the x,y position is obtained from the sectors and the z position is obtained from the time of arrival of the drifting electrons. Comprehensive details about the TPC can be found in the references [17][18].

### 2.3.2 The Time-Of-Flight detector – TOF

The Time-of-Flight detector (TOF) [20] at STAR that utilises Multigap Resistive Plate Chamber (MRPC) technology akin to the ALICE-TOF at LHC, has been fully functional since the year 2010. This large area detector ( $\sim 50 \text{ m}^2$ ) has two key elements, the up-VPD that provides the start time information and the barrel TOF - MRPC system that provides the stop time for the particle time of flight (stop time - start time =  $\tau$ ) measurement. The VPD's are scintillator detectors with photomultiplier tubes positioned  $\pm 5.7\text{m}$  on either side of the interaction point with a pseudorapidity coverage of  $4.24 < \eta < 5.1$ . They detect the coincidence signals from high

energy photons emerging at forward rapidity [21].

The main purpose of this detector is to significantly improve upon the efficiency of charged particle identification at higher momenta, that was previously impossible with the TPC. Using time of flight information from the TOF system, it was possible to perform direct particle identification of  $\pi : K : p$  upto  $\sim 1.7 - 1.9$  GeV/c in momenta and identification of  $(\pi + K) : p$  upto a momentum range of  $\sim 2.9 - 3.1$  GeV/c. In conjunction with ionization energy loss information from the TPC, the TOF has increased particle identification efficiency of STAR to more than 98% of the charged hadronic spectra.

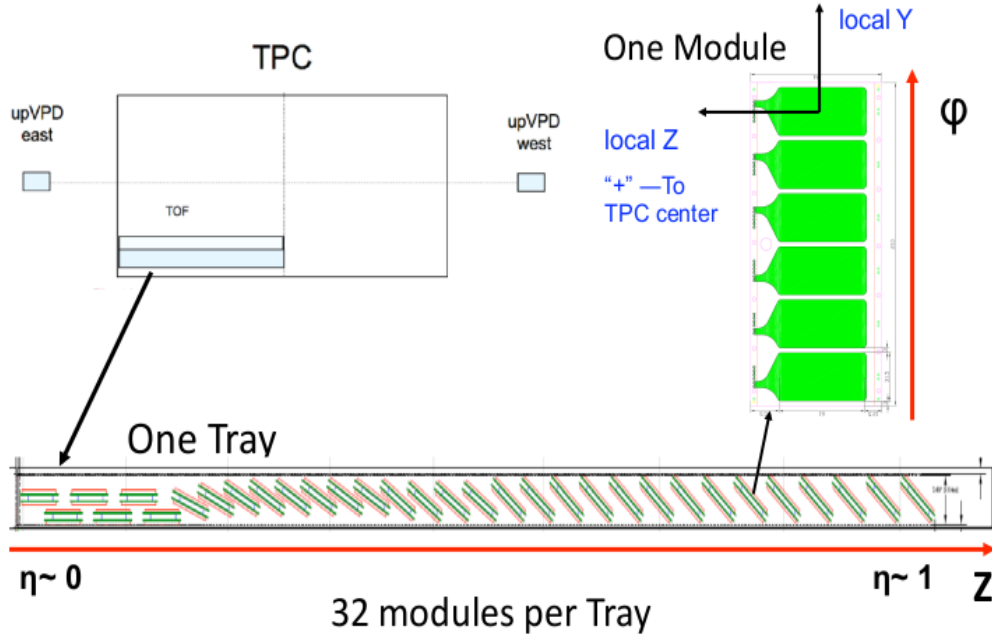


Figure 2.9: The geometry of the TOF detector, including readout pad design taken from reference [22]

The detector system comprises of 120 gas-tight trays with 32 MRPC's mounted in each tray as shown in Fig. 2.9. The 3840 MRPC's each having six readout pads make for 23040 readout channels in total. The TOF is cylindrical in shape, located immediately next to the TPC and has exactly same acceptance. The MRPC's for the STAR-TOF are 5 gap modules, with each sub-gap being  $220 \mu\text{m}$  and the internal and external resistive float glass plates being  $0.54 \text{ mm}$  and  $1.1 \text{ mm}$



in thickness respectively. The outer surface of the external electrodes are coated with graphite to facilitate the application of high voltage. The uniformity of the graphite paint ensures a uniform electric field. Readout pad dimensions are 6.1 cm in length (along the  $z$  direction) and 3.5 cm in width (along the  $\phi$  direction) and a thin insulating Mylar layer separates them from the outer electrodes. The detector operating voltage is 14 kV ( $\pm 7$  kV on each electrode) and for the avalanche mode of operation (to be discussed in detail in Sec. 3.3.3), a gas mixture of 95% Freon (R-134A) and 5% Isobutane (i-C<sub>4</sub>H<sub>10</sub>) is used. Charged particles traversing through the detectors lead to primary ionization in the gas gaps that eventually transforms into avalanches due to the strong, uniform electric field. The image charge is induced on the readout pads as a result of the movement of charges inside any of the gas gaps. The analog signals are then amplified and digitized on-board and converted into timing measurements [23]. Each TOF hit has an associated TPC track of momentum  $p$  and path length  $l$  (measured as helix distance between the primary vertex and the TOF channel). Using the time of flight ( $\tau$ ) information from the TOF, the particle velocity can be calculated as

$$\beta = \frac{l}{c\tau} \quad (2.1)$$

Starting with the expression for relative momentum,

$$p = \gamma\beta m \quad (2.2)$$

where,

$$\gamma = \frac{1}{\sqrt{1 - \beta^2}} \quad (2.3)$$

Substituting Eq.(2.3) in Eq.(2.2) and squaring both sides, we get

$$p^2 = \frac{m^2\beta^2}{1 - \beta^2} \quad (2.4)$$

$$\Rightarrow p^2 = \beta^2(m^2 + p^2) \quad (2.5)$$

we can arrive at the relation between the velocity ( $\beta$ ) and momentum ( $p$ ) as

$$\frac{1}{\beta} = \sqrt{\frac{m^2}{p^2} + 1} \quad (2.6)$$

The PID results with the first five TOF trays installed during the RHIC Run 8 in 2008, in terms of a scatter plot between the inverse of particle velocity and charged track momentum [23] have been shown in Fig. 2.10.

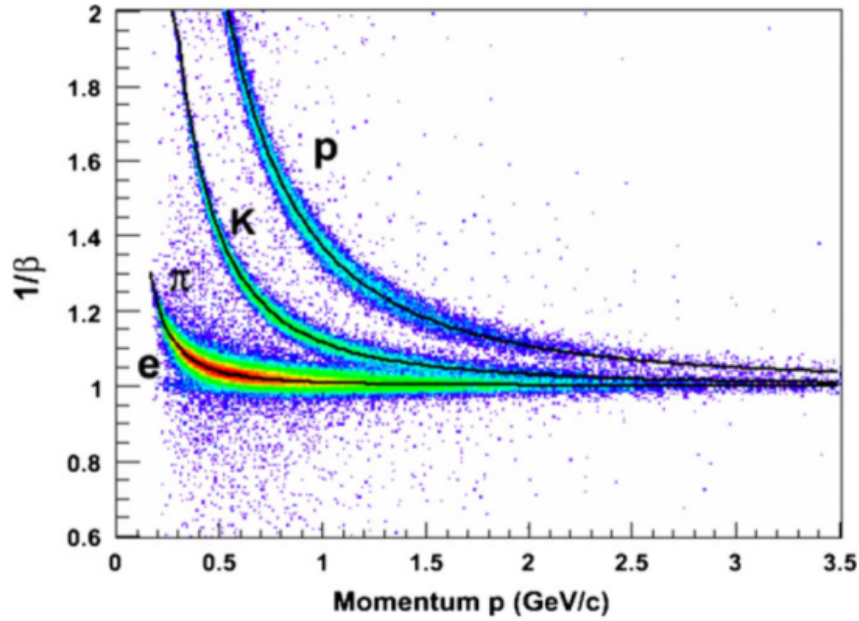


Figure 2.10: Particle identification performance of the first 5 TOF MRPC trays during RHIC p+p collisions in 2008 [23].

### 2.3.3 The Photon Multiplicity Detector – PMD

The Photon multiplicity detector (PMD) [24] is a preshower detector that was installed in STAR in 2002 to improve the phase space coverage for the detection of photons. Fig. 2.11 highlights the location of the PMD at STAR. It is designed to measure event-by-event photon

multiplicity in the forward region. The high particle density in the forward region prevented the installation of a calorimeter. The PMD has complete azimuthal coverage and a pseudorapidity coverage of  $-2.3$  to  $-3.7$ . The detector took data successfully from the years 2002 to 2011 before being decommissioned and dismantled. It was installed outside the STAR magnet at a distance of 5.4 metres from the interaction point along the beam axis. The detector (Fig. 2.12) has

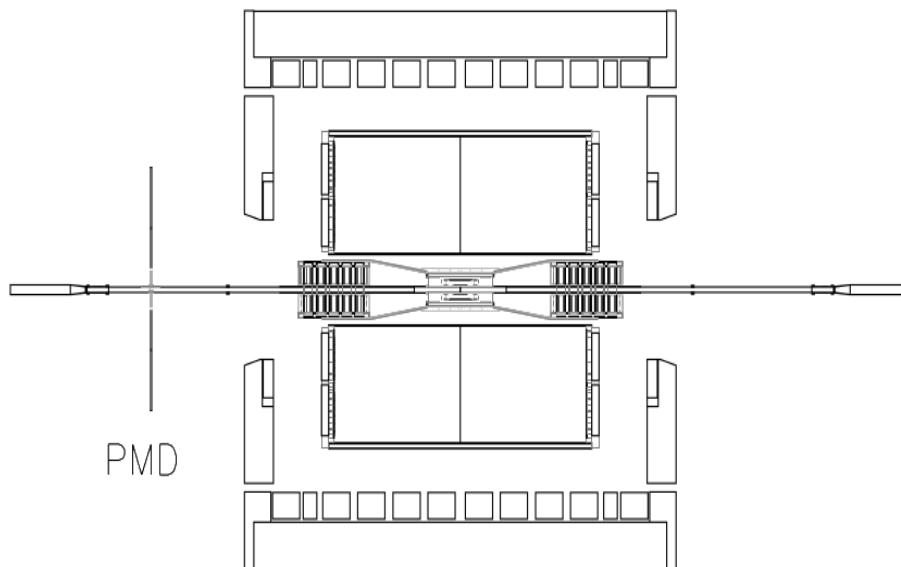


Figure 2.11: The STAR Photon Multiplicity Detector [24].

two identical highly granular planes on two sides of a 3 radiation length lead converter. The plane behind the lead converter is called the pre-shower plane and the plane in front is called the charged particle veto (CPV). The CPV plane enhances the hadron rejection capability of the PMD detector by acting as a veto for charged particles. The lead converter thickness is optimised for high photon conversion probability and minimisation of transverse shower spread. Extensive simulation studies and prototype tests led to the final working design of the detector. The detector is designed as an array of hexagon-shaped cells made of copper. These cells form the building blocks of the detector and a rhombus-shaped honeycomb of dimensions 25.4 cm in a matrix of  $24 \times 24$  cells makes up a unit module. A supermodule is a high voltage insulated, gas-tight enclosure consisting of a set of 4-9 unit modules. The pre-shower and the CPV planes

have 12 supermodules each, organised in a hexagonal geometry to ensure complete azimuthal coverage using the least number of supermodules.

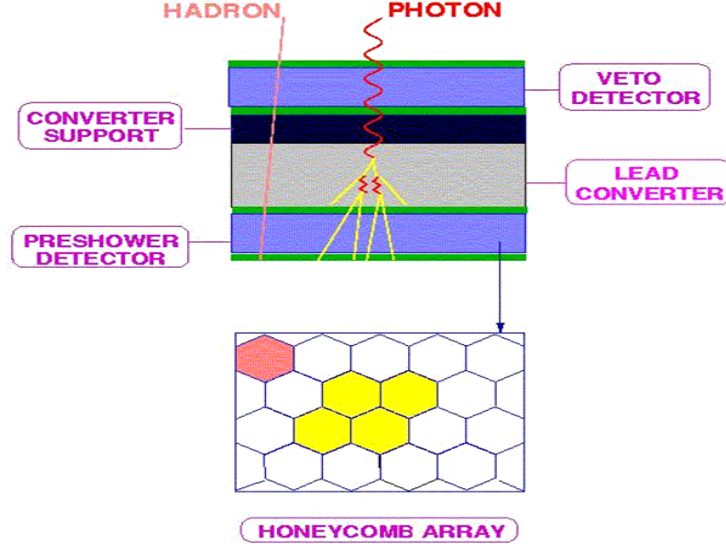


Figure 2.12: Working principle of the Photon Multiplicity Detector

The detector works on the principle of a proportional counter and a gas mixture of Ar + CO<sub>2</sub> in the ratio 70:30 by weight is the sensitive medium. Fig. 2.12 is a cartoon showing the working principle of the PMD. A photon incident on the lead converter creates an electromagnetic shower that spreads to more than one cell on the pre-shower plane leading to the formation of a large cluster. Charged hadrons do not shower upon incidence on the lead converter and usually affect a single cell of the pre-shower plane. The signal due to a charged hadron mimics a Minimum Ionising particle (MIP) signal. The CPV plane shares its electronics and data acquisition system with the pre-shower plane. Simulation studies using the HIJING [25] and AMPT [26] particle production models indicate that nearly 10-11 % of the total number of photons produced in a collision lie within the coverage of the PMD. The decay of neutral pions into photons is the dominant mode of photon production in heavy-ion collisions and HIJING calculations reveal that it is about 93-96 % [28].

### 2.3.4 The Forward Time Projection Chamber – FTPC

Charged particle detection with the TPC at STAR is limited to the pseudorapidity range  $|\eta| < 1$ . Two forward TPC's (FTPC) [27] have been installed in STAR on either side of the interaction point to provide an extension to the phase space coverage for charged particle detection. The two FTPC's cover  $2.5 < |\eta| < 4.0$  in pseudorapidity and  $2\pi$  in azimuth and measure the charge state and momenta of charged tracks.

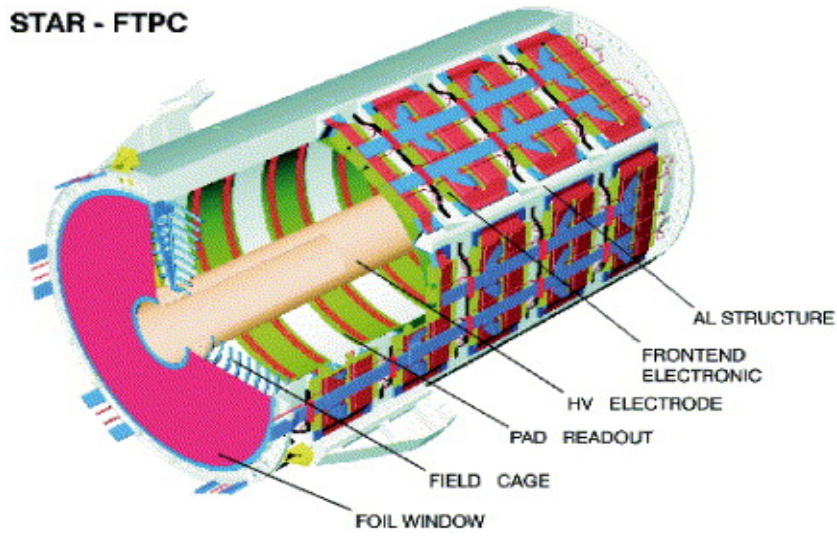


Figure 2.13: The STAR Forward Time Projection Chamber [27]

The cylindrical FTPC detectors as shown in Fig. 2.13, are 75 cm in diameter and 120 cm in length. The readout system consists of 10 padrows that are subdivided into six sectors, with 160 pads each. The FTPC sensitive medium is a gas mixture of Ar and CO<sub>2</sub> in a ratio of 50 % : 50% by weight. For the optimization of the limited space available for the drift of electrons inside the FTPC and the feasibility of track reconstruction amidst large particle density at forward rapidity, the FTPC utilises a radial electric field, perpendicular to the STAR magnetic field. Due to its novel design, the FTPC is capable of resolving two tracks upto 2 mm. Simulation studies using the HIJING [25] and AMPT [26] particle production models reveal that 6-7 % of the total produced charged particles are detected by the FTPC within its acceptance [28].

### 2.3.5 The Muon Telescope Detector – MTD

Muon detectors being used around the world in high energy physics experiments utilise tracking stations, trigger detectors and absorbers for the detection of muons. The large area Muon Telescope Detector (MTD) [31][32][33] at midrapidity ( $|\eta| < 0.5$ ) at STAR, covering 45% in azimuth [33] has been installed as an upgrade to the STAR experiment for the direct identification of muons. The MTD plans to make use of the inexpensive Multigap Resistive Plate Chamber (MRPC) [29] technology, known for its excellent timing and position resolution to achieve its physics goals [31][32]. The requirement for the MTD physics programme is a detector that can provide  $<100$  ps timing resolution and  $\sim 1$  cm position resolution for the identification of muons having a few GeV/c momentum [30]. The MTD utilises the inexpensive MRPC technology similar to the STAR-TOF system. MRPC's, known for their excellent timing and position resolution, give the MTD an edge in terms of muon detection and identification using precise timing and hit position measurement. The MTD modules are located at a radius of  $\sim 400$  cm from the collision point as can be seen from Fig. 2.14. The material budget due to the steel backlegs (flux-return bars) of the STAR magnet [19] that provide the return flux path to the solenoidal magnetic field, along with the Barrel Electromagnetic Calorimeter (BEMC) [34], serve as  $\sim 6$  interaction length hadron absorbers. The BEMC photomultiplier tubes and associated electronics are placed in boxes behind the magnet backlegs. The MTD MRPC modules are strategically placed on the BEMC PMT boxes for clean muon identification after rejection of the hadronic background. Muons are identified as hits on the MTD MRPC modules from the reconstructed TPC tracks extrapolated to the MTD, having proper timing and hit position values [32].

Installation of the 122 single-stack, 5-gap MRPC modules of outer dimensions  $91.5 \text{ cm} \times 58 \text{ cm}$  has been completed in 2014 after prototype studies since the year 2007. The MTD MRPC's are comparatively larger than their TOF counterparts. Gas gaps are defined by  $250 \text{ }\mu\text{m}$  thick nylon monofilament wires, called fishing lines. The resistive plates used for detector fabrication are float glass plates of volume resistivity  $\sim 10^{13} \text{ }\Omega\text{-cm}$ . The 4 inner plates are  $0.7 \text{ mm}$  in thickness while the 2 outer plates which are used as electrodes after coating them with a Licron

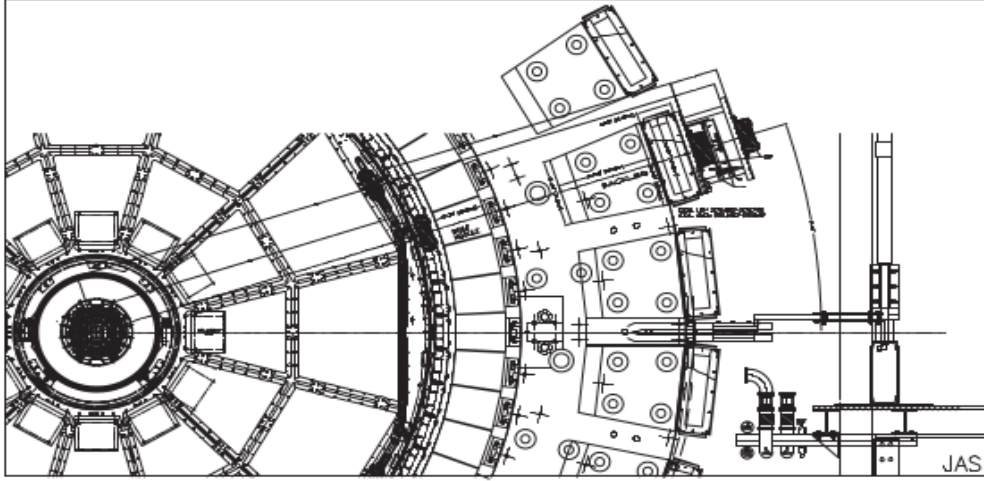


Figure 2.14: Location of the STAR MTD [32]

resistive paint are 1.1 mm in thickness. The detectors have double-ended readout in the form of Printed Circuit Boards (PCB's). Each PCB has 12 readout strips of dimensions  $87\text{ cm} \times 3.8\text{ cm}$  and adjacent strips are separated by a gap of 0.6mm [23]. The positive and negative high voltage electrodes are insulated from pick-up strips via Mylar foils and paper honeycomb boards on either side provide support. Fig. 2.15 illustrates the geometry of the MTD-MRPC's. The MTD MRPC's are operated in the avalanche mode at  $12.6\text{ kV}(\pm 6.3\text{ kV})$ . The detector sensitive medium is the same as that of the TOF-MRPCs, a mixture of Freon and Isobutane in the ratio 95:5 [23]. This unique, large area muon detection system has a timing resolution  $\sim 100\text{ ps}$  and spatial resolution  $\sim 1\text{ cm}$  [33] that fulfils the requirement for the MTD project [30].

### 2.3.6 Simulation results for the STAR-MTD

Simulation studies [32] were performed in the framework of the STAR experiment in order to establish the capability of the Muon Telescope Detector. Fig. 2.16 shows a full simulation of central Au+Au collisions using the HIJING event generator for the geometry configuration of all the STAR detectors including the entirety of the material budget. The muon detectors are shown in blue placed on top of the green iron return-bars (backlegs) of the STAR magnet within

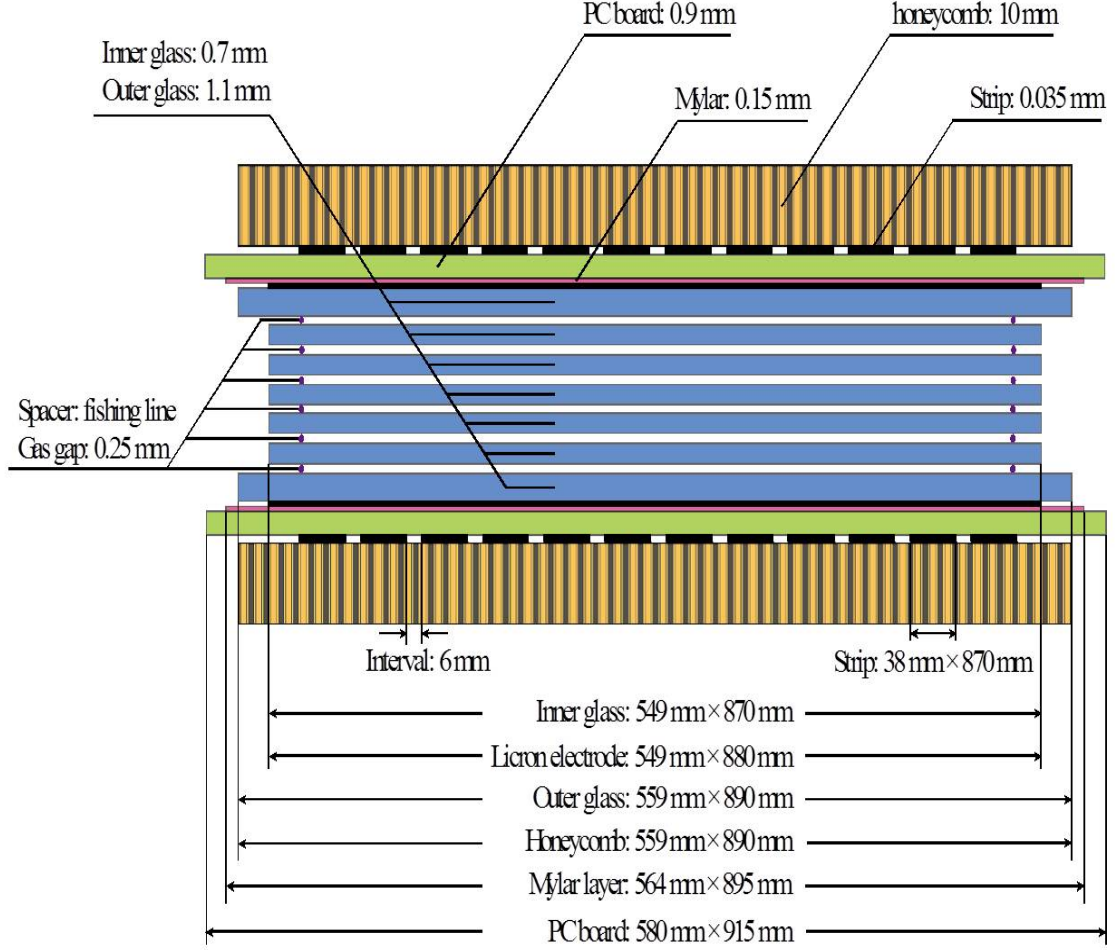


Figure 2.15: Schematic diagram of a 5-gap MRPC module for the STAR-MTD

the pseudorapidity coverage of  $|\eta| < 0.8$  [32]. The detectors cover the backlegs entirely and the space between the backlegs was kept uncovered in simulation. The azimuthal acceptance using this simulation geometry is  $\sim 56\%$  of  $2\pi$  [32]. The simulation result indicates that the particles reaching the MTD are primarily through the gaps between the backlegs, while most particles are absorbed in the material budget leading up to the BEMC.

Detailed simulations [35] were performed using the STAR detector geometry to measure the MTD detection efficiency. The simulation procedure involves extrapolation of the tracks



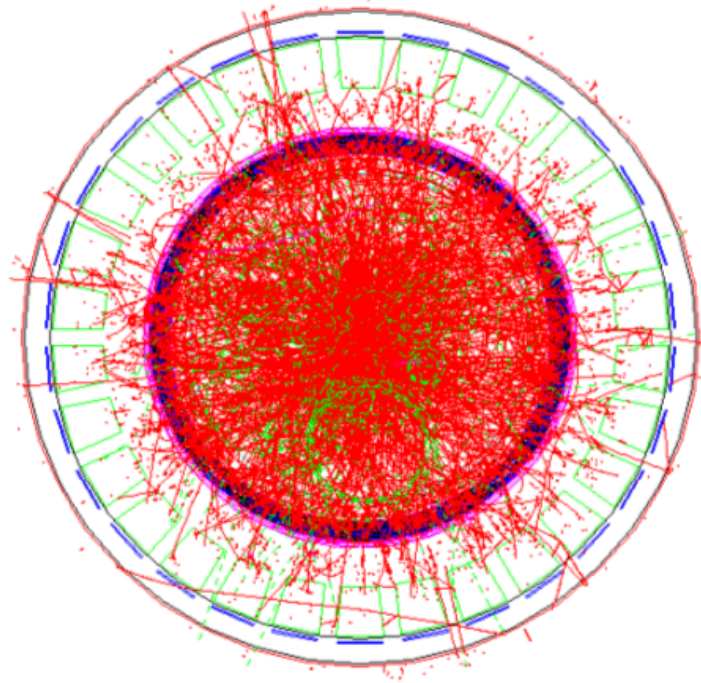


Figure 2.16: Simulation of central Au+Au collisions in the framework of the STAR geometry and material budget using the HIJING event generator [32]

reconstructed at the TPC to the MTD. Since the MTD relies on precise hit position and timing information measurement, the distance between the extrapolated MTD hit and the actual MTD hit is needed to be  $\leq 4$  cm and the difference in timing is needed to be  $< 400$  ps. For simplicity, the helix extrapolation does not take into account the presence of the magnetic field. The efficiency obtained with muons having transverse momentum,  $p_T > 2$  GeV/c as shown in Fig. 2.17 is  $\sim 40$ -50%. The low efficiency of the MTD towards muon detection can be attributed to the MTD acceptance. In an ideal scenario, pions and kaons are absorbed by the steel magnet backlegs, but in the event of decay of the pions and kaons into muons before they reach the backlegs results in misidentifications. It is clearly evident from Fig. 2.17 that the factor of proton rejection is larger compared to pions and kaons. The combined pion, kaon and proton detection efficiency is  $< 1\%$  after considering their relative yields [32]. This study highlights the hadron rejection capability of the MTD due to the strategic location of the detectors. Simulation results indicate

a rejection factor  $\sim 50$ -100 which can be improved by using tracking and ionization energy loss information from the TPC and using the TOF detector for hit matching.

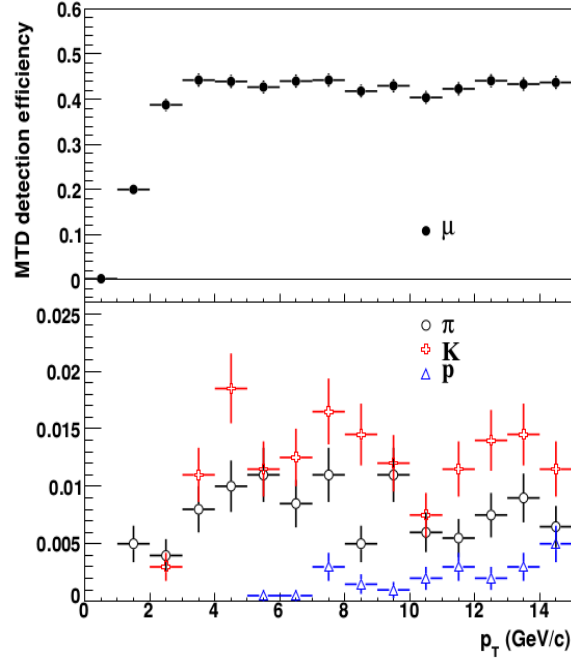


Figure 2.17: Detection efficiency for muons compared to the probability of misidentification for pions, kaons and protons [32].

### 2.3.7 Physics potential with the MTD

The combination of the STAR mid-rapidity detectors, the Time Projection Chamber (TPC), the Time-Of-Flight (TOF) and the Barrel Electromagnetic Calorimeter (BEMC) is capable of triggering and detecting di-electrons coming from the  $J/\psi \rightarrow e^+ + e^-$  decay channel. Large backgrounds in case of electrons and the lack of effective triggering especially at low transverse momentum ( $p_T$ ) are the obvious limitations to this measurement. The potential of the STAR-MTD can help to redress this issue by using di-muons. The MTD will provide high efficiency and excellent triggering for di-muons from  $J/\psi$  over a large acceptance at mid-rapidity [33] and help in a better understanding of the color screening properties of the medium with an increased number of detected  $J/\psi$  samples. The MTD detector at mid-rapidity at STAR aims

to achieve high efficiency and excellent triggering for detection of di-muons from  $J/\psi$  over the large acceptance of the STAR detector to improve the understanding of the color screening properties of the medium. An improvement in the invariant mass resolution achievable with muons from the MTD should also help in separating the different  $\Upsilon$  states (1S, 2S, 3S) and to determine the temperature of the QGP medium. The STAR and PHENIX detectors are capable of  $J/\psi$  detection via the  $J/\psi \rightarrow e^+ + e^-$  channel with the help of the electromagnetic calorimeters for triggering and identification of electrons. Fig. 2.18 shows results obtained for  $J/\psi$  efficiency as a function of transverse momentum at mid-rapidity [32] using the di-electron decay channel at PHENIX [36] and STAR. The limitation to this measurement comes from the low acceptance of the PHENIX detector and lack of electron triggering capability at low momentum for the STAR detector. In the framework of the relatively larger acceptance of the STAR detector, the MTD wishes to resolve this critical issue by providing large  $J/\psi$  samples via the  $J/\psi \rightarrow \mu^+ + \mu^-$  channel due to improved triggering.

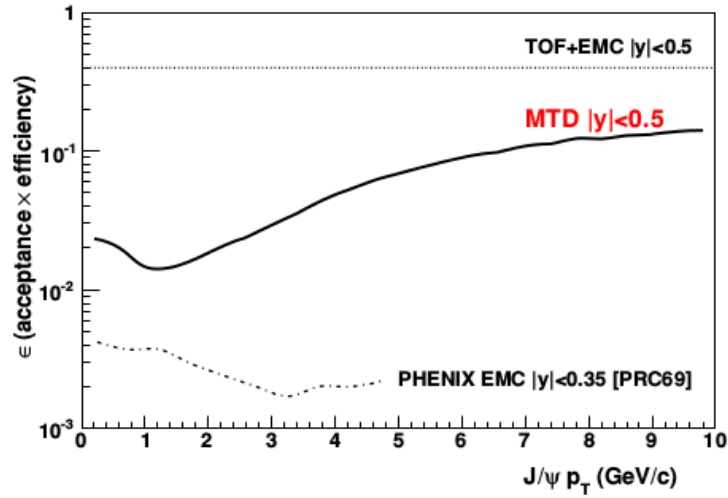


Figure 2.18:  $J/\psi$  efficiency as a function of  $p_T$  at mid-rapidity using the di-electron decay channel at PHENIX [36] and STAR [32]

Fig. 2.19 shows the simulated  $J/\psi \rightarrow \mu^+ + \mu^-$  invariant mass distribution with a signal-to-background ratio of 7:1 [32]. Simulation results for the invariant mass reconstruction of di-muons

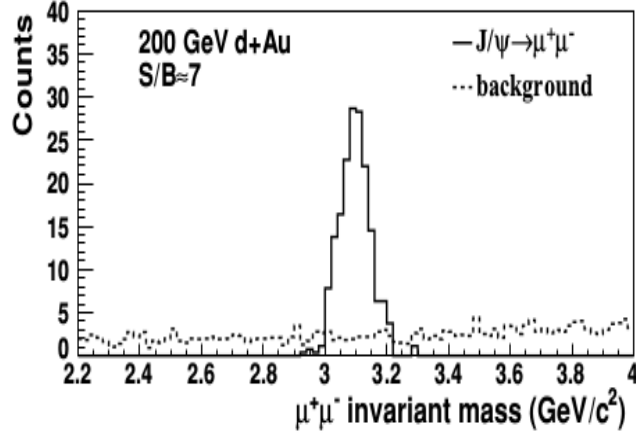


Figure 2.19: Signal to background ratio for the  $J/\psi$  invariant mass distribution obtained from simulation [32].

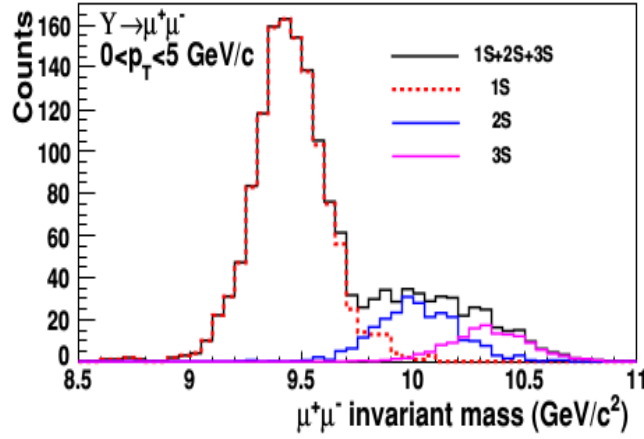


Figure 2.20: Simulation result highlighting the separation of the different  $\Upsilon$  states using the di-muon decay channel [32].

from the  $\Upsilon \rightarrow \mu^+ + \mu^-$  decay channel [32] has been shown in Fig. 2.20 and a clear separation of the three  $\Upsilon$  states (1S, 2S, 3S) is obtained due to an improved mass resolution achievable for muons. The objective of this thesis is the fabrication and testing of Multigap Resistive Plate Chambers for the STAR-MTD to facilitate the measurement of di-muons at mid-rapidity to study the yet unknown properties of QGP.

# Bibliography

- [1] M. Harrison et al., Nucl. Inst. and Meth. A 499, 235 (2003).
- [2] <http://home.cern/topics/large-hadron-collider>
- [3] <https://www.bnl.gov/rhic/> ; [http://en.wikipedia.org/wiki/Relativistic\\_Heavy\\_Ion\\_Collider](http://en.wikipedia.org/wiki/Relativistic_Heavy_Ion_Collider).
- [4] K. H. Ackermann et al. (STAR Collaboration), Nucl. Inst. and Meth. A 499, 624 (2003); J. Adams, et al. [STAR Collaboration], Nucl. Phys. A 757, 102 (2005).
- [5] K. Adcox et al. (PHENIX Collaboration), Nucl. Inst. and Meth. A 499, 469 (2003) ; K. Adcox, et al. [PHENIX Collaboration], Nucl. Phys. A 757, 184 (2005).
- [6] B. B. Back et al. (PHOBOS Collaboration), Nucl. Inst. and Meth. A 499, 603 (2003); B. B. Back, et al. [PHOBOS Collaboration], Nucl. Phys. A 757, 28 (2005).
- [7] M. Adamczyk et al. (BRAHMS Collaboration), Nucl. Inst. and Meth. A 499, 437 (2003) ; I. Arsene, et al. [BRAHMS Collaboration], Nucl. Phys. A 757, 1 (2005).
- [8] RHIC Accelerators, <https://www.bnl.gov/rhic/complex.asp>
- [9] Satoshi Ozaki and Thomas Roser, Prog. Theor. Exp. Phys. 2015, 03A10
- [10] <https://www.bnl.gov/tandem/> ; <https://www.bnl.gov/science/accelerators/TVdG.php>
- [11] M. Harrison, S. Peggs, T. Roser (2002), "The RHIC Accelerator". Annual Review of Nuclear and Particle Science 52: 425.

- [12] D. J. Gross and F. Wilczek, Phys. Rev. Lett. 30 (1973) 1343 ; H.D. Politzer, Phys. Rev. Lett. 30 (1973) 1346
- [13] C. Montag et al. CERN Yellow Report CERN-2014-004, pp.63-68 ; arXiv:1410.4076 [physics.acc-ph]
- [14] M. Harrison, T. Ludlam, and S. Ozaki, Nucl. Instr. and Meth. A 499, 235 (2003).
- [15] L C De Silva, PhD Thesis, University of Houston, USA, 2012.
- [16] Md Nasim, PhD Thesis, Homi Bhabha National Institute, India, 2014.
- [17] M. Anderson et al., Nucl. Instrum. Meth. A **499** (2003) 659
- [18] L. Kotchenda et al., Nucl. Instrum. Meth. A **499** (2003) 703
- [19] C. Adler et al. [STAR Collaboration], Nucl. Instrum. Meth. A **499** (2003) 633. ; F Bergsma et al., 2003 Nucl. Instr. and Meth. A 499 633.
- [20] W. J. Llope et al., Nucl. Instrum. Meth. A **522** (2004) 252.
- [21] Evan W Sangaline, PhD Thesis, University of California, Davis, USA 2014.
- [22] David Tlustý, PhD Thesis, Nuclear Physics Institute of the Academy of Sciences, Czech Republic, 2014.
- [23] W. J. Llope, Nucl. Instrum. Meth. A 661 (2012) S110–S113.
- [24] M. M. Aggarwal et al., Nucl. Instr. Meth. A 499, 751 (2003); M. M. Aggarwal et al., Nucl. Instr. Meth. A 488, 131 (2002).
- [25] X-N. Wang and M. Gyulassy, Phys. Rev. D 44, 3501 (1991).
- [26] B. Zhang et al., Phys. Rev. C 61, 067901 (2000).
- [27] K. H. Ackermann et al., Nucl. Instr. Meth. A 499, 713 (2003).

- [28] J. Adams et al. [STAR Collaboration], [arXiv:nucl-ex/0511026].
- [29] E. Cerron Zeballos et al., Nucl. Inst. and Meth. A 374 (1996) 132-135.
- [30] Z Xu BNL LDRD project 07-007; Beam Test Experiment (T963) at FermiLab.
- [31] STAR Muon Telescope Detector Proposal:  
[http://www.star.bnl.gov/~ruanlj/MTDreview2010/MTD\\_proposal\\_v14.pdf](http://www.star.bnl.gov/~ruanlj/MTDreview2010/MTD_proposal_v14.pdf).
- [32] L Ruan et al., J. Phys. G: Nucl. Part. Phys. 36 (2009) 095001.
- [33] C. Yang et al. [STAR Collaboration], Nucl. Instr. Meth. A 762 (2014) 1
- [34] M Beddo et al., 2003 Nucl. Inst. and Meth. A 499 725.
- [35] Lin G (for the STAR Collaboration) 2006 A New Large-area Muon Telescope Detector at Mid-rapidity at RHIC, talk presented at DNP 2006, Nashville, TN, 25–28 October.
- [36] S S Adler et al 2004 Phys. Rev. C 69 014901.

## Chapter 3

# Development of Multi-gap RPCs (MRPC) for the STAR experiment

This chapter focusses on the discussion about gaseous ionization detectors. The emphasis has been on the evolution of the parallel plate design and the Resistive Plate Chamber (RPC). The Multigap RPC (MRPC) design, which has been a natural progression in this field of detectors to improve timing resolution has been discussed in detail alongwith the fabrication and test results of the MRPC's for the STAR-MTD project. A spin-off benefit of the detector R&D for the MTD project is to study the feasibility of MRPC's as detectors in TOF-PET imaging. A preliminary effort in this direction, the fabrication and testing of small-sized MRPC prototypes with a positron-emitting  $^{22}\text{Na}$  source, has been presented here.

### 3.1 Gaseous ionization detectors

Detectors are devices that detect the presence of charged particles and/or electromagnetic radiation produced in high energy and nuclear physics experiments or from cosmic radiation. The first detection of ionizing radiation dates back to the 1890's when Röntgen during his discovery of X-rays and subsequently Becquerel, during his accidental discovery of radioactivity, used



photographic plates as the detection tool. The ionizing property of X-rays were used to good effect by Madame Curie and later on by J. J. Thomson. The detection of charge liberated due to ionization necessitated a medium in which the charges could drift away from the point of generation under the influence of an electric field. This prioritised the choice of ‘Gas’ as the sensitive medium and hence the development of gas-filled detectors started.

The first gas-filled detector, the ‘Ionization Chamber’, used this principle of collecting charge liberated by X-rays in a gaseous medium in the presence of an electric field. The intensity of the ionizing radiation was found to be proportional to the amount of radioactive material used. The ionization chamber was used by Hess in 1910 for the discovery of cosmic rays [1]. Rutherford laid the foundation to gaseous ionization detector development for detecting ionizing radiation. His pioneering research led to a better understanding of the working principle of gas detectors. Rutherford and Geiger built the first cylindrical gas-filled device that made use of a metallic wire as an anode inside a cylindrical gas-filled cathode in the year 1908 [1][2]. The electrons released in the gas due to ionization drift towards the metallic wire anode under the influence of a potential difference between the electrodes. In the process, as the electrons reach the vicinity of the wire the electric field intensifies and the number of inelastic collisions undergone by the electrons increases exponentially. This exponential multiplication of electrons in the presence of a strong electric field is termed as the Townsend Avalanche, named after John Townsend for his extensive research on charge multiplication in gases due to collisions in the presence of strong electric fields. The detected charge signal is amplified as a result of the avalanche and is proportional to the charge created via primary ionization by the radiation incident on the detector. The gas detector developed by Rutherford and Geiger was hence adequately named as the ‘Proportional Counter’ [2]. Geiger and Müller developed a new detector based on the same principle in the year 1928. The detector was called the ‘Geiger-Müller Counter’ or simply, the ‘GM Counter’. The detector was robust and inexpensive and due to larger amplifications achievable with this detector as it was operated at higher electric fields, detection of single electrons was made possible [1][2]. With the passage of time and with the advancement of technology, the readout technology has

improved leaps and bounds compared to the rudimentary instrumentation existent during the development of these detectors.

Electromagnetic interaction is the most probable way in which charged particles interact with the gaseous medium. The passage of an energetic charged particle leads to ionizations in the gas medium and creation of electron-ion clusters. The phenomenon is called primary ionisation. If the primary electrons possess energy higher than the ionization potential of the gaseous medium, they create secondary electron-ion pair via ionizations. Gas detectors [3][4] work on this principle of ionisation and the direct collection of the ionisation electrons and ions produced by radiation passing through a sensitive (gas) medium. The mean number of electron-ion pairs created is directly proportional to the amount of energy deposited in the chamber by the through-going charged particle. The electron-ion pairs drift through the electric field towards the anode and cathode respectively where they are subsequently collected. On reaching the anode, the electrons pass through a resistor giving a voltage signal proportional to the charge deposited. The different regimes of gas detector operation based on the applied high voltage and the number of ion pairs collected has been discussed below [4].

At low applied voltages, when the electric field strength is insufficient to prevent recombination, the created electron-ion pairs recombine with each other. This is the *Recombination* region and the no. of ion pairs collected is less than that actually created.

With the increase in voltage, there is a suppression in the recombination of the ion-pairs and the total ionization produced by the through-going radiation is collected without any charge amplification. This is known as the region of *Ion Saturation* and the principle on which Ionisation chambers work. Signal pulse amplitude being extremely small, this mode requires sophisticated electronics for the measurement of radiation.

Beyond the ionization region, an increase in voltage leads to the onset of gas multiplication as the threshold field for secondary ionization ( $10^6$  V/m) is overcome [4]. Charge amplification results in a proportionality between the number of incident and collected ion pairs and it is reflected through a linear amplification of signal pulse amplitude with the increasing number of

created ion pairs. This region of *true Proportionality* is the operating regime of the Proportional counter.

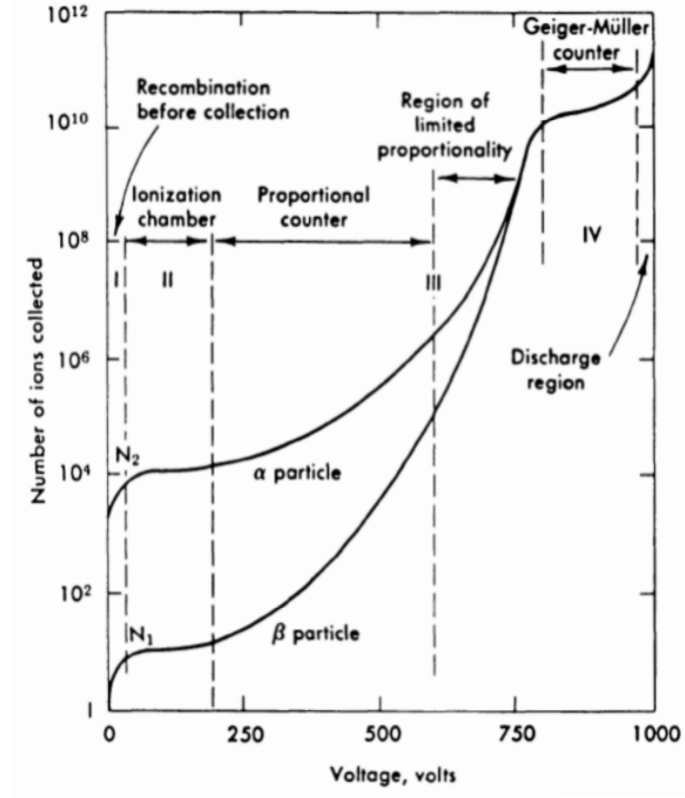


Figure 3.1: Modes of operation of gas detectors, in terms of the number of ions collected as a function of the applied voltage [3].

Upon further increasing the voltage, the linearity of operation is lost. At such high electric fields, the electrons are collected quickly on the cathode while a positive ion cloud is created within the gas gap owing to their larger mass and slower drift velocity. This space charge effect leads to a distortion of the applied electric field. This electric field dependent gas multiplication is the cause of the non-linearity observed in this mode of operation and hence the name region of *Limited Proportionality*. An increase in the number of created ion-pairs leads to an increase in the signal amplitude, but the dependence is non-linear. The avalanche mode of operation of Resistive Plate Chambers is in the region of limited proportionality.

At voltages beyond the region of limited proportionality, the space charge becomes the dom-

inating effect. A saturation is reached and the process of avalanche multiplication becomes self-limiting. Multiplication proceeds upto the extent where a certain number of positive ions build up a space charge within the detector that reduces the electric field such that further amplification is prohibited. Thus, the final detector output is independent of the incident radiation. This mode of operation is called the *Geiger-Mueller* mode and the region in which the GM counter works. The detector basically works as a counter of incident radiation without providing any information about its nature as it fails to differentiate between incident radiation of different energies.

An increase in the applied high voltage beyond the Geiger Mueller mode brings us to the *Discharge mode*, which is characterised by continuous discharge. Hence, this region is not used for detector operation. Fig. 3.1 is an illustration of the different regimes of operation of gas detectors.

The basic attributes of a gas detector are :-

- Efficiency : The efficiency of a gas detector is defined as the ratio of the number of particles detected to the total number of particles incident on it.
- Position Resolution : It is defined as the ability of the detector to localize particle trajectory within a small region.
- Time Resolution : The ability of a gas detector to distinctly detect two particles incident on the detector with a time separation is defined as its time resolution.
- Dead Time : The least attainable difference in time between consequent resolved hits on the same readout pad or channel of the detector is defined as the dead time.

The ease of construction, efficient handling and the economic nature of Gas detectors along with their excellent efficiency, timing and position resolutions make them front-runners for large area detection systems in high energy and nuclear physics experiments. The evolution of this field down the years has led to the development of more complex detectors that are efficient

and better in terms of performance compared to their primitive counterparts. The fill gas composition, detector operating conditions, the mode of operation, materials to be used for detector fabrication and detector geometry are optimised based on experimental requirements. A variety of gas-filled detectors are being used in experiments worldwide based on requisite detector parameters like rate capability, efficiency, timing and position resolution [5][6].

### 3.2 Evolution of the Parallel Plate Design in Gas detectors

The early gas detectors had cylindrical geometry, with a metallic wire kept at a large positive potential as the anode, while the surface of the metallic cylindrical tube kept at ground potential served as the cathode. Noble gases like Argon, or a mixture of Argon and a quench gas were typically used as the fill gas in these detectors. The purpose of the quench gas which is chosen to have high rotational degrees of freedom is to absorb the Ultraviolet (UV) photons, thus limiting the spread of the avalanche. The radial electric field  $E(r)$  due to the cylindrical geometry has a strong  $\frac{1}{r}$  dependence on the distance ( $r$ ) from the wire. Naturally, the field is most intense in the vicinity of the anode wire, at a distance of the order of the wire diameter. The avalanche multiplication happens once the electrons generated via ionization drift to this region of high electric field. The fluctuations in drift times results in poor timing resolution [6][7]. In order to achieve better time resolution, the planar geometry was considered. Planar geometry ensures a strong and uniform electric field throughout the sensitive area of the detector. Whilst electrons in case of a cylindrical wire chamber need to drift towards the high electric field region in the vicinity of the anode wire for avalanche multiplication to set in, parallel plate electrodes ensure instant avalanche multiplication of primary clusters created via ionization. As a consequence, the delay in signal formation due to electron drift times is averted and parallel plate detectors have excellent time resolution. In this case, the timing jitter is solely influenced by the fluctuations in the primary ionization, the avalanche growth times and the avalanche statistics [8][9]. The avalanche growth and the signal formation shall be revisited in a later section and discussed in greater detail for the parallel plate geometry. A brief history of the use of the parallel plate

design has been discussed in the following sections to shed light on the challenges faced and methods used to improve the detector parameters.

### 3.2.1 The Keuffel Spark Counter

The first gas-filled detector to utilize parallel plate electrodes and a uniform, high electric field is the Keuffel Spark Counter [10][11]. A uniform electric field of 1-3 kV/2.5 mm is provided by high voltage applied between two parallel Copper electrodes with a gas gap of 2.5 mm. A mixture of Argon and Xylene kept at a pressure of  $\sim 500$  mbar acts as the sensitive medium. A through-going charged particle ionizes the gas and the uniform electric field immediately triggers the avalanche multiplication. The charge build-up inside the gas gap develops into streamers and sparks. Although the uniform electric field improves the time jitter, the metal electrodes pose the disadvantage of getting short-circuited by the sparks. This shortcoming is overcome by using a switching-off circuit, that stops sparks from shorting the electrodes at the expense of detector rate capability. Large area operation of the counter is impossible as the spark discharge energy being proportional to the chamber area, damages the metallic electrodes. The typical dead times measured for the Spark Counter are a few ms, required to recharge the electrodes via the high voltage power supply. This detector has a much improved time resolution ( $\sim 1$  ns) compared to the resolution achievable with the GM Counter ( $\sim 100$  ns) [8].

### 3.2.2 The Pestov Spark Counter (PSC)

The Pestov Spark Counter [12][13] shown in Fig. 3.2, is a gas-filled, parallel plate detector with an extremely small gas gap  $\sim 100$   $\mu\text{m}$ . Unlike the conductive electrodes used by Keuffel, this detector was the first to make use of resistive electrodes. The resistive anode used in this detector is a special glass plate of volume resistivity  $10^{10}$   $\Omega\text{-cm}$ , while the other electrode was metallic. In the presence of the strong electric field, the avalanche transforms into a streamer but the detector does not run the risk of getting short-circuited. The streamer affects only a limited region of the anode due to its high resistivity, while the rest of the detector remains active.

The gas mixture used for the operation of this detector had high UV absorption capability that prevents UV photons from spreading the discharge.

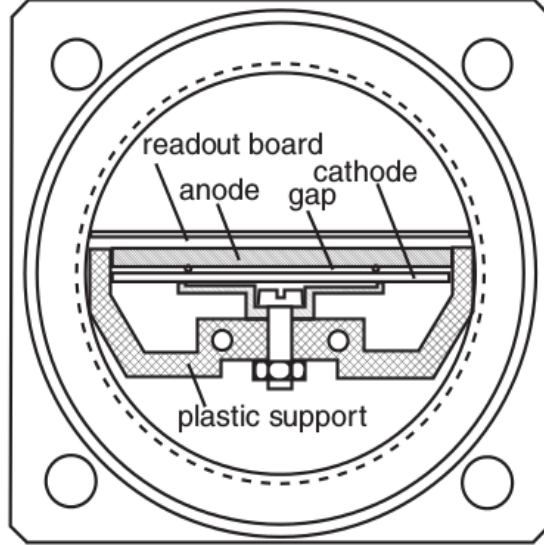


Figure 3.2: Schematic diagram of the Pestov Spark Counter [14].

Very high detection efficiency is achieved by mounting the detector on an aluminium vessel, maintaining it at a large pressure of 12 bar which ensures large primary ionization in the small gas gap. A timing resolution as good as  $\sim 35$  ps is obtained by the detector along with an excellent noise rate of  $\sim 0.2$  Hz/cm<sup>2</sup> [14][15]. The limitations of the detector arise from the mechanical constraints imposed on its operation (high pressure) and the lack of availability of the non-commercial glass electrode.

### 3.2.3 Parallel Plate Avalanche Chamber

The Parallel Plate Avalanche Chamber (PPAC) is a gas-filled detector with a gap thickness of  $500\ \mu\text{m}$  to  $2\ \text{mm}$  maintained with suitable spacers between electrodes. The detector uses a variety of electrode material, from metallic plates to metallized ceramics and plastics. As is evident from the name, this parallel plate detector operates in the avalanche mode unlike the streamer/spark mode (to be discussed in detail in Sec. 3.3.3) operation of its predecessors. The

avalanche mode operation maintains a low device gas gain of  $\sim 10^3$  to  $10^5$  with a proper fill gas choice and prevents streamer formation. This keeps the discharge probability of the detector for minimum ionizing particles down to  $10^{-5}$  and improves the rate capability upto  $10 \text{ MHz/cm}^2$  [16]. The other advantage is the timing resolution of the detector  $\sim 100$  to  $250 \text{ ps}$  [17][18]. The operation at a low gain has limitations in terms of small signal strength ( $\sim 1 - 10 \text{ fC}$ ) [18] that affects detector efficiency and the signal-to-noise ratio. The detector fabrication is non-trivial and the large scale use of the PPAC technology is questionable due to the above limitations [19].

Keeping in mind the limitations of the previous generations of parallel plate detectors, R. Santonico and R. Cardarelli in the year 1981 conceived a new detector called the Resistive Plate Chamber [20] and used resistive plates for its construction. The RPC is the basis of this thesis and has been discussed in detail in the next few sections.

### 3.3 Resistive Plate Chamber (RPC)

Designed as a better alternative to the Parallel Plate Avalanche Counter, the Resistive Plate Chamber (RPC) is fabricated with resistive plates as electrodes. Locally available, inexpensive materials like Glass and Bakelite (phenolic paper laminates) which typically have high volume resistivity ( $\sim 10^9 - 10^{12} \text{ } \Omega\text{cm}$ ) are chosen as electrodes. The gas gap is defined using polycarbonate spacers of high resistivity ( $> 10^{13} \text{ } \Omega\text{cm}$ ) sandwiched between the two resistive electrodes. The through-going charged particle ionises the gas which leads to an avalanche in the presence of the strong electric field. Highly resistive electrodes prohibit the flow of electric charge from the high voltage power supply to maintain this discharge. The discharge between the plates is therefore quickly quenched via a drastic reduction in the electric field in a small area. Typical discharge time scales are  $\sim 10 \text{ ns}$  while the charging up of the plates depends on the time constant ( $\tau$ ),

$$\tau = \rho \epsilon_0 \epsilon_r \quad (3.1)$$



which depends on the electrode volume resistivity ( $\rho$ ) but is independent of the detector dimensions [5][6][21].  $\epsilon_0$  and  $\epsilon_r$  are the dielectric constant of the gas and permittivity of free space respectively.

As an example, the time constants for the bakelite ( $\rho \sim 10^{10} \Omega\text{-cm}$ ) and glass ( $\rho \sim 10^{12} \Omega\text{-cm}$ ) electrodes are  $\tau \sim 10$  ms and  $\tau \sim 1$  s respectively [6][8].

As the charge-up time is much higher compared to the discharge time, the area of the detector affected by the discharge ( $\sim 0.1 \text{ cm}^2$ )[20], called the dead area, behaves as an insulator and remains inactive during this period of time ( $\tau$ , the dead time). The remaining area of the detector, however, is unaffected and retains its sensitivity to charged particles. This property of resistive electrodes vastly improves their rate capability. The fact that bakelite electrode resistivity is  $\sim 100$  times less than glass electrodes, the rate capability of detectors using bakelite electrodes is proportionately higher. Glass electrodes with low resistivity values are being used currently for high-rate applications.

A schematic of a single gap RPC is shown in Fig. 3.3. Built using parallel plate electrodes of either glass or bakelite, electrodes are separated by polycarbonate spacers to define the uniform gas gap.

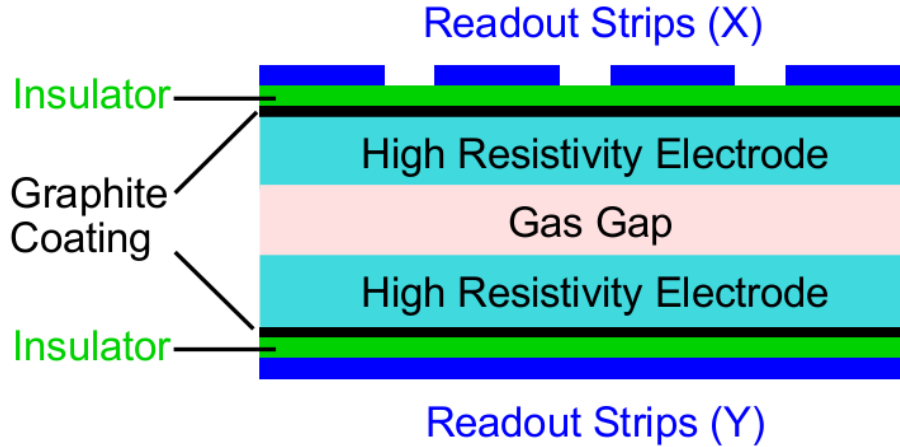


Figure 3.3: Schematic diagram of a basic Resistive Plate Chamber taken from [8]

The high voltage is applied to the outer surface of the electrodes via conducting contacts that produces a uniform electric field in the gap. A thin graphite layer of surface resistivity  $\sim 1 \text{ M}\Omega/\square$  is painted on the external surface of the electrodes to permit the application of high voltage. The avalanche multiplication of the electrons and the movement of the charges inside the gap induces a signal on external metallic pick-up strips. The pickup strips behave like transmission lines and are isolated from the HV electrodes with a layer of insulator. Signals in gaseous detectors are induced signals due to the motion of charges within the sensitive volume and the signal persists till the charges arrive at the electrodes [2]. The readout strips on the two sides of the chamber can be placed perpendicular to each other, to provide the x- and y-co-ordinate of the through-going charged particle. The mode of operation of the detector which has been discussed in a later section determines the sensitive gas mixture to be used and the voltage to be applied on the detector.

The schematic shown in Fig. 3.4 highlights the difference between detectors with cylindrical geometry and parallel plate geometry in terms of avalanche growth and signal generation.

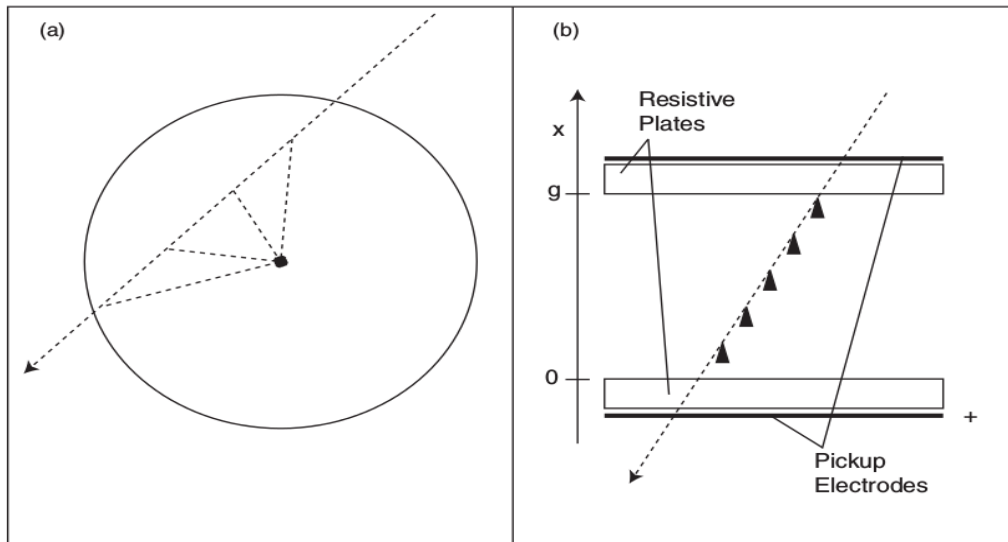


Figure 3.4: Illustration of the difference in avalanche growth and signal generation between a) a cylindrical wire chamber and b) a parallel plate detector [14]

RPC's have better timing resolution compared to cylindrical wire chambers. This arises

from the uniform electric field in RPC's which results in instant avalanche multiplication as opposed to the  $\frac{1}{r}$  field dependence in wire chambers that introduces time fluctuations due to the drift of electrons to regions of strong electric field close to the anode wire for the initiation of the avalanche. Separate subsections in the thesis have been dedicated to discussions about the avalanche multiplication and signal generation in an RPC, specifically in a detector of 2 mm gas gap and the different modes of operation.

### 3.3.1 Choice of the Fill gas used in RPC's

The gas gap acts as the sensitive medium for particle ionization in a gas detector. The choice of the fill gas for an RPC, or for that matter any gas detector, is critical. The phenomenon of avalanche multiplication develops in practically all gases and hence any gas or a mixture of gases can ideally be used as the sensitive medium. However, there are certain criteria that must be satisfied, e.g operation at low voltage, high gas gain, high rate capability, extended lifetime, swift recovery [22]. Noble gases that do not take part in chemical reactions are ideal choices for fill gas as their high specific ionization at low electric fields for charged particles, ensures a low operating voltage. Argon being the least expensive in the family of noble gases, serves as the perfect choice for the ionizing component. Detector operation with only Argon as the sensitive component has the disadvantage of transition to the discharge mode at gas gains  $\sim 10^3$ - $10^4$ . During the passage of through-going radiation, ionization and excitation of Argon atoms occurs simultaneously. The excited Argon atoms return to the ground state via radiative processes. The emitted photons create undesirable secondary ionizations within the gas gap that enhance avalanche to streamer transition probability. This feature prompted the use of polyatomic molecules with rotational or vibrational degrees of freedom that dissipate the photon energy via non-radiative processes, thus enabling detector operation at high gas gains. These gases are called quenchers. A mixture of a noble gas and a quench gas (e.g Methane-CH<sub>4</sub>, Isobutane-i-C<sub>4</sub>H<sub>10</sub>) allows stable detector operation at high gas gain. An electronegative additive is introduced in the gas mixture to serve as the electron quencher. Their primary function is to quench energetic electrons and

prohibiting them from creating new avalanches elsewhere in the sensitive medium [22]. Freon and SF<sub>6</sub> are best examples of electron quenchers used in gas detector gas mixtures, especially RPC's. The high atomic mass and cluster density of Freon, makes it a suitable ionizing gas for small-sized gaps operated in the avalanche mode. The large number of primary ionization electrons, especially the number created closest to the cathode produces detectable avalanches and maximises detection efficiency. A gas mixture containing Freon as the ionizer (R134A, eco-friendly), i-C<sub>4</sub>H<sub>10</sub> as the photon quencher and traces of SF<sub>6</sub> as the electronegative electron quenching component serves well for the avalanche mode of operation of MRPC's.

### 3.3.2 Avalanche Multiplication and Signal generation in RPC

The basic signal generation principle in case of gas-filled detectors like the RPC is based on ionization in the gas and the avalanche multiplication of the electrons [23]. In the presence of strong electric field (few kV/cm), the liberated primary electrons are accelerated to sufficient energies to create further ionizations in the gas gap. This phenomenon of multiplication of free electrons created via ionisation is termed as the Townsend avalanche. Due to the distinct drift velocities of electrons and ions (a factor of 10<sup>3</sup> higher for electrons) [7], owing to their much smaller mass, the shape of an avalanche is like a liquid-drop (Fig. 3.5), with a tail of positively-charged ions and electrons located at the head.

The Townsend equation governs the fractional rise per unit path length of electrons and is given as :

$$\frac{dn}{n} = \alpha dx \quad (3.2)$$

where,  $\alpha$  is the first Townsend coefficient for the gaseous medium. The value of  $\alpha$  is otherwise field dependent, but, for the parallel plate scenario of uniform electric field, its a constant. The solution of Eq. 3.2 yields the number density of electrons as a function of distance as follows :

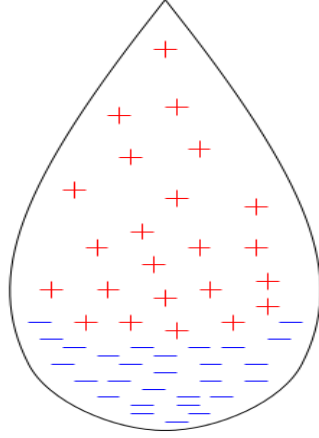


Figure 3.5: Schematic diagram of a liquid-drop shaped avalanche [25].

$$n(x) = n_0 e^{\alpha x} \quad (3.3)$$

where,  $n_0$  is the initial number of electrons and  $x$  is the distance between the anode and the point where the primary ionization cluster is created. The number of electrons in an avalanche, therefore, increases exponentially. Let us take the example of a standard RPC of 2 mm gap thickness ( $d$ ) subject to a strong uniform electric field ( $E$ ). As equation 3.3 suggests, the total number of electrons created in an avalanche depends on the distance  $x$ . So, naturally, an electron starting to avalanche from the cathode, that traverses the whole gap thickness of 2 mm will accumulate a greater number of electrons in its course and hence generate more charge compared to the case when the avalanche starts at a distance of 0.5 mm from the cathode. This fact has been suitably illustrated in Fig. 3.6.

The majority of the electrons and ions are created at distances close to the anode during the course of the avalanche. Electrons drift quickly towards the anode and induce the fast component ( $q_{fast}$ ) of the signal. The slow moving ions drift towards the cathode and induce the slow component ( $q_{slow}$ ) of the signal. The total induced signal ( $q_{total}$ ) is the sum of the fast and

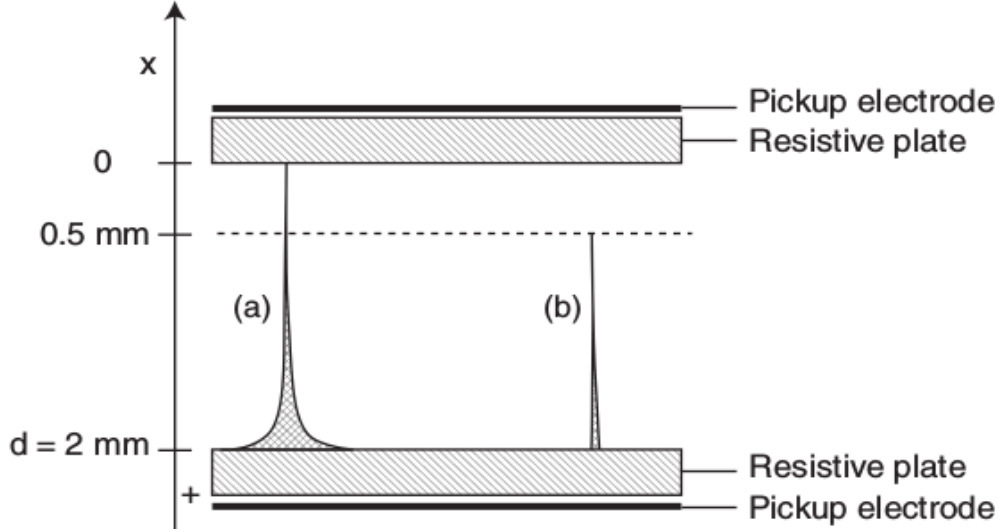


Figure 3.6: Charge development in a 2 mm gap RPC with the avalanche multiplication starting at two different positions a) the avalanche starts at  $x = 0$  and traverses the entire 2 mm gas gap and b) the avalanche creation is at  $x = 0.5$  mm from the cathode and travels 1.5 mm in the gas gap [14]

the slow components and is related to the fast signal as [24].

$$q_{fast} = \frac{q_{total}}{\alpha \cdot d} \quad (3.4)$$

As will be discussed in detail in the following section, to maintain the avalanche mode of operation the limiting value of  $\alpha \cdot d$  should be  $\sim 20$ . This limiting value is obtained when the electron avalanches the entire gap thickness and the number of electrons generated in the avalanche as given by Eq. 3.3 is  $\sim 10^8$ . This is equivalent to a total charge of 16 pC within the gap and a fast signal component equivalent to 800 fC. Similarly, when the primary ionization takes place 0.5 mm away from the cathode and the electron avalanches a distance of 1.5 mm within the gas gap, it generates  $\sim 10^6$  electrons ( $\alpha \cdot d \sim 15$ ), a total charge equivalent to 160 fC or a fast signal component of 8 fC. It is extremely difficult to detect this signal as it is below the threshold level of most RPC front-end electronics. Therefore, the truer picture of signal

generation in an RPC is that only when primary ionization is within 0.5 mm of the cathode (for a 2 mm gap RPC), a detectable RPC signal is produced and the notion that the RPC signal is a sum of multiple avalanches is incorrect [14].

### 3.3.3 Modes of operation

A Resistive Plate chamber can be operated in two different modes, the Avalanche mode (also called the limited proportionality mode) and the Streamer mode. As previously discussed, radiation passing through gas detectors creates primary ionization, which in the presence of strong electric fields undergoes multiplication till the subsequent formation of a Townsend Avalanche.

A schematic description of the avalanche mode of operation can be found in Fig. 3.7.

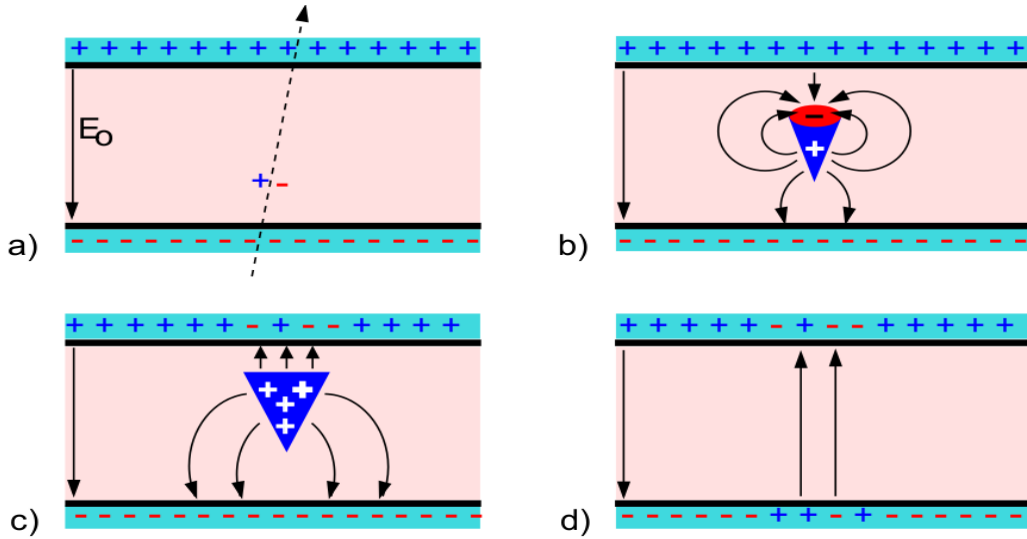


Figure 3.7: Avalanche development in an RPC detector a) Primary ionization of gas atoms by through-going radiation culminating in a Townsend Avalanche in an electric field  $E_0$  b) Avalanche dynamics starting to influence the electric field c) Owing to the large differences in mass, electron drift velocity is considerably higher than ions and the electrons and ions reach respective electrodes at different times. d) When ions finally reach the cathode, the discharge affects a small area of the electrodes due to its high resistivity, around the region of avalanche development [8].

Following the discussion in the previous section, the number of avalanche electrons( $n$ ) produced within the gas is given in Eq. 3.3. The equation is slightly modified, if the attachment

of electrons in the gas during their drifting motion in the presence of electronegative gases is considered.

$$n(x) = n_0 e^{(\alpha-\beta)x} = n_0 e^{\eta x} \quad (3.5)$$

where  $\beta$  is the absorption co-efficient and  $\eta (= \alpha - \beta)$  is the effective Townsend co-efficient. The amplification factor (gain) of the detector is defined as

$$M = \frac{n}{n_0} = e^{\eta x} \quad (3.6)$$

The factor M is distinctly different for the two modes of operation. An important aspect of the avalanche mode of operation is to avoid secondary ionisations and thus prevent streamers, necessitating detector operation with  $M \ll 10^8$ . The avalanche to streamer transition occurs beyond the phenomenological Raether limit [26], when the number of electrons exceeds  $10^8$ . Eqn. 3.6 suggests that this upper limit on the amplification factor, puts a limiting condition on the value of  $\alpha \cdot d \sim 20$  (for the simplest case, assuming  $\beta=0$ ). Keeping in mind the statistical fluctuations involved in the electron energy distribution and correspondingly on the value of the detector gain (M), avalanche mode of operation requires an average gain  $\sim 10^6$ .

At higher values of the detector gain, there is a significant contribution from photons towards avalanche development leading to the evolution of a streamer. The Streamer mode operation of the detector is at  $M > 10^8$  and is shown schematically in Fig 3.8.

In accordance with Pestov, a planar detector like the RPC, with resistive electrodes can be represented as a collection of discharge cells, which to a first order of approximation, behave independently [6]. A planar capacitor of area S, gap thickness d and permittivity  $\epsilon$  has a capacitance (C) :

$$C = \frac{\epsilon S}{d} \quad (3.7)$$



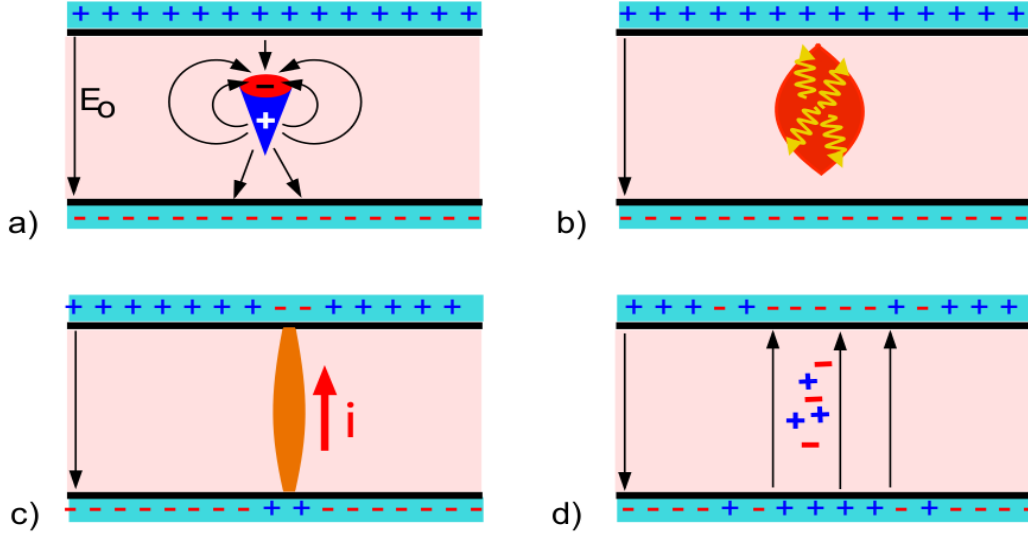


Figure 3.8: Development of a streamer in an RPC a) A townsend avalanche developing after the passage of radiation b) At such high values of gas gain, enormous charge in the sensitive volume of the detector modifies the external electric field strongly. Photons also play a major role in spreading the avalanche and streamer evolution c) Formation of a conductive channel between the electrodes leads to sparks and discharge of wider regions of the electrodes d) The discharge causes a reduction of the electric field at the avalanche spot creating a dead area [8].

The area of the cell and the average total charge ( $Q$ ) created in the gap are related as

$$S = \frac{Qd}{\epsilon V} \quad (3.8)$$

In the avalanche mode, due to the lower gains, the signal pulse is smaller, and the average total charge  $\sim 1$  pC. Whereas in the streamer mode, the high detector gain produces large average total charge  $\sim 100$  pC [5][6]. The value of total charge is directly proportional to the surface area of the discharge cells as seen from Eqn. 3.8. Smaller values of  $Q$  in case of the avalanche mode, affect smaller regions of the electrodes and hence ensure better rate capability ( $\sim \text{kHz}/\text{cm}^2$ ) compared to the streamer mode ( $\sim$  a few hundred  $\text{Hz}/\text{cm}^2$ ) [8].

The large signal amplitude in case of the streamer mode is advantageous in the sense there is no need of amplification and signal readout is easy. The avalanche mode of operation requires sophisticated low-noise electronics owing to the smallness of the signal pulses.

### 3.3.4 The advent of the Multi-gap RPC (MRPC)

The basis of a gas detector having excellent timing resolution is the creation of fast detectable signals due to rapid avalanche growth. This ideally means operation at a high gas gain to ensure fast signal production. At such high electric fields, in order to prevent the rapid growth of avalanches in the gas gap and their transition into streamers, there needs to be some kind of protective mechanism to inhibit the transition and safeguard the detector. The addition of resistive plates to subdivide the gaps is the best possible solution. This multigap system not only provides necessary boundaries through the intermediate plates to prevent avalanche growth, the high resistivity of the plates ensures transparency to the detector signals induced on external metallic pickup plates. Movement of charges in any of the sub-gaps induces a signal [14]. As has already been discussed, generation of detectable avalanches requires primary ionisation closest to the cathode [28]. The variation in the initial primary ionization cluster position is what defines detector time resolution. The subdivision of the gas gap substantially reduces the time jitter and improves detector time resolution [27]. The Multi-gap design achieves a longer efficiency plateau and higher rate capabilities [28]. The schematic in Fig. 3.9 illustrates how the single gap is subdivided into multiple smaller gaps by the introduction of resistive plates, a design named as the Multi-gap Resistive Plate Chamber (MRPC).

Fig 3.9 shows the schematic of a 5-gap MRPC comprising 6 electrically floating equi-spaced resistive plates. The two outermost electrodes are graphite-painted for the application of the high voltage. Similar to the single gap design, the read-out strips located on the external surfaces of the outermost electrodes are isolated via an insulating material like Mylar. The internal plates initially assume correct voltages electrostatically upon the application of the high voltage. The plates are maintained at the right voltages by a feedback mechanism - flow of electrons and ions in opposite directions - that takes effect within the gas gap, establishing exact gain in all sub-gaps. The rate of avalanche formation being equally probable in each identical gap with an identical electric field, the passage of electrons on a side of the resistive plate is counterbalanced by the passage of positive ions on the other side of the same plate. Hence, the net passage of

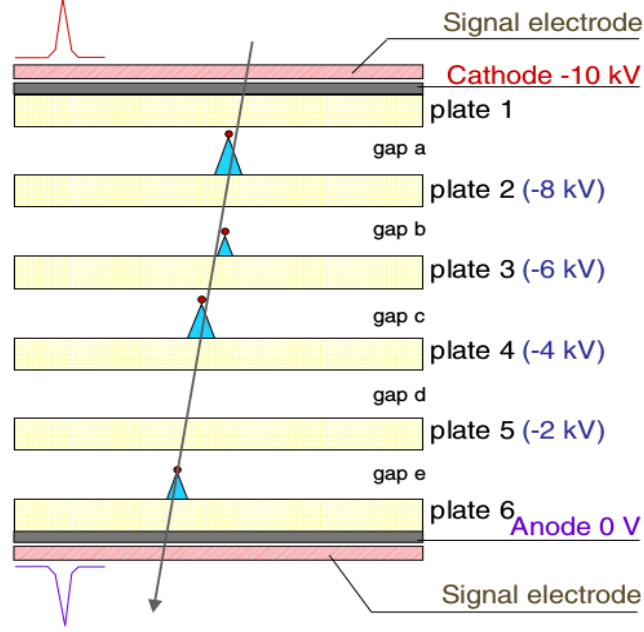


Figure 3.9: Schematic diagram of a Multi-gap RPC [14]

charge at a given time on any of the internal electrodes is zero. Any accidental deviation of voltage on the plates (from the set value) changes the electric field of the adjacent gaps. The change in the gas gain of the adjacent gaps modifies the electron and ion flow in a way so as to neutralize the voltage change via the feedback mechanism.

As per the calculations shown in [29], the timing resolution ( $\sigma_t$ ) of an RPC is defined as

$$\sigma_t = \frac{1.28}{(\alpha - \beta)v_d} \quad (3.9)$$

where,  $\alpha$ ,  $\beta$  and  $v_d$  are the Townsend co-efficient, attachment co-efficient and electron drift velocity respectively. For the specific case of smaller gas gaps, in order to be able to create detectable avalanches, the value of  $(\alpha - \beta)$  should be higher and the higher electric field across the smaller gap would naturally mean higher electron drift velocity. Therefore, the improvement of timing resolution in case of an MRPC with smaller gas gaps is fairly straightforward from

Eqn. 3.9. In case of single gap RPC's, gap width precision is extremely critical, otherwise, there is a large variation in detector gain. Gas gap tolerance should ideally then be even more critical in case of MRPC's with gaps as small as  $\sim 250\mu\text{m}$ . Moreover, the large charge generated within the gaps in case of MRPC's, should see a rise in current flow through the resistive plates culminating in rate effects. Contrary to this belief, MRPC's do not experience undue rate effects. The principal reason behind this is the space charge effect in the gap [14]. During the progression of an avalanche, as already shown in Fig. 3.5, the positive ions lagging behind at the tail of the avalanche, shield the electrons at the head from the electric field due to the applied high voltage. This reduction in electric field decreases the gas gain and limits further avalanche growth. Particularly in case of smaller gas gaps, the compactness of the avalanche, makes space charge the dominating effect and prevents the avalanche to streamer transition by limiting the number of avalanche electrons to  $\sim 10^7$ . Simulation studies done by Lippmann and Riegler discuss at length about space charge effects [30][31]. So now, imperfections in the gas gap could either lead to an increase in the electric field or otherwise. Increase in the electric field strength causes faster avalanche growth until the onset of space charge effects within the gap restricts avalanche growth. As the number of electrons in the avalanche are maintained below the Raether limit, a transition into the streamer region is prohibited and rate capability of the detector is unaffected. If the electric field somehow decreases in a certain region of the gap, the field-dependent Townsend co-efficient ( $\alpha$ ) increases and the attachment co-efficient ( $\beta$ ) decreases with it. As a consequences, the number of ions inside the gap increases (both positive and negative) and this excess charge should lead to increase in the currents flowing through the plates and a greater voltage drop across the plates. This should automatically reduce the detector rate, however, as has been shown in [32], a recombination of the positive and negative ions in the small MRPC gas gaps fails to cause any additional voltage drop across the plates and leaves the rate capability of the detector unaffected.

### 3.3.5 Applications of Resistive Plate Chambers - single gap and multi-gap

The Resistive Plate Chambers are being extensively used now-a-days as a detector for high energy physics experiments. The reasons are as follows:-

- RPC's are built from simple, low cost materials, readily available (e.g glass and bakelite) in the market.
- Fabrication and operation of these detectors is fairly simple and the fabrication cost per unit area is quite low, compared to other detectors offering similar performances.
- Read-out of detector signals alongwith obtaining a two-dimensional readout (x- and y- from the same chamber) is relatively simple.
- Coverage of large areas, high detection efficiency(>90%) and long-term stability.
- Excellent timing resolution ( $\sim 2$  ns for single gap and  $\sim 50$  ps for multi-gap), particle tracking capability and good position resolution.

The mode of operation of an RPC is application-specific. In the streamer mode, especially suited for triggering purposes, RPC's are operated at  $\sim 40$ - $50$  kV/cm electric fields, efficiencies >95% and timing resolution ( $\sigma$ )  $\sim 1$  ns. The signal readout is simple due to the absence of signal amplification requirements, however, rate capability is limited to  $\sim 100$  Hz/cm<sup>2</sup>. The experiments utilising RPC's operated in the streamer mode are L3 [34], BABAR [35], BELLE [36], muon-arm of ALICE [37], BESIII [38], OPERA [39], ARGO-YBJ [40]. The upcoming Indian Neutrino Observatory (INO) [50] experiment and the DUNE experiment at Fermilab plan to use 2 mm gap Bakelite RPC's operated in the streamer mode.

The Avalanche mode of operation demands sophisticated electronics as the charge generated in the gap is low, giving small signals that require pre-amplification. The rate capability is much higher ( $\sim$ a few kHz/cm<sup>2</sup>) and Multigap RPC's operated in the avalanche mode have excellent timing resolution. As a trigger detector, avalanche mode RPC's are used by the ATLAS [41],

CMS [42] and LHCb [43] experiments as the muon trigger detector. The PHENIX experiment uses a double-gap Bakelite RPC [44] in the avalanche mode as muon trigger. Multigap RPC's for timing purposes are used in the HARP[45], ALICE (TOF)[46], STAR(TOF and MTD)[4], FOPI [48] and HADES [49] experiments. An excellent summary of RPC application at the different experiments worldwide can be found in Ref. [6], including mode of operation, acceptance area, electrode, gap thickness and number of gaps .

### 3.4 Fabrication of 5-gap Glass MRPC modules at VECC for the STAR-MTD

A large part of this thesis work is the development of glass MRPC's for the STAR Muon Telescope Detector upgrade at RHIC. The physics motivation behind the MTD has been thoroughly discussed in previous sections. In this section, we shall discuss about detector geometry and the fabrication and testing of the five-gap MRPC's installed at STAR. After several years of R&D with prototype detectors, starting from the year 2007, the working MRPC module design was finalised in 2011. The three types of MRPC prototypes that have been studied are :

- Type A - Double stack MRPC module with 10 gas gaps. Detector active area is  $87 \text{ cm} \times 17 \text{ cm}$ . 6 double-ended readout pads of width 2.5 cm with a 0.4 cm gap between each pad.
- Type B - Single stack MRPC module with 5 gas gaps. Detector active area is  $87 \text{ cm} \times 52 \text{ cm}$ . 12 double-ended readout pads of width 3.8 cm with a 0.6 cm gap between each pad.
- Type C - Single stack MRPC module with 6 gas gaps. Detector active area and readout strips identical to Type B.

The Type B MRPC prototype was chosen as the final design and the number of gaps and the read-out strip size was chosen after duly considering High Voltage constraints and the requirement of the number of electronics channels. A total of 122, single stack, 5 gap MRPC modules

of dimensions  $91.5 \text{ cm} \times 58 \text{ cm}$  have been installed at mid-rapidity at STAR. A schematic of the MRPC is shown in Fig. 3.10.

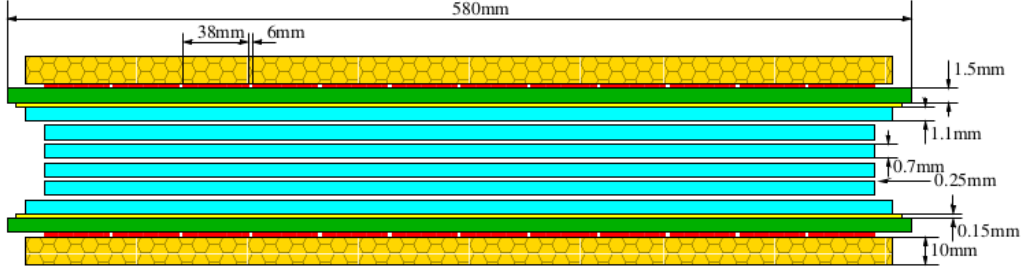


Figure 3.10: A schematic diagram of the Type B MRPC. The different components used for detector fabrication have been highlighted in different colors. Honeycomb boards are in yellow, Read-out strips are in red, Printed Circuit Boards (PCB) are shown in green, the Mylar insulating foil is colored light yellow while the glass plates are sky blue in color. Diagram not to scale. The vertical dimension has been enhanced to get a clear view [51].

The detectors have double-ended differential strip readout, with each strip having a dimension of  $87 \text{ cm} \times 3.8 \text{ cm}$  and 12 such strips on both sides of each detector. The strips are separated by a gap of 6 mm. Two different sets of float glass plates of resistivity  $\sim 10^{13} \Omega\text{cm}$  are used for detector fabrication. The inner glass electrodes are 0.7 mm in thickness, while the outer graphite-coated electrodes for high voltage application are slightly thicker at 1.1 mm. The HV electrode is painted with colloidal graphite and a surface resistivity of  $\sim 5 \text{ M}\Omega/\square$  is maintained to ensure electric field uniformity.

The fabrication procedure of the long MRPC modules is a non-trivial process that follows several rigorous steps, undertaken with great care and caution. The flowchart in Fig. 3.11 summarizes the MTD-MRPC fabrication procedure at VECC followed by brief outlines of the steps and pictures of the fabrication steps.

The glass plates (both inner and outer electrodes) for detector fabrication were sent to VECC by Tsinghua University, Beijing, China, alongwith the nylon monofilament fishing line for defining the gas gaps. This was done to ensure uniformity in the MTD-MRPC modules fabricated at the two Chinese Institutes, USTC and Tsinghua and at VECC. The inner glass plates of  $700 \mu\text{m}$  thickness are cleaned with distilled water and Alcohol (2-propanol) to remove

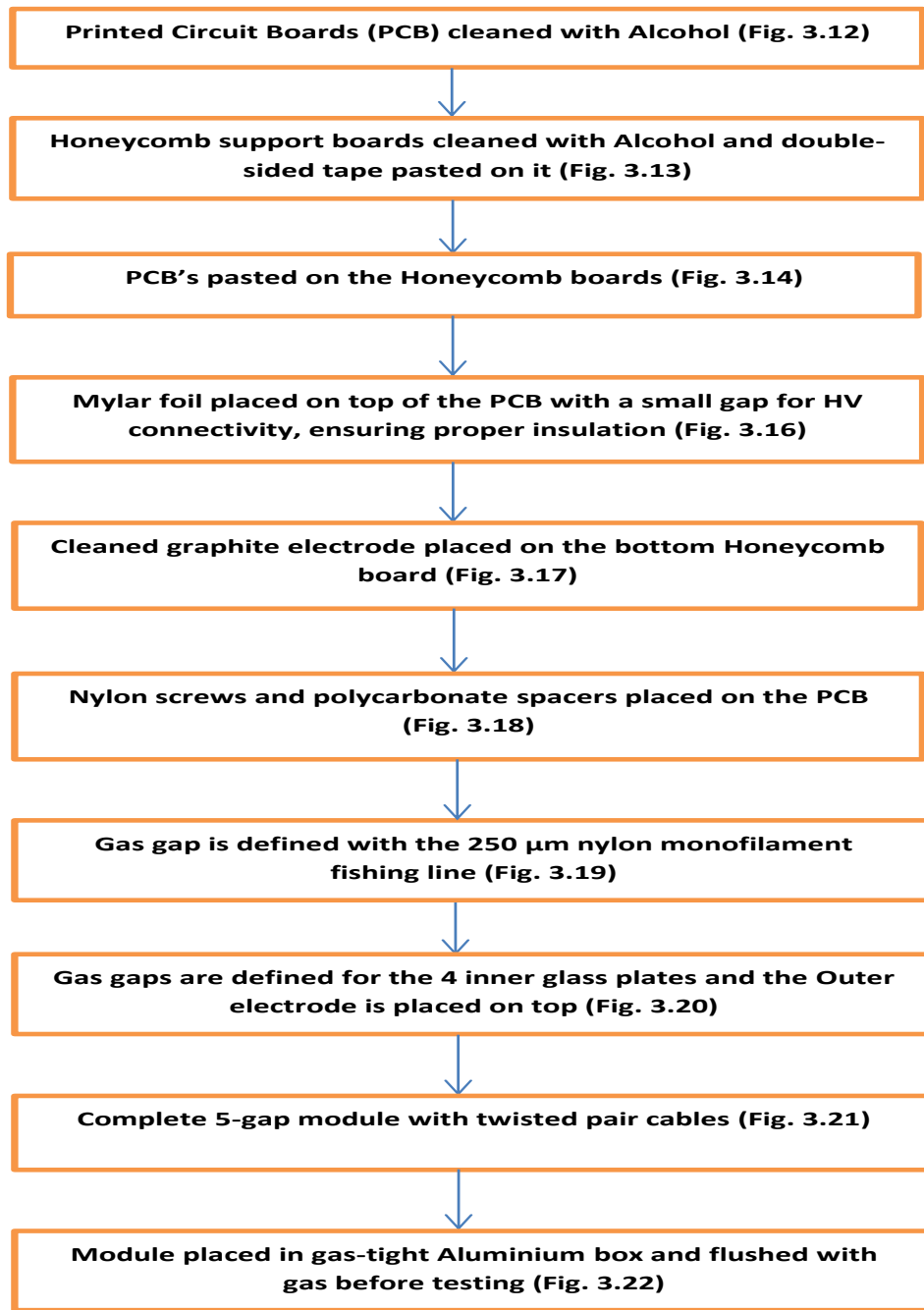


Figure 3.11: A flowchart summarising the fabrication procedure of the MTD-MRPC modules at VECC.



dust from the surfaces. Four such glass plates are thoroughly cleaned for the 5-gap MRPC. The clear side of the two graphite electrodes (1.1 mm thick glass plates) are cleaned in a similar fashion.

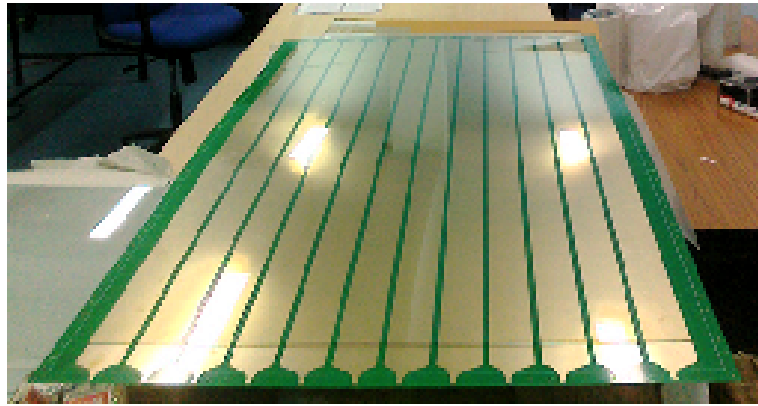


Figure 3.12: Printed Circuit Board (PCB) with metallic (Cu) readout strips.

The top and bottom printed circuit boards (PCB) shown in Fig. 3.12 are then cleaned thoroughly with Alcohol. The same is done for the top and bottom Honeycomb boards that provide support to the glass MRPC's.

After thorough cleaning of the boards, a double-sided tape is pasted on them carefully (Fig. 3.13).

Thereafter, the PCB's, top and bottom, are pasted on top of the taped sides of the corresponding honeycomb boards as shown in Fig. 3.14, with adequate weights to ensure uniform adherence of the PCB's on the boards.

The copper strips on the PCB's are now cleaned and a mylar sheet cut to appropriate dimensions is placed on the PCB. Initially, a small part at the edge of the mylar sheet as illustrated in Fig. 3.15, used to be removed to make space for putting a graphite tape on top of the copper tape placed on the PCB.

Test results revealed that this large gap caused serious problems in the MRPC modules and arcing at the edge of the glass electrodes due to a lack of insulation. The mylar design was modified thereafter and a small rectangular opening on top of the copper strip was made to



Figure 3.13: Putting the double-sided tape on the honeycomb board before attaching the PCB board to it.

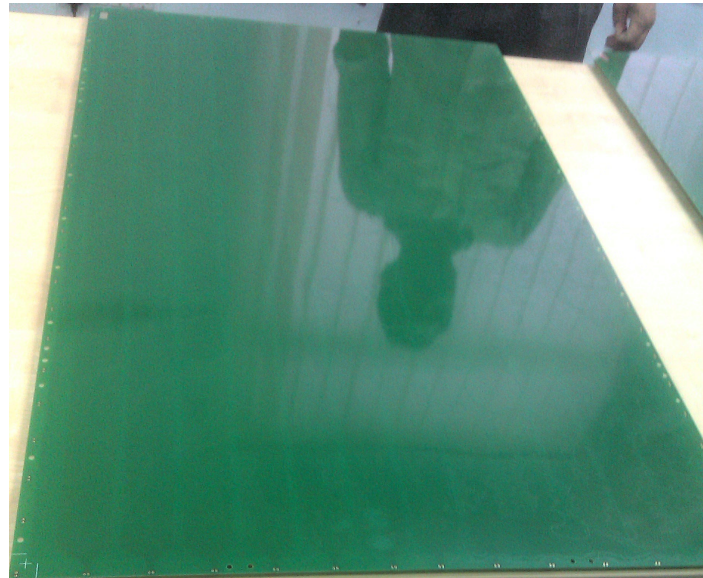


Figure 3.14: PCB pasted on the honeycomb boards with double-sided tape.

account for the graphite tape. This new design has been illustrated in Fig. 3.16.

The graphite-coated electrode is carefully placed on top of the PCB , shown in Fig. 3.17, with the mylar foil placed on top, ensuring proper contact between the electrode and the underlying graphite tape for the uniformity of the applied high voltage. It is then cleaned with an air

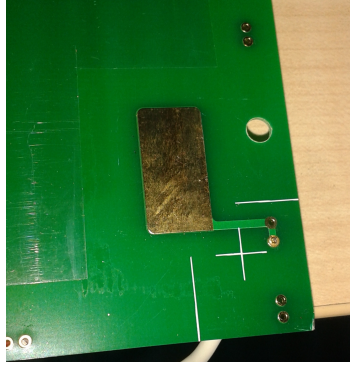


Figure 3.15: Old design with a part of the Mylar foil at the edge completely removed. This led to improper insulation and arcing of the glass electrodes. The process was subsequently discontinued.



Figure 3.16: New Mylar design with just a small gap for graphite tape.

gun to remove dust particles. The PCB is lined with holes on all four sides for the insertion of custom-made nylon screws and polycarbonate side spacers to hold the fishing line in position. The nylon screws and the polycarbonate spacers are placed on the PCB as shown in Fig. 3.18.

With the graphite electrode in position over the honeycomb boards the gas gaps are defined using the 250  $\mu\text{m}$  nylon monofilament fishing line.

A picture of the first gas gap defined on the outermost electrode is shown in Fig. 3.19. The glass surface with the fishing line is duly cleaned with an air gun to remove any unwanted dust particles everytime, before placing new glass plates on top. This process is repeated for the four inner glass plates to define the five 250  $\mu\text{m}$  gas gaps for the five-gap MRPC. During the winding



Figure 3.17: Graphite electrode placed on the bottom honeycomb board.

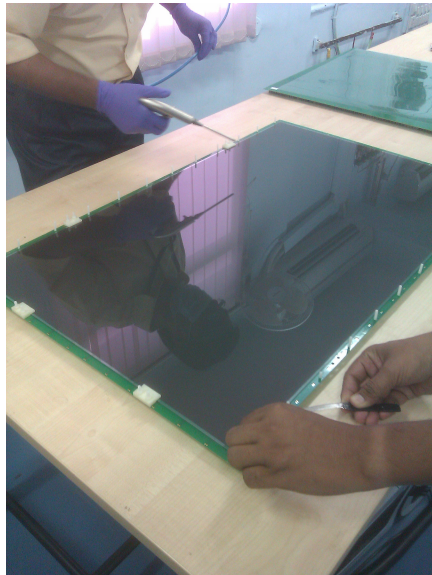


Figure 3.18: Cleaning of the bottom electrode with a spray gun. The nylon screws and spacers are also in position.

process, the fishing line is cleaned with lint-free tissue to remove dust particles from it. Fig. 3.20 shows a close-up view of the 5 MRPC gas gaps, held in place by the nylon screw to which the fishing line are wound.

The final step is to carefully place the other graphite electrode mounted on the honeycomb board with the PCB and the mylar sheet over the top of the stack of glass plates with the fishing



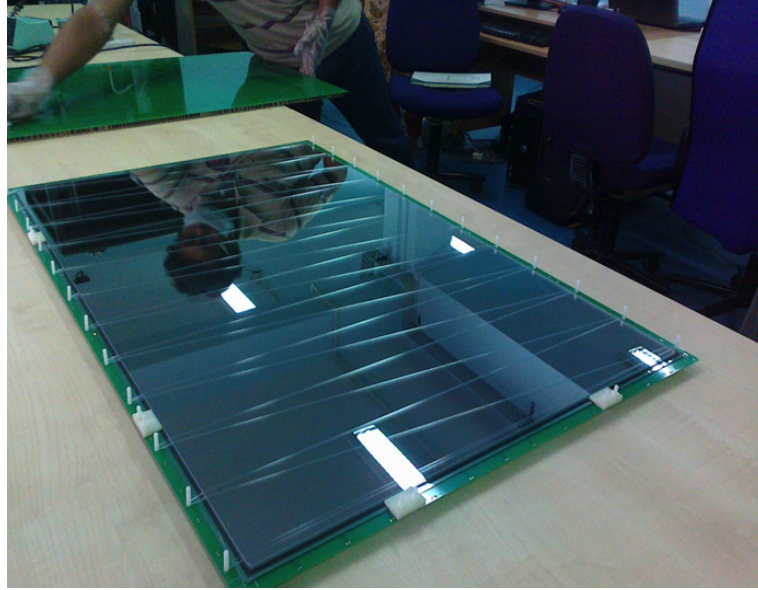


Figure 3.19: 250  $\mu\text{m}$  nylon monofilament fishing line defining one of the gas gaps on a glass plate

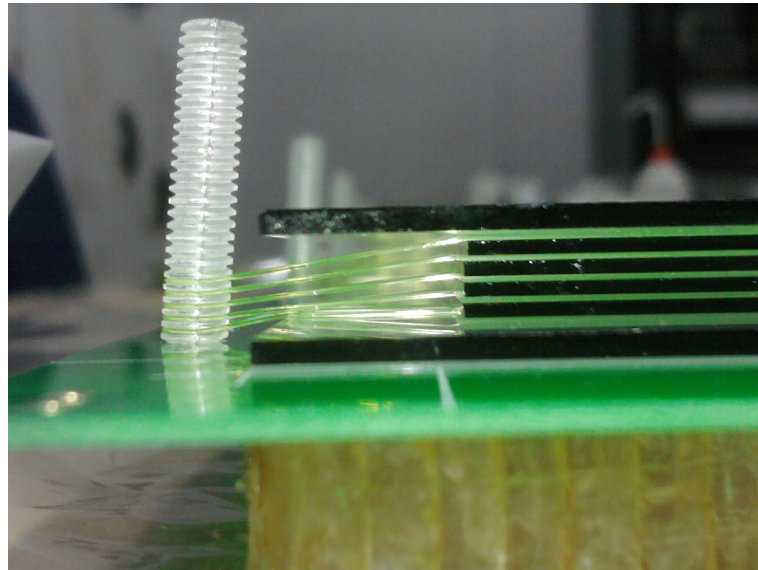


Figure 3.20: A Nylon screw holding the fishing lines in position for the 5 gas gaps. The picture shows all the components in place, from the bottom honeycomb board and PCB and the (outer and inner) glass plates, to the nylon screw and the fishing line.

lines and bolt the screws for compactness. A completed module is shown in Fig 3.21, with 4 ribbon cables connected to the strips for signal readout. The ribbon cables, also called pigtails,

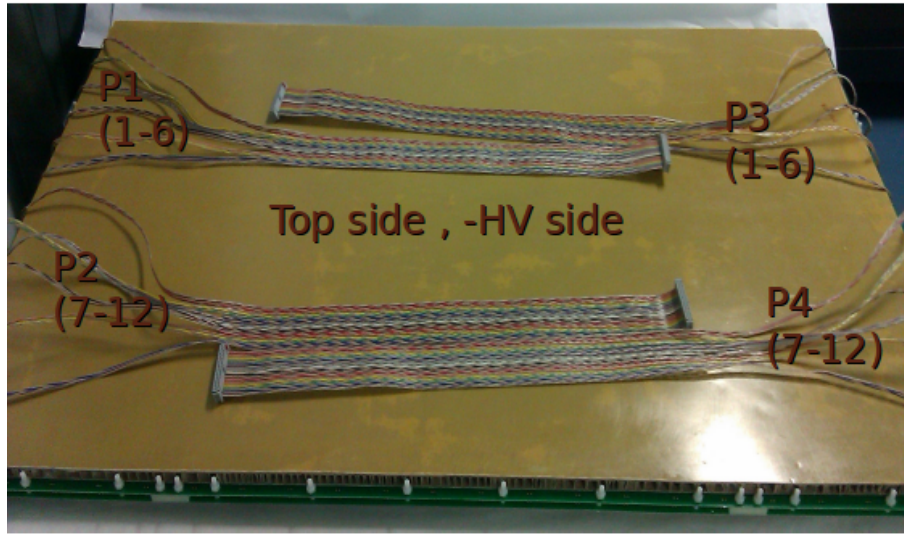


Figure 3.21: A completed module with the twisted pair cables connected.

have been sent to VECC by UT, Austin, USA and have been connected conforming to the norms for the MRPC. The cables P1 and P3 are identical and are meant for strips 1-6, while the other set of identical cables, P2 and P4 connect strips 7-12.

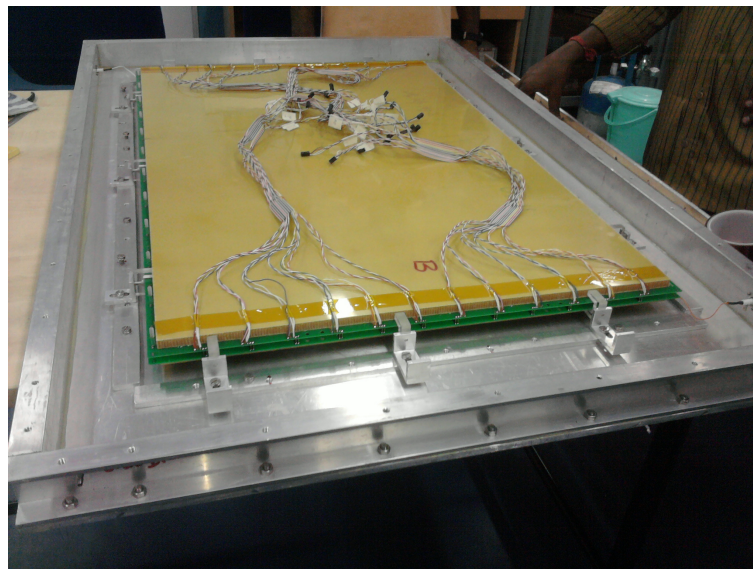


Figure 3.22: The module is placed in the ingeniously built, gas-tight Aluminium box for testing.

The completed module is then placed in a gas-tight Aluminium box for testing as shown in Fig. 3.22. The module is then tested in the Avalanche mode with a gas-mixture of Freon (R134A) and isobutane ( $i\text{-C}_4\text{H}_{10}$ ) in a volume ratio of 95 : 5 and a picture of the gas mixing and distribution system has been shown in Fig. 3.23. The High Voltage was applied with a CAEN N1470 NIM HV power supply. The detector was normally ramped up at  $\sim 8$  V/s. A summary of the components including their dimensions used during the fabrication of individual MRPC modules is shown in Fig. 3.24.



Figure 3.23: Gas mixing and distribution system.

Material	Dimension (mm)	Tolerance (mm)	Quantity
Outer glass	890×559×1.1	±0.5, ±0.5, ±0.02	2
Inner glass	870×549×0.7	±0.5, ±0.5, ±0.02	4
Graphite electrode	888×557×0.1	-0.5	2
Mylar film	895×564×0.15	±0.1	2
Honeycomb board	890×559×10	±1.0, ±1.0	2
PCB	915×580×0.9 12strips, 38×870/strip	±0.5	2
Fishing Line	Diameter 0.25	±0.005	
Nylon screw			24
Side spacer(poly carbonate)			8
HV lead	60cm	±1	2
Signal lead	60cm	±1	4

Figure 3.24: Summarising the components required for the fabrication of a MTD-MRPC module including their dimensions and respective quantities.



### 3.5 Test results of the MTD-MRPC modules at VECC with cosmic rays

After the completion of a module, it is kept in the Aluminum gas-tight box and flushed with gas for the next 3 days (72 hours), which ensures  $\sim 2$  volume changes of gas in the detector at the flow rate of 20 SCCM (Standard Cubic Centimetre per Minute). After that, the high voltage was applied to the detector. The detector is initially seasoned by ramping the voltage manually with the CAEN N471A NIM HV power supply. It is then ramped up to the operating voltage of  $\pm 6300$  Volts at the rate of 8 V/s with the CAEN N1470. The detector V-I characteristic is measured to determine the performance of the detector and is shown in Fig. 3.25.

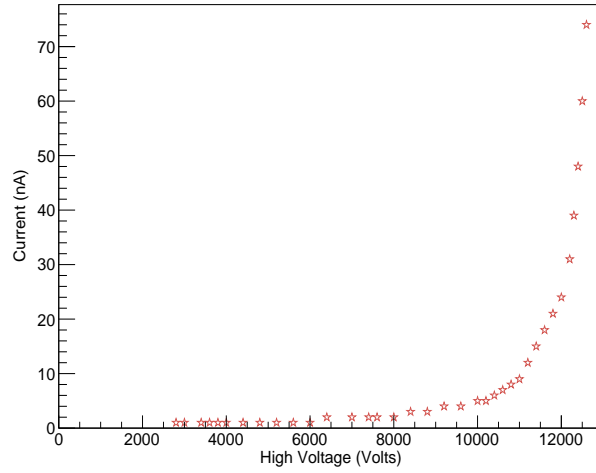


Figure 3.25: V-I characteristic of VECC MTD-MRPC module #9 as a function of high voltage.

The V-I characteristic curve clearly has two distinct slopes, which is an inherent feature of the RPC gas gap. The RPC gas gap can be suitably described by an equivalent circuit diagram shown in Fig. 3.26. It can be represented as a combination of the spacer resistance and the gap resistance, acting in parallel. While the behaviour of the spacer is Ohmic, the gas gap behaves like a Zener diode. The electric field at lower operating voltages is insufficient for avalanche development. Therefore, the gas gap behaves like an insulator and offers a path of infinite

resistance to the flow of current. As explained by Eq.s 3.10-3.12, the slope of the V-I curve in this regime is determined by the resistance of the spacer. At higher voltages, the breakdown of the gas inside the detector changes the scenario. The development of Avalanches means the gas gap starts behaving like a conductor and offers a zero resistance path to the flow of current. The slope of the V-I curve in this regime of operation is determined by the resistance of the glass plates as shown in Eq.s 3.13-3.14.

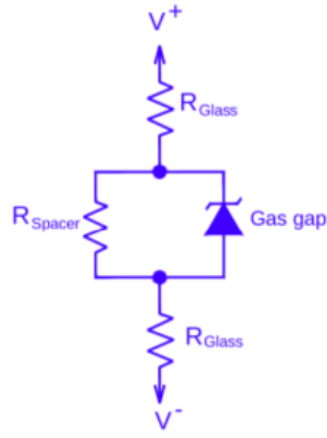


Figure 3.26: Electrical equivalent circuit diagram of a glass RPC gas gap [6]

At low operating voltages :

$$R_{gap} \approx \infty \quad (3.10)$$

$$R_{spacer} \gg R_{glass} \quad (3.11)$$

$$\frac{dV}{dI} = R_{spacer} \quad (3.12)$$

while at higher operating voltages:

$$R_{gasgap} \approx 0 \quad (3.13)$$

$$\frac{dV}{dI} = R_{glass} \quad (3.14)$$

A schematic of the cosmic ray test-setup is shown in Fig. 3.27. The 2 paddle scintillators S1 and S2 are of dimensions  $20 \text{ cm} \times 8.5 \text{ cm}$ , while the narrow paddle, referred as the finger scintillator FS is  $5 \text{ cm} \times 1.5 \text{ cm}$ . The analog scintillator and detector pulses are sent to the CAEN N841 Leading Edge Discriminator. The master trigger is determined by the 3-fold coincidence of the scintillators.

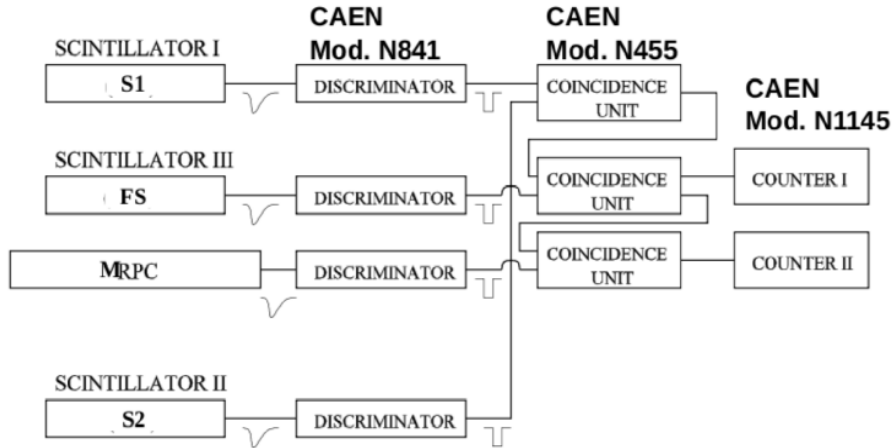


Figure 3.27: A schematic diagram showing the cosmic ray trigger scheme for the MRPC test.

The coincidence of the MRPC logic signal with the 3-fold is defined as the 4-fold. The CAEN N455 module is the coincidence unit used for the tests. The efficiency of the detector is defined as the ratio of the 4-fold count to the 3-fold count for a fixed time. The 4-fold and 3-fold numbers are counted using the CAEN N1145 counter module. The efficiency of the detector as

a function of the applied high voltage is shown in Fig. 3.28. An efficiency of 90% is obtained at the detector operating voltage of  $\pm 6300$  Volts. The onset of the plateau region as seen from the efficiency plot (Fig. 3.28) ( $\sim 12$  kV) that coincides with the start of the breakdown region as seen from the V-I characteristic plot (Fig. 3.25).

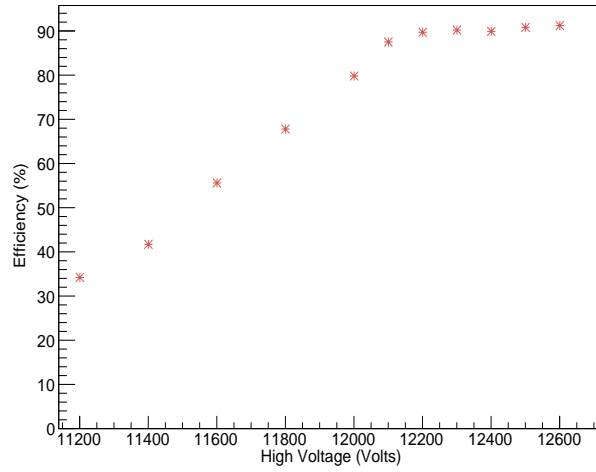


Figure 3.28: Efficiency of VECC MTD-MRPC module #9 as a function of high voltage.

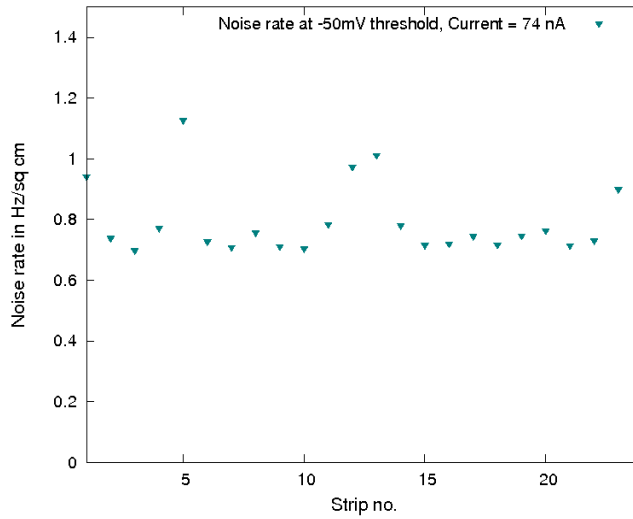


Figure 3.29: Strip-by-strip noise rate variation of the VECC MTD-MRPC module #9 at the operating voltage of  $\pm 6300$  Volts.

The strip-by-strip variation of the detector noise rate(normalized by strip area) as shown in Fig. 3.29 has been measured at the detector operating voltage of  $\pm 6300$  Volts. The detector read-out being double sided, there are 24 readings for the 12 readout strips. As an example, 1 and 13 are opposite sides of the same strip and so on. The slightly higher noise rate for the strips at the edge is expected due to the electric field deformation at the edges. Apart from one end of strip 5 which is noisy, the rest of the strips show consistent noise rates  $\sim 0.8$  Hz/cm<sup>2</sup>. The test results shown here are for the VECC MTD-MRPC module #9. The test results for the other 9 MRPC modules fabricated at VECC were similar. The VECC MRPC module #9 was also tested at University of Texas at Austin, USA and the test results have been shown in Fig. 3.30 and Fig. 3.31. A strip-by-strip noise rate measurement at UT Austin for module #9 is shown in Fig. 3.30 and results obtained are similar to the test results at VECC. The strips at the edges of the detector are noisy due to the electric field deformation. The pick-up strips are readout at both ends and High Z and Low Z indicate the positioning along the z axis. Fig. 3.31 shows a correlation plot of the noise measurements at the two ends of each strip. This test is performed to investigate the proper functioning of the readout channels without any damage. The 12 double-ended strips are numbered 0-11 on one side and 12-23 on the other side by convention. In the ideal case, the noise rate peaks obtained from the two ends of each strip should be mirror images of each other. Fig. 3.31 reveals identical noise rate measurements from opposite ends of each strip and that all readout strips function properly.

### 3.6 Cosmic ray Test results of the MTD-MRPC modules at STAR

A cosmic-ray event in STAR [51] is schematically depicted in Fig. 3.32 and passes through the MTD, BEMC, TOF and TPC detectors in the order of sequence. During the passage of a cosmic ray muon, the time recorded by an MTD-MRPC is called tMTD, while the times noted by two TOF MRPC's on either side of the interaction point are called tTOF1 and tTOF2 respectively.

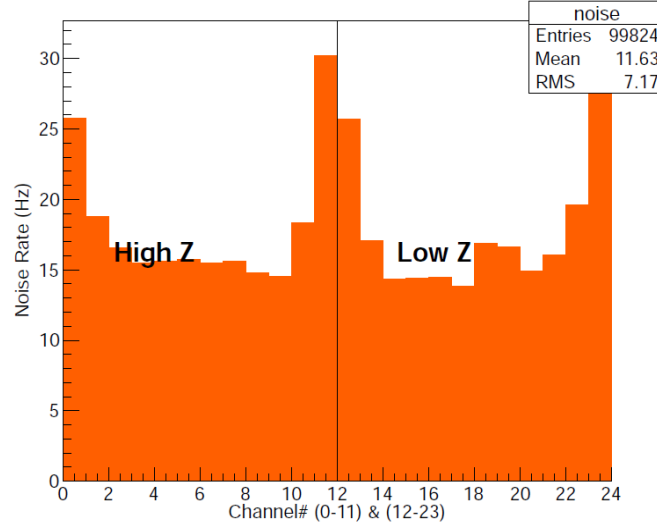


Figure 3.30: Strip-by-strip noise rate measurement of the VECC MTD-MRPC module #9 at the operating voltage of  $\pm 6300$  Volts at UT Austin.

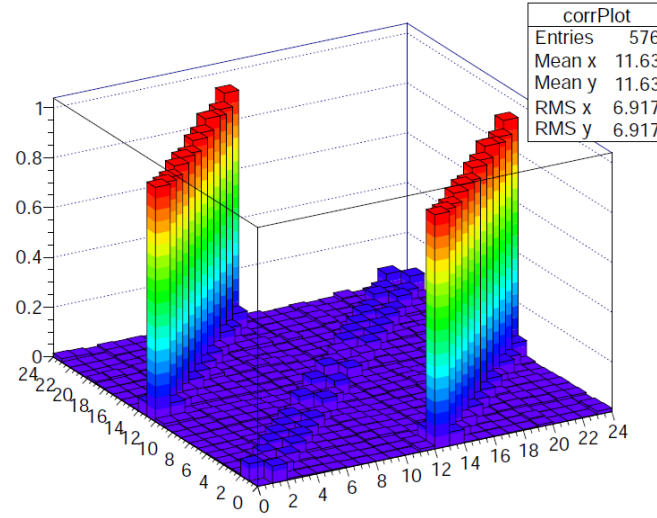


Figure 3.31: A correlation plot showing the noise correlation of the VECC MTD-MRPC module #9 at the operating voltage of  $\pm 6300$  Volts at UT Austin.

The time-of-flight between the two TOF detectors can be calculated using the path length of the cosmic ray and the momentum  $p$  measured by the TPC and is referred as  $t_{\text{TPC}}$ . Similarly, the time-of-flight through the magnet backlegs between the MTD and the first TOF detector can also be calculated using the helical path length traversed by the cosmic muon of momentum

p. This time is referred as tSteel.

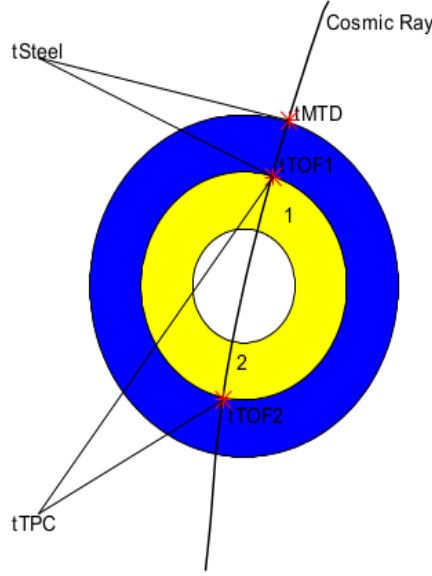


Figure 3.32: Schematic representation of a cosmic ray event at STAR [51]

The spatial resolution of the MTD-MRPC detectors along the  $z$  direction (direction along the strips) and the azimuthal direction (direction perpendicular to the strips) are measured by extrapolating the reconstructed tracks from the TPC to the MTD. The hit position at the MTD in the  $Z$  direction is calculated as the difference between the leading times of the signal from the two ends of the readout strip that is fired. Whereas, the middle point of the strip that has the largest signal gives the  $\phi$  position [51]. The  $\Delta Z$  and  $\Delta\phi$  distributions as shown in Fig. 3.33 are obtained as the difference between the extrapolated TPC track hit position and the measured MTD hit position in the  $Z$  and  $\phi$  directions respectively. The standard deviation of the Gaussian fit to the  $\Delta Z$  and  $\Delta\phi$  distributions gives a detector spatial resolution of 2.6 cm and 0.006 radians respectively [51].

The time resolution of the detector is measured with tracks matching the selection criteria of  $\Delta Z < 6$  cm and  $\Delta\phi < 0.2$  radian. The timing resolution of the MTD system is obtained from  $t_{\text{MTD}}$  after subtracting the start time contribution of the TOF detectors and the time-of-flight through the steel backlegs. The resultant expression  $\Delta T = (t_{\text{TOF2}} - t_{\text{TPC}} + t_{\text{TOF1}})/2 - t_{\text{MTD}}$

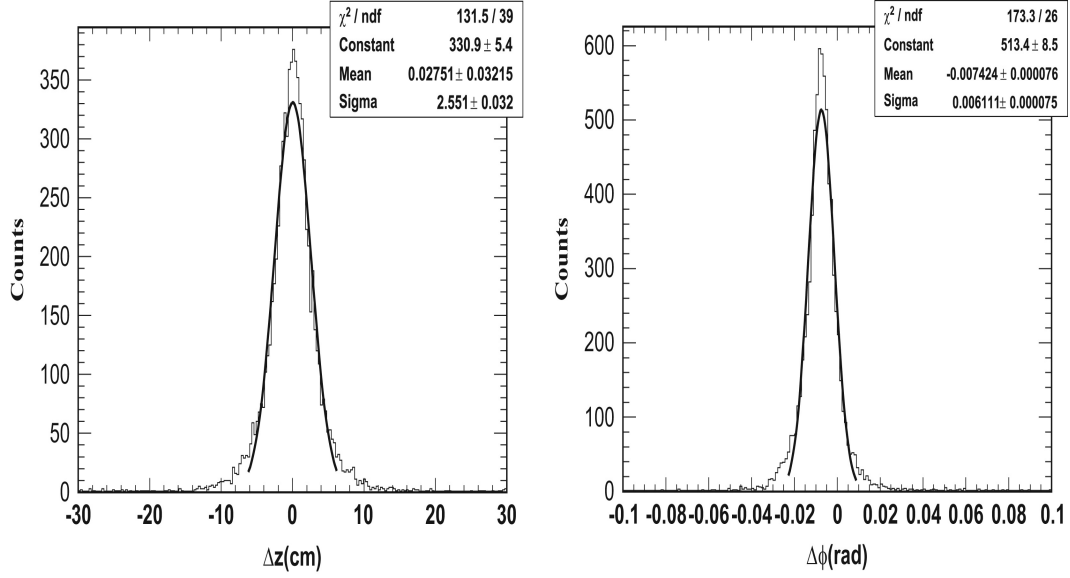


Figure 3.33: The  $\Delta Z$  distribution shown in the left panel and the  $\Delta \phi$  distribution shown in the right panel. The standard deviation of the Gaussian fits (solid curves) gives the detector spatial resolution [51].

- tSteel, is plotted for each individual strip and the standard deviation of the Gaussian fit to this distribution gives the detector time resolution. The top frame of Fig. 3.34 shows the standard deviations of the  $\Delta T$  distribution of each strip after correcting for slewing and offsets [51]. The bottom frame of Fig. 3.34 shows the overall timing resolution of the detector by combining the values of each strip. The standard deviation of the Gaussian fit to this distribution, 104 ps, gives the timing resolution of the detector [51].

Details of the cosmic ray test results of the MTD-MRPC modules can be found in [51]. The test results are found to conform with the expected values [52] for the MTD-MRPC's and make this detector suitable for the physics requirements [53] that it aims to address.



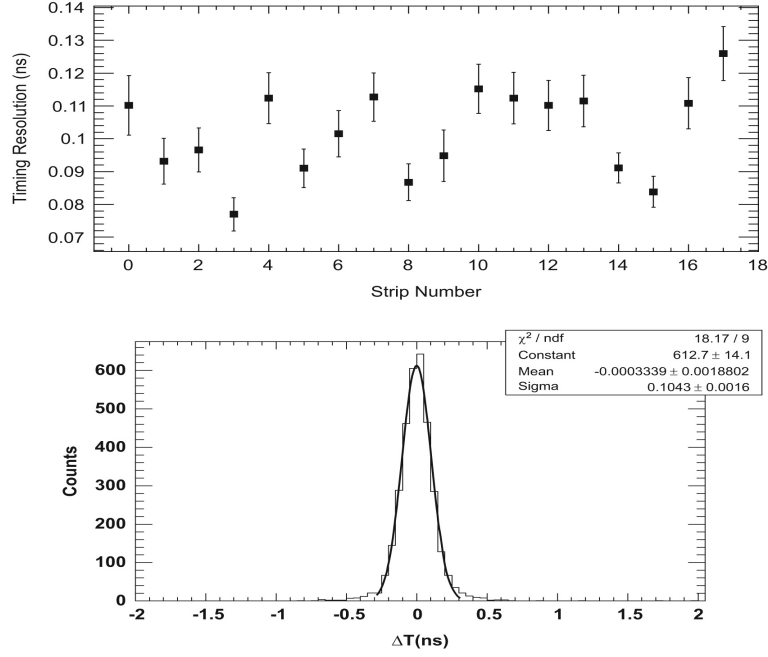


Figure 3.34: Timing Resolution

### 3.7 Detection of 511 keV photons with MRPC's as a proof-of-principle for TOF-PET

Among the many uses of technologies being developed for experiments on high energy physics, one of the principal spin-off benefits is the use of newer, advanced detector technologies for Medical Imaging purposes. Positron Emission Tomography (PET) is one of the many avenues that are being explored to find suitable improvements to existing detection techniques. RPC's with excellent timing resolution, similar to the STAR-MTD MRPC's, are being investigated as potential candidates for PET imaging [54][55]. A preliminary effort using small-sized MRPC prototypes fabricated using the same raw materials and identical detector technology as the MTD MRPC's, has been undertaken to test the proof-of-principle of PET imaging. This has been explained in detail in the next few sections, including a discussion on the benefits of Time-of-Flight PET (TOF-PET) imaging.

### 3.7.1 Introduction

Positron Emission Tomography is a biomedical imaging technique in which a radionuclide labelled with a positron emitter ( $^{11}\text{C}$ ,  $^{13}\text{N}$ ,  $^{18}\text{F}$  or  $^{15}\text{O}$ ) is administered into the object under investigation. The emitted positrons have an extremely small range ( $\sim 1\text{-}2$  mm in human tissue) and annihilate with an electron to emit two back-to-back (momentum conservation), 511 keV photons. A coincidence event is defined when a pair of photons considered from the same annihilation event are detected on opposite sides of the object being studied within a narrow time window, called the coincidence time window. The coincident detection of the two almost co-linear, 511 keV photons, is the basis of PET. It establishes the occurrence of the positron-electron annihilation event along the line joining the relevant detectors where the events were registered. This line is referred to as the Line-Of-Response, LOR. A collection of such LOR events, recorded for all possible angles, enables the reconstruction of the activity distribution of the positron emitter in the tissues. 3D tomographic images are reconstructed via filtered back-projection or by iterative reconstruction techniques [56]. There are however, several limitations as far as PET imaging and the precision of the image reconstruction is considered. Multiple factors degrade the actual achievable resolution of a PET system. The most important factors [7][57], as highlighted in Fig. 3.35 are

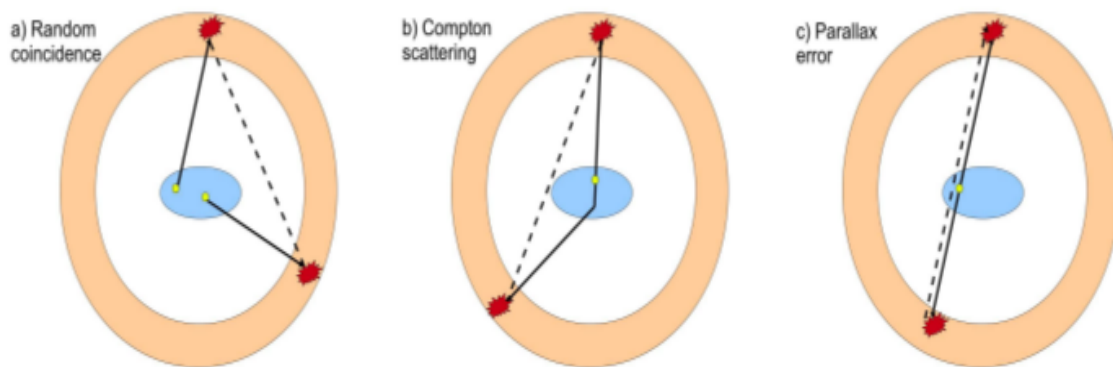


Figure 3.35: Factors degrading PET resolution a) Random coincidences, b) Compton scattering of the photons c) Effect of Parallax error [57].

- **Random Coincidences :** The detection of photons from different annihilation events result in random coincidences. It is a function of the detector coincidence time window for two real photons emitted from an annihilation event. Improvements in the detector time resolution help remove random coincidences.
- **Compton scattering :** The 511 keV photons emitted from a positron-electron annihilation event are scattered within the object being studied, during the course of their travel before detection. Compton scattering decreases the actual photon energy from 511 keV and also changes the direction of the photons. As a consequence, when a scattered event is detected, the recorded LOR has no correlation with the actual annihilation event. Such discrepancies in the data causes a degradation in the image reconstruction resolution, where the final reconstructed image is inaccurate and lacks in contrast. The sensitivity of the detection system towards photons having energy less than 511 keV plays a major role in this. Attenuation of one or both photons results in the complete loss of the actual event, causing a loss in statistics.
- **Parallax Error :** In crystal-based PET systems, the 511 keV photon is detected after it travels a certain distance before full energy deposition and is determined by the stopping power of the crystal. This actual location can only be truly measured if the depth of interaction (DOI) for the detector is known. The projection of this point on the surface of the detector is taken as the photon detection point and used for constructing the LOR. This causes a large parallax error if the variation between the real position and the projected point is appreciable and images reconstructed are blurred. Photons entering the detector obliquely are especially affected. Detection systems with excellent position resolution that are unaffected by parallax effects improve the resolution of the reconstructed image.

### 3.7.2 Advantages of Time-of-Flight in PET

The use of Time-of-Flight information in PET systems dates back to the 1980's and a detailed summary can be found in [58][59]. Although the systems (e.g. Cesium Fluoride, CsF and Barium Fluoride, BaF<sub>2</sub> crystals) had excellent count rate, they had poor spatial resolution and could not match the sensitivity of the existing non-TOF systems (Bismuth Germanate BGO crystals). Naturally, interest in TOF-PET systems gradually declined till recently, when a resurgence in TOF-PET imaging due to the progress in scintillator technology has brought them back into use [56]. The advent of scintillating crystals with good time resolution (Lutetium Oxyorthosilicate, LSO and , Lutetium-Yttrium Oxyorthosilicate, LYSO crystals) alongwith fast, reliable PMT's and advancements in list-mode reconstruction algorithms, make TOF usage the realistic choice. In a detection system using Time-of-Flight information, precision measurement of the arrival times of the coincident photons is possible and the difference in times helps to localize the annihilation event on the LOR [56]. Apart from reducing random coincidences, TOF information enhances the signal-to-noise ratio of the reconstructed image by minimizing noise propagation along the LOR [56] and reduces data acquisition time and dosage [57]. The annihilation position along the LOR can be established with an FWHM accuracy  $\Delta L$  [54] related to the FWHM accuracy in time  $\Delta t$  as shown below

$$\Delta L[mm] = c \frac{\Delta t[ps]}{2} \quad (3.15)$$

$$\Delta L[mm] = c \frac{2.36\sqrt{2}\sigma_t[ps]}{2} \quad (3.16)$$

$\sigma_t$  is the rms timing resolution of the detecting element.

$$\Delta L[mm] \approx \frac{\sigma_t[ps]}{2} \quad (3.17)$$

According to Eq. 3.17, a detector time resolution of 100 ps (rms) localizes the annihilation point to an FWHM accuracy of  $\approx 50$  mm. Although this value is well beyond image granularity ( $\sim$  a few mm) requirements [54] for PET systems, it certainly helps in terms of the image reconstruction process. A schematic diagram shown in Fig. 3.36 highlights the advantage of using TOF information in PET imaging.

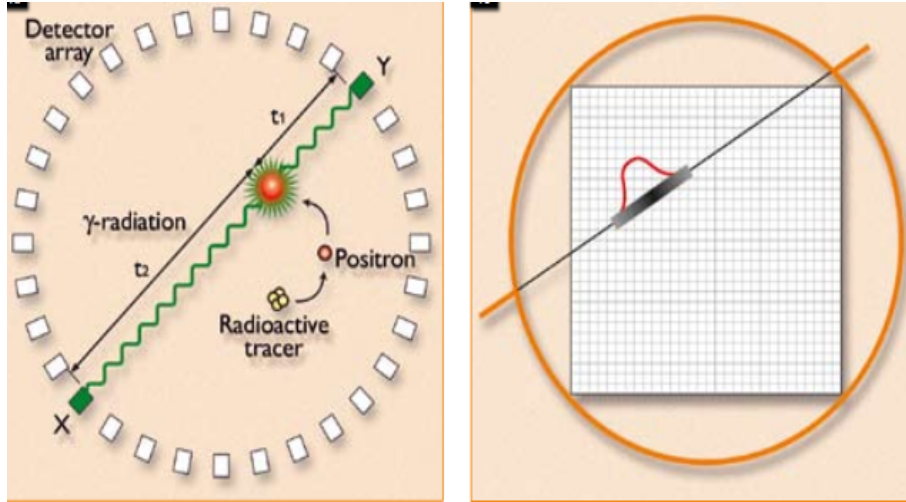


Figure 3.36: a) The positron emitted by the administered radionuclide emits two coincident back-to-back 511 keV gamma rays upon annihilation with an electron. The arrival time difference of the photons ( $t_2 - t_1$ ) helps localize the annihilation event along the line of response (LOR) joining the two detectors X and Y, b) Event reconstruction using TOF information is done within a reduced back-projected region ( $\Delta L$ ) of the LOR determined by the system time resolution [56].

Utilizing TOF information on an object of diameter  $L$  being investigated, an enhancement in sensitivity of  $\sim L/\Delta L$  is achieved, thus reducing the event statistics requirement for the reproduction of images [60]. In non-TOF systems, larger objects suffer from increased attenuation that causes loss of real events and an enhancement in Compton scattered events that lead to poor image quality. TOF-PET has the ability to significantly improve image quality for larger

objects, at par with smaller objects, by accumulating higher statistics within acceptable scan times [56]. The importance of detector time resolution ( $\sigma$ ) is paramount in case of TOF-PET systems. As shown in Eq. 3.17, the better the time resolution of the detector ( $\sigma_t$ ), the smaller the extent of the back-projected LOR region for image reconstruction, hence better the image quality. The other usefulness of excellent time resolution is in minimizing the coincidence time window ( $4\sigma_t$ ) [7]. A lower time window clearly reduces the number of random coincidence events. Therefore, detection systems with excellent time resolution are extremely essential for PET imaging.

### 3.7.3 Advantages of RPC's for use in PET

As previously discussed, RPC'S are gaseous detectors being used worldwide in high energy physics, nuclear physics and neutrino experiments for charged particle detection and are known for their excellent position and timing resolution. The MRPC [28] is a variant of the RPC, conceived in the year 1996, with smaller gas gaps and a much improved timing resolution. Efforts to use the RPC as the detection system in TOF-PET can be found avidly in literature [57][61][62][63]. The potential of RPC's as TOF-PET detection systems can be highlighted through the following :

- Detectors have naturally layered structure suited to photon conversion and are based on the converter-plate principle [64].
- Fabrication of an MRPC is simple, inexpensive and economic construction of large-sized detectors is quite feasible. The Field-Of-View attainable with RPC's [65] comes at a much lower cost compared to existing crystal based systems [57][63]. A larger FOV reduces scan times and dosage.
- Excellent timing resolution ( $\sigma$ ) values have been published for MRPC's ( $\sim 20$  ps for charged particles [66] and  $\sim 90$  ps for single photons [54]).

- Excellent Position resolution values reported for RPC's with a resolution upto  $\sim$ sub-millimeter achievable [62].
- Parallax errors are absent for detection with RPC's.
- RPC's are unaffected by magnetic fields, hence they are compatible with Magnetic Resonance Imaging (MRI).
- The efficiency of gamma detection for RPC's increases as a function of gamma energy as it increases from 200 keV to 500 keV. To the contrary, in case of scintillators, the efficiency goes down beyond gamma energy of 100 keV [63]. Therefore, Compton scattered photons of energies less than 511 keV are naturally suppressed for RPC's.

To sum up, there is a stark contrast between the existing scintillator crystal-based TOF-PET imaging and the proposed MRPC-based TOF-PET imaging. However advantageous MRPC technology might seem, it has obvious limitations, especially for gamma detection as discussed in the next section. Use of MRPC's for TOF-PET imaging seems to be the practical choice for the future and a better alternative to the existing expensive scintillator-based technology. Extensive R&D on the topic is being carried out worldwide by several groups.

### 3.7.4 Limitations of RPC-PET

The critical factor that determines the sensitivity of the gamma detection system for TOF-PET is the quantum efficiency of the detector. The quantum efficiency for RPC's is defined as the number of 511 keV  $\gamma$ 's detected to the original number of  $\gamma$ 's incident on the detector. RPC's being charged particle detectors their photon detection efficiency [54][67] is much lower in comparison to scintillating crystals [63]. The main concern with RPC's is thus the maximization of the gamma detection efficiency which can be improved by using MRPC's and optimising the number of glass plates to improve gamma conversion into electrons and their subsequent detection. Another parameter is the optimization of the electrode thickness as the photons primarily interact with the detector electrode material via the Compton effect.

### 3.7.5 Fabrication and testing of the six-gap MRPC prototype

Despite the challenges of gamma detection with MRPC's mainly in terms of low detection efficiency, their simple and economic construction paves the way for stacking large number of MRPC detectors to increase gamma conversion. An increase in detection efficiency, along with their excellent timing resolution and position resolution can suitably make MRPC's an alternative to the currently used highly expensive scintillator-based systems for PET. The preliminary gamma detection efficiency results of a six-gap MRPC prototype operated in avalanche mode, using a  $^{22}\text{Na}$  source as the  $\beta^+$  emitter has been discussed here. The MRPC prototype [68] has dimensions  $16\text{ cm} \times 10\text{ cm}$ , is built with seven float glass plates, each of thickness  $600\text{ }\mu\text{m}$ , obtained from GSI, Germany. The gas gap between the plates is defined by  $200\text{ }\mu\text{m}$  polycarbonate buttons. The prototype is operated in the avalanche mode with a gas mixture of eco-friendly Freon (R-134A) and Iso-butane, in the ratio 95 : 5. The  $^{22}\text{Na}$  source is placed between the MRPC prototype and a plastic scintillator of dimensions  $5\text{ cm} \times 1.2\text{ cm}$  as shown in Fig. 3.37.

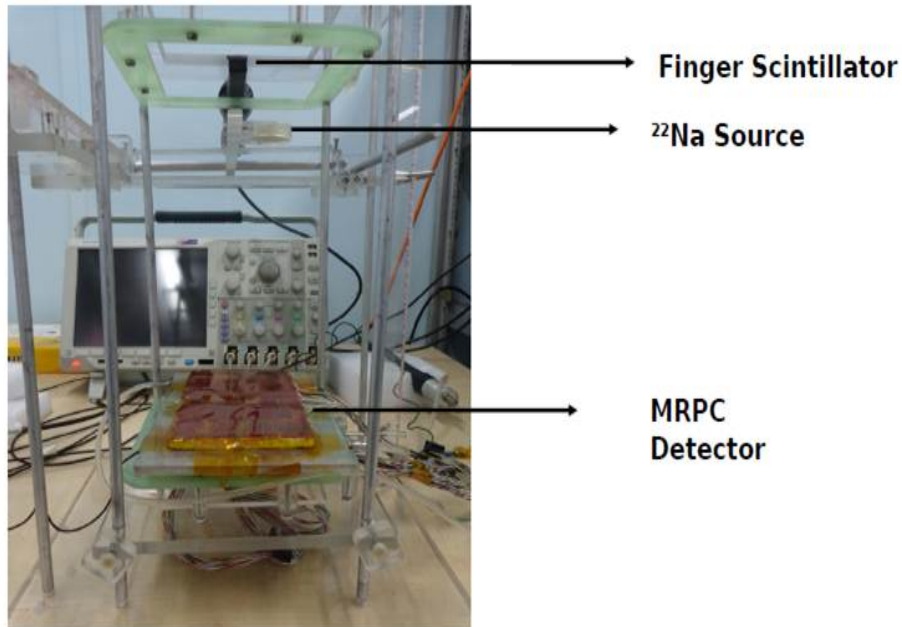


Figure 3.37: Experimental Set-up for testing the prototype MRPC with the  $^{22}\text{Na}$  source [69][70].



### 3.7.6 Experimental Results with the 6-gap MRPC prototype

The positrons emitted by the source travel a very short path length ( $\sim 1\text{-}2$  mm in human tissue [7]) before annihilating with electrons producing two almost anti-parallel 511 keV photons. The test results with the 6-gap MRPC and the plastic scintillator are performed in two different configurations, with the  $^{22}\text{Na}$  source and without the  $^{22}\text{Na}$  source placed between them. The tests without the source is referred as the non-source configuration and is performed to remove the background arising from cosmic muons. Coincidence count rate between the signals obtained from the MRPC strips and the scintillator is measured with and without the source. With the increase of the applied high voltage, the coincidence count rate increases. The coincidence count rate as a function of the applied high voltage is shown in Fig. 3.38 and it clearly establishes the effect of the source.

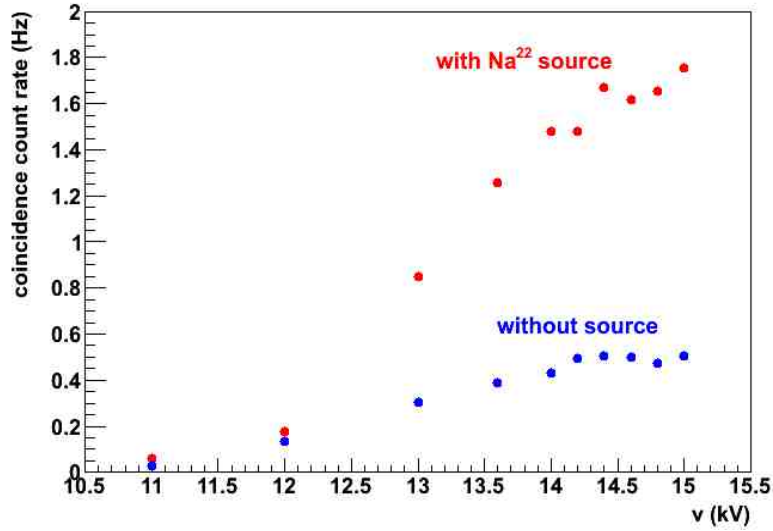


Figure 3.38: The coincidence count rate as a function of the high voltage [69][70].

In the presence of the  $^{22}\text{Na}$  source, the ratio of the two fold coincidence count rate between the MRPC signal and scintillator signal to the number of photons counted by the scintillator (after

subtracting the background contribution due to cosmic muons from the non-source configuration) is defined as the photon-pair detection efficiency. The variation of gamma detection efficiency as a function of the high voltage is shown in Fig. 3.39. The efficiency increases with that of the high voltage and tends to saturate at higher voltages. A photon-pair detection efficiency of 0.9% is obtained at a high voltage of 15 kV after correcting for geometrical acceptance and cosmic ray effect measured in non-source configuration [70][69].

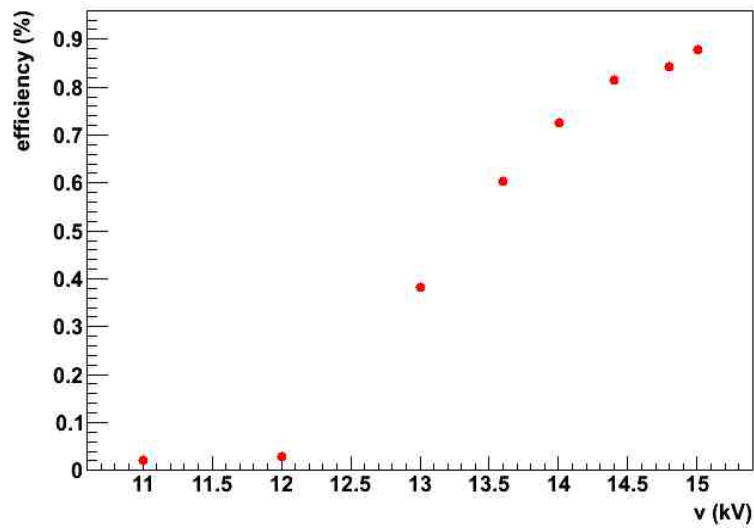


Figure 3.39: The pair detection efficiency as a function of the high voltage [69][70].

In an effort to locate the  $^{22}\text{Na}$  source position, the distance between the scintillator and the MRPC is fixed at 44.5 cm and the time difference between the signals from the scintillator and the MRPC is measured by varying the source position. A simple mathematical calculation assuming a photon velocity of 30 cm/ns gives the expected time difference between the signals. Experimentally, the time differences at the 4 different source positions are obtained by taking the mean ( $\mu$ ) of the Gaussian fit to the time distribution acquired with the start signal from the scintillator and the stop signal from the MRPC. The large error bars are the standard deviation ( $\sigma$ ) values from the Gaussian fit to the time distribution. The calculated and measured time difference as a function of source distance (source distance is measured from the MRPC

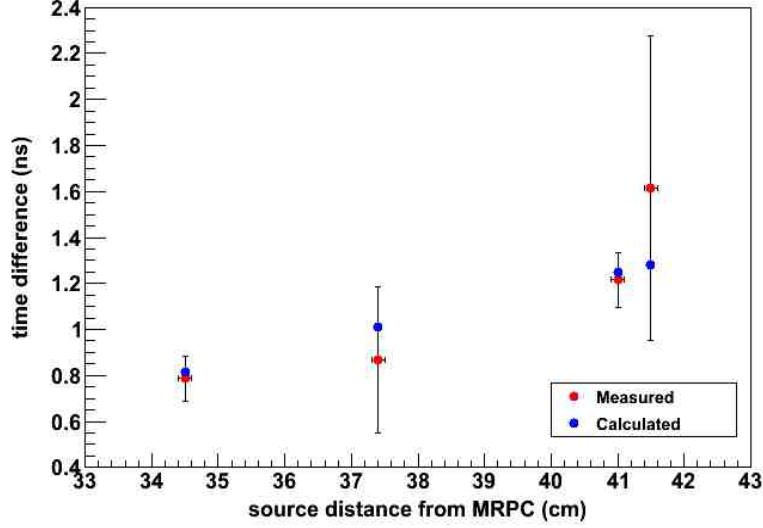


Figure 3.40: Calculated and measured time difference as a function of source distance [69][70].

prototype) is shown in Fig. 3.40 [69][70]. Given the large error bars, the experimentally measured time difference values follow the trend of the calculated time difference values using a 30 cm/ns photon velocity.

### 3.7.7 Fabrication and testing of the two-MRPC coincidence system

Two identical 5-gap MRPC prototypes of dimensions 18 cm  $\times$  18 cm have been built and Fig. 3.41 shows the construction of one such prototype. The prototypes have been built with 0.7 mm glass plates used for the MTD-MRPC modules cut to prototype dimensions and the same nylon monofilament fishing line of thickness 250  $\mu$ m has been used to define the gas gaps. The only difference from STAR geometry is that the outer electrodes are also of the same dimension as the inner electrodes. The electrodes were spray-painted using a semi-conducting graphite paint manufactured by Kansai Nerolac, India in a 1:1 ratio by volume with a special dry thinner from the same company. The obtained surface resistivity for the electrodes is  $\sim 0.7$ - $0.8$  M $\Omega/\square$ . A frame made of Perspex with an “O”-ring on top is used as the gas-tight box for the assembly of the glass plates. The fishing lines are wound on nylon screws inserted into the frame through

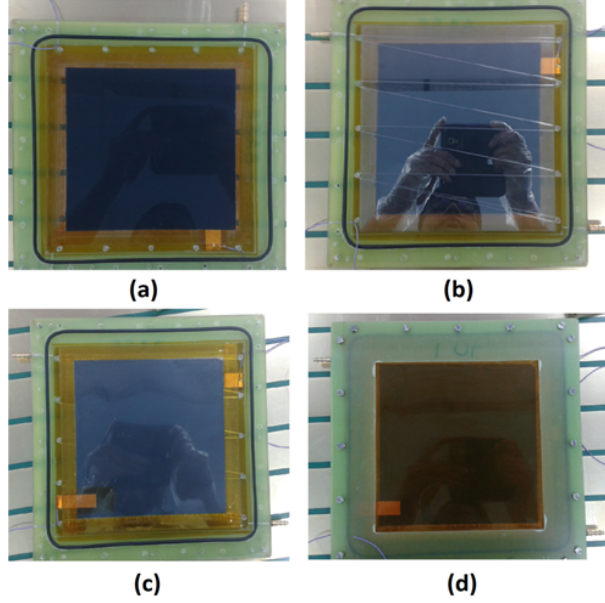


Figure 3.41: Steps of fabrication of the  $18\text{ cm} \times 18\text{ cm}$  prototype MRPC module a) The graphite coated electrode is placed on the frame made of “Perspex”. The nylon screws are placed to define the gas gaps and the provision for the application of High Voltage has also been made. b) The  $250\text{ }\mu\text{m}$  fishing line is used to define the gas gap c) Four inner glass plates are subsequently stacked and the outer electrode is placed at the top d) The top part of the frame is placed and the complete gas-tight module is then flushed with gas, ready to be operated in the avalanche mode.

custom-made holes. The detector has two gas nozzles for gas throughput and wires are soldered on both sides for the application of high voltage.  $\text{CAF}_4$  is applied at the soldering joints for insulation. The prototypes are tested in the Avalanche mode, using an identical gas mixture of Freon and Iso-butane in the ratio 95 : 5 as used for the MTD MRPC modules. This new 2-MRPC set-up has been built as an improvement of the previous work, where the plastic scintillator is being replaced by an identical MRPC, aimed at improving the overall measurement.

### 3.7.8 Preliminary timing resolution measurement

As shown in Fig. 3.42, a cosmic ray test-setup is made to test the timing resolution of the two MRPC prototypes. The detector time resolution is tested with a scintillator-based cosmic ray muon telescope and also in coincidence with each other. In the first case, the scintillator

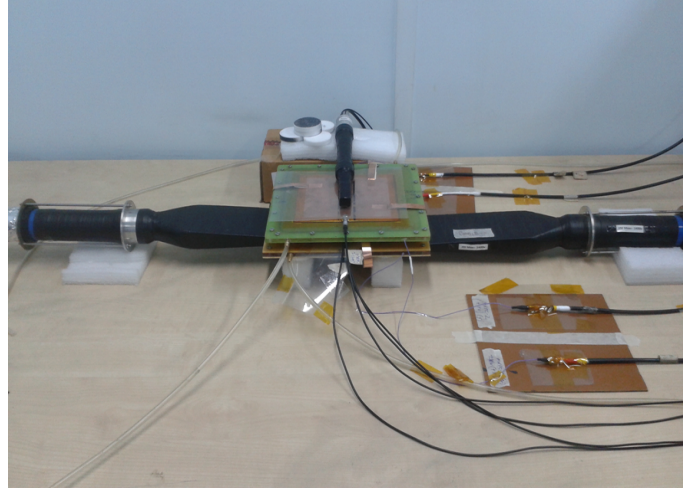


Figure 3.42: The two-MRPC coincidence setup for testing the detector timing resolution.

telescope is built with 3 plastic scintillators arranged as shown in Fig. 3.42. The dimensions of the two paddle scintillators are  $20\text{ cm} \times 8.5\text{ cm}$ , while the finger scintillator is  $5\text{ cm} \times 1.5\text{ cm}$ . The detector readout is in the form of copper strips of size 2 cm with a gap of 2 mm in between. The master trigger is defined as the coincidence of the scintillator signals (3-fold or 3F) and is connected to the TDC start, while the MRPC logic signal is sent to the TDC-stop after a fixed 50 ns delay. The TDC module used for the test is a PS 7186 TDC. The data acquisition system is CAMAC-based. Fig. 3.43 shows the variation of detector time resolution as a function of the applied high voltage. A resolution  $\sim 120\text{ ps}$  has been obtained at the operating voltage of  $\pm 7900\text{ Volts}$  (15.8 kV) after subtracting scintillator contribution. All measurements have been done using a 4 channel CANBERRA 454, Constant Fraction Discriminator for digitising the analog pulses. The TOF-PET sensitivity depends heavily on detector time resolution and the excellent time resolution  $\sim 120\text{ ps}$  obtained with the new MRPC prototype is promising for future tests with the  $^{22}\text{Na}$  source.

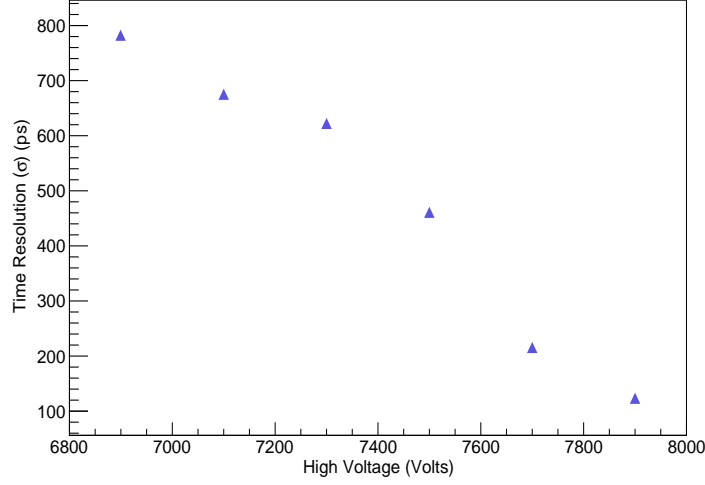


Figure 3.43: Timing resolution measured with Scintillator 3-fold as TDC-Start and delayed detector logic pulse as TDC-Stop. The error bars are within marker size.

### 3.8 Conclusions and Outlook

The responsibility of VECC towards the STAR-MTD project of building 10% of the required modules has been successfully completed. 10 MRPC modules were tested thoroughly at VECC and then shipped to UT, Austin for further tests. There were quite a few issues with detector fabrication, but, they were sorted during the course of the process. One of the modules was shipped to USTC for further tests before being shipped to UT, Austin. The modules were tested OK. A six-gap glass MRPC tested in the avalanche mode with 511 keV photon pairs from a  $^{22}\text{Na}$  source showed a clear signal of photon pairs above background as detected by a scintillator and MRPC coincidence [69][70]. A preliminary effort to identify the source location using the MRPC-scintillator coincident timing distribution was successful and matched the calculated data within error bar [69][70]. A two-MRPC coincidence set-up has been built, which is expected to give better estimation of the ability of the system to detect photons from the  $^{22}\text{Na}$  source in coincidence, due to better detector resolution. Preliminary results indicate the time resolution of the newly fabricated 5-gap detectors to be  $\sim 120$  ps at the operating voltage of 15.8 kV, while tests with the source are currently ongoing.

# Bibliography

- [1] F.N. Flakus, IAEA BULLETIN, VOL 23, No 4.
- [2] Fabio Sauli, Gaseous Radiation Detectors, Fundamentals and Applications, Cambridge University Press.
- [3] W. R. Leo: Techniques for Nuclear and Particle Physics Experiments, 2nd Edition, Springer-Verlag Berlin Heidelberg, 1994.
- [4] G. F. Knoll: Radiation Detection and Measurement, 3rd Edition, John Wiley& Sons, Inc.
- [5] Saikat Biswas, PhD Thesis, University of Calcutta, India, 2010.
- [6] Satyanarayana Bheesette, PhD Thesis, Indian Institute of Technology Bombay, India, 2009.
- [7] Maria Monica Necchi, PhD Thesis, University of Pavia, Italy, 2008.
- [8] Christian Lippmann, PhD Thesis, Goethe University Frankfurt, Germany, 2003.
- [9] Daniele de Gruttola, PhD Thesis, University of Salerno, Italy, 2007.
- [10] J. W. Keuffel, Phys. Rev. 73, 531 (1948).
- [11] J. W. Keuffel, Rev. Sci. Instr. 20, 202 (1949).
- [12] V.V. Parchomchuck, Yu.N. Pestov, N.V. Petrovykh, Nucl. Instr. and Meth. 93 (1971) 269
- [13] Y. Pestov, Nucl. Instr. and Meth., 196, (1982), 45

- [14] M C S Williams, J. Phys. G: Nucl. Part. Phys. 39 (2012) 123001.
- [15] Yu. Pestov. Ric. Sci. Educ. Perm, 112:604–621, 1998. presented in the 36th International Winter Meeting on Nuclear Physics, Bormio, Italy, 1998.
- [16] A. Akimov et al. , Nucl. Instr. and Meth., A 344 (1994) 120.
- [17] A. Arefiev et al., Nucl. Instr. and Meth., A 348, (1994) , 318.
- [18] ALICE TOF - Time-of-flight technical design report. CERN/LHCC 2000-012, ALICE TDR 8, 2000.
- [19] Akimov V A et al 2002 Instrum. Exp. Tech. 45 493
- [20] R. Santonico, R. Cardarelli, Nucl. Inst. and Meth. 187 (1981) 377.
- [21] R. Cardarelli et al., Nucl. Inst. and Meth. A 263 (1988) 20.
- [22] T. Ferbel, Experimental Techniques in High-Energy Nuclear and Particle Physics, Second Edition.
- [23] F. Sauli, “Principles of operation of multiwire proportional and drift chambers”, CERN Yellow report CERN 77-09.
- [24] Santonico R 1996 Topics in resistive plate chambers 3rd Int. Workshop on Resistive Plate Chambers (Pavia, 1995) Sci. Acta 11 1.
- [25] Jane T. Bromley, Masters Thesis, 1994, University of Manchester.
- [26] Raether H 1964, Electron Avalanches and Breakdown in Gases (London: Butterworths).
- [27] S. Narita , Y. Hoshi et al, Nucl. Inst. and Meth. A 602 (2009) 814
- [28] E. Cerron Zeballos,I. Crotty, D. Hatzifotiadou, J. Lamas Valverde, S.Neupane, M.C.S. Williams, A. Zichichi, Nucl. Inst. and Meth. A 374 (1996) 132-135.



- [29] Riegler W, Lippmann C and Veenhof R, Nucl. Inst. and Meth. A 500 (2003) 144.
- [30] Lippmann C and Riegler W , Nucl. Inst. and Meth. A 517 (2004) 54.
- [31] Lippmann C and Riegler W , Nucl. Inst. and Meth. A 533 (2004) 11.
- [32] Doroud K, Afarideh H, Hatzifotiadou D, Rahighi J, Williams M C S and Zichichi A 2009 Nucl. Instrum. Methods A 610 649.
- [33] Gy. L. Benze et al., Nucl. Inst. and Meth A 340 (1994) 466.
- [34] G. Carlino. The RPC trigger system of L3: history and current status. Scientifica Acta, 13:269–280, 1998.
- [35] A. Zallo. The BABAR RPC system. Nucl. Instr. Meth., A 456 (2000) 117.
- [36] K. Abe et al. Glass RPC module for the BELLE endcap  $K_L/\mu$  detector. Scientifica Acta, 13:281–293, 1998.
- [37] ALICE muon spectrometer technical design report. CERN/LHCC 99-22, ALICE TDR 5, page 145, 1999 ; Addendum to the ALICE muon spectrometer technical design report. CERN/LHCC 2000-046, Addendum 1 to ALICE TDR 5, pages 44–46, 2000.
- [38] Yuguang Xie et al., Nucl. Instrum. Meth. A 599, (2009), 20 ; Jiawen Zhang et al., Nucl. Instrum. Meth. A 540, (2005), 102.
- [39] S. Dusini et al. Design and prototype tests of the RPC system for the OPERA spectrometers. presented at the 'RPC 2001 – 6th Workshop on Resistive Plate Chambers and Related Detectors, 26-27 November 2001, Coimbra, Portugal.
- [40] C. Bacci et al., Nucl. Instr. Meth., A 546:121–125, 2000.
- [41] ATLAS Technical Design Report, Muon Spectrometer, CERN/LHCC/97-22, Geneva, 1997.
- [42] CMS-Technical Proposal, CERN/LHCC/94-38, December 1994.

- [43] LHCb Collaboration, CERN-LHCC-2001-010, (2001).
- [44] Byungsik Hong, Nucl. Instrum. Meth. A 602, (2009), 644.
- [45] M.Bogomilov et al., Proc. Workshop on RPCs and Related Detectors, Coimbra,Portugal, (2001);M.Bogomilov et al., Nucl. Instrum. Meth. A 508, (2003), 152.
- [46] ALICE TOF - Time-of-flight technical design report. CERN/LHCC 2000-012, ALICE TDR 8, 2000.
- [47] W.J. Llope, Nucl. Instrum. Meth. A 661 (2012) S110–S113 ;
- [48] A. Schüttauf et al., Nucl. Instrum. Meth. A 602, (2009), 679.
- [49] D.Belver et al., Nucl. Instrum. Meth. A 602, (2009), 687.
- [50] INO Collaboration, Detailed Project Report I, (2007).
- [51] C Yang et al for the STAR Collaboration, Calibration and performance of the STAR Muon Telescope Detector using cosmic rays, Nucl. Instrum. Meth. A 762 (2014) 1.
- [52] Y. Sun et al., Nucl. Instr. Meth. A 593, 307 (2008); Y. Wang et al., Nucl. Instr. Meth. A 640, 85 (2011).
- [53] L. Ruan et al., J. Phys. G 36, 095001 (2009); Z. Xu, BNL LDRD project 07-007; Beam Test Experiment (T963) at FermiLab.
- [54] A. Blanco, et al., Nucl. Instr. and Meth. A 508 (2003) 88.
- [55] M. Couceiro, et al., Nucl. Instr. and Meth. A 580 (2007) 915.
- [56] J.S. Karp et al., J Nucl Med. 2008 March ; 49(3): 462–470 ; J.S. Karp et al., MEDICA-MUNDI 52/1 2008/07 ; J.S. Karp, Time-of-Flight PET, SNM advancing molecular imaging and therapy, volume 3, issue 3 (2006) [<http://snmmi.files.cms-plus.com/docs/PETCENewsFall06.pdf>].

- [57] B. Pavlov et al., 2013 JINST 8 P01011.
- [58] Lewellen TK. Time-of-Flight PET. Semin Nucl Med 1998; 28(3):268-275.
- [59] Moses WW. Time of Flight in PET Revisited. IEEE Trans Nucl Sci 2003; 50(5): 1325-1330.
- [60] T.F. Budinger, J. Nucl. Med. 24 (1983) 73
- [61] P. Fonte, IEEE Transactions on Nuclear Science, 49 (2002) 881–887.
- [62] A. Blanco et al, IEEE Transactions on Nuclear Science, 53, (2006) 2489–2494.
- [63] G. Belli et al. Journal of Physics: Conference Series 41 (2006) 555–560.
- [64] J.E.Bateman, Nucl. Instr. and Meth 221 (1981) 131.
- [65] M. Abbrescia et al, Nucl. Instrum. Meth. A 550 (2005) 116–126 ; G. Chiodini et al, Nucl. Instrum. Meth. A 581 (2007) 213–216.
- [66] C. Williams et al, Nucl. Instr. Meth. A 594 (2008) 39–43.
- [67] F. Sauli et al., Nucl. Instrum. Meth. A. 778 (2015) 85–91.
- [68] A. Banerjee et al., Nucl. Instrum. Meth. A. 718 (2013) 138.
- [69] A. Roy et al., 2014 JINST 9 C10030.
- [70] A. Banerjee, PhD Thesis, Homi Bhabha National Institute, India, 2015.

## Chapter 4

# Charged-neutral correlation Analysis at forward rapidity

### 4.1 Introduction

This chapter focusses on the measurement of event-by-event (e-by-e) fluctuations and correlations between charged (ch) and neutral particle ( $\gamma$ ) multiplicities at the forward rapidity for Au+Au collisions at RHIC. In the framework of the STAR experiment, the two forward detectors, the Photon Multiplicity Detector (PMD) and the Forward Time Projection Chamber (FTPC) simultaneously measure photons and charged particles respectively. The common pseudorapidity coverage of the two detectors in which the measurement is performed is  $-3.7 < \eta < -2.8$ . This unique analysis has been done for the first time at STAR for a wide range of Au+Au Beam Energy Scan (BES) energies,  $\sqrt{s_{NN}} = 200, 62.4, 39, 27, 19.6$  GeV, to gather information regarding the nature of the chiral phase transition. The primary objective is to investigate the possible evidences of dynamical charged-neutral correlations beyond model predictions for generic pion production. A comparative study of charged-neutral correlations and net-charge correlations has also been undertaken, where results obtained for the BES energies have been compared to published results obtained at  $\sqrt{s_{NN}} = 200$  GeV [8]. Details of the energy, collision

centrality and charge dependence of charged-neutral correlation for the energies 200, 62.4, 39, 27, 19.6 GeV has been presented in this thesis. Two special observables,  $\nu_{dyn}^{\gamma-ch}$  and  $r_{m,1}^{\gamma-ch}$  ( $m = 1-3$ ) constructed out of the factorial moments of the charged and neutral particle multiplicities have been used for this analysis. These observables are designed to study the ch- $\gamma$  correlation and are robust against detector inefficiencies by construction. The details about the analysis procedure, datasets used, data cleanup and limitations of the measurement of ch- $\gamma$  correlation in the context of the STAR experiment and the experimental results obtained have been discussed in this chapter in detail.

## 4.2 Method of analysis

The predominant contribution to the charged and neutral particle multiplicity produced in heavy-ion collisions is in the form of charged ( $\pi^\pm$ ) and neutral pions ( $\pi^0$ ) [1] respectively. As the neutral pion decays into photons, the experimental detection of neutral pions is via photons. The presence of any kind of correlation in pion production is reciprocated by a correlation between charged and neutral particles, or more specifically between charged particles and photons. As has been already discussed, a phase transition from the sQGP phase to the Hadronic gas phase can lead to the creation of metastable domains of Disoriented Chiral Condensate (DCC) [2–5]. The distribution of the neutral pion fraction as a result of the decay of the metastable DCC domains is theoretically predicted to be distinctly different from the generic expectation of pion production in equal abundances due to isospin symmetry [3][5]. This phenomenon manifests in the form of an anti-correlation between charged and neutral pion multiplicities [4]. As predicted in [2–5], the ratio of charged-to-neutral pions carries sensitive information about the chiral phase transition. The quantity of interest for this analysis is the neutral pion fraction ( $f$ ) which can be expressed as

$$f = N_{\pi^0} / (N_{\pi^0} + N_{\pi^\pm}) \quad (4.1)$$

to a close approximation [6][7], the value of  $f$  can be written as

$$f^{\gamma-ch} = N_{\gamma}/(N_{\gamma} + 2N_{ch}) \quad (4.2)$$

which explains the study of the ch- $\gamma$  correlation.

The motivation behind this analysis is to look for dynamical evidences of ch- $\gamma$  (anti)correlation beyond generic expectation in Au+Au collisions at RHIC and to search for qualitative differences with net-charge correlation in the same acceptance [8]. It will also be interesting to look at the energy dependence of the ch- $\gamma$  correlation for the BES energies. Measurement of ch- $\gamma$  correlation requires a simultaneous measurement of charged particles and photons within a common acceptance. In the framework of the STAR experiment [9], this is possible both at mid-rapidity and forward rapidity. At midrapidity ( $|\eta| < 1$ ), the TPC [10] measures charged particles, while the BEMC [11] measures photons. The inability of the BEMC to detect photons less than 500 MeV in momentum is a major impediment to this analysis, considering theoretical predictions that claim the average momentum of pions produced from the decay of DCC domains is inversely proportional to DCC domain size [12]. At forward rapidity ( $-3.7 < \eta < -2.8$ ), the FTPC [13] and PMD [14] detectors measure charged particles and photons respectively. The FTPC measures charged particles of transverse momentum ( $p_T$ ) as low as 150 MeV/c, while the PMD measures photons down to 20 MeV/c in transverse momentum with reasonable efficiency. This analysis deals with the e-by-e measurement of charged and neutral particle multiplicity fluctuation in the common PMD-FTPC acceptance within the pseudorapidity range  $-3.7 < \eta < -2.8$ . The observables chosen for this analysis  $\nu_{dyn}^{\gamma-ch}$  and  $r_{m,1}^{\gamma-ch}$  ( $m = 1-3$ ), to be described in detail in the next section, have been developed using a proper combination of factorial moments of the charged and neutral particle multiplicities, expressed in terms of the neutral pion fraction ( $f$ ). The use of these observables and the methodology followed for the charged-neutral analysis described in this thesis is well documented [7][15][16]. The observables have been specifically constructed for

sensitivity towards dynamical signals of ch- $\gamma$  correlation.

#### 4.2.1 Choice of suitable observables for ch- $\gamma$ correlation

In heavy-ion collisions, there are inherent limitations in the measurement of experimental observables. The detector response being binomial [6], fluctuations in the measurements of particle numbers is automatically introduced. Additional detector artefacts like limited acceptance, particle decay and mis-identification of particles introduce further spurious correlations in data. Selection of robust observables for the event-by-event study of multiplicity fluctuations, that minimize the effects of spurious correlations is naturally very important. Specifically designed observables that are sensitive towards ch- $\gamma$  correlation have been used for this analysis [6]. The use of the observable  $\nu_{dyn}$  for studying particle ratio fluctuations in heavy ion collisions is well known and was introduced in [16]. The observable  $\nu_{dyn}^{\gamma-\text{ch}}$ , for the special case of charged-neutral correlation is defined as

$$\nu_{dyn}^{\gamma-\text{ch}} = \frac{\langle N_{\text{ch}}(N_{\text{ch}} - 1) \rangle}{\langle N_{\text{ch}} \rangle^2} + \frac{\langle N_{\gamma}(N_{\gamma} - 1) \rangle}{\langle N_{\gamma} \rangle^2} - 2 \frac{\langle N_{\text{ch}} N_{\gamma} \rangle}{\langle N_{\text{ch}} \rangle \langle N_{\gamma} \rangle} \quad (4.3)$$

$$= \omega_{\text{ch}} + \omega_{\gamma} - 2 \times \text{corr}_{\gamma-\text{ch}} \quad (4.4)$$

$$= \left( \frac{\langle (1-f)^2 \rangle}{\langle 1-f \rangle^2} + \frac{\langle f^2 \rangle}{\langle f \rangle^2} - 2 \frac{\langle f(1-f) \rangle}{\langle f \rangle \langle 1-f \rangle} \right) \frac{\langle N(N-1) \rangle}{\langle N \rangle^2} + \frac{1}{2 \langle f \rangle \langle N \rangle}. \quad (4.5)$$

As shown in Eqn.s 4.3 and 4.4,  $\nu_{dyn}^{\gamma-\text{ch}}$  consists of three terms,  $\omega_{\text{ch}}$ , the fluctuation of the number of charged particles,  $\omega_{\gamma}$ , the fluctuation of the number of photons and  $\text{corr}_{\gamma-\text{ch}}$ , which is the scaled ch- $\gamma$  correlation term. The individual terms are constructed out of factorial moments of charged particle and photon multiplicities. In Eqn. 4.5,  $\nu_{dyn}^{\gamma-\text{ch}}$  has been expressed in terms of the neutral pion fraction  $f$ . The Poissonian limit for the individual terms is unity, hence, for purely statistical fluctuations, the observable  $\nu_{dyn}$ , is zero by design. In presence of dynamical fluctuations from any source of origin, the value of  $\nu_{dyn}$  should be non-zero [16–18]. The other advantage of using  $\nu_{dyn}$  is its robustness against detector effects like efficiency, acceptance

[19][20]. Using the generating function approach [15], the robustness of the observables against detector inefficiencies and sensitivity towards signals of ch- $\gamma$  correlation has been shown [6][7].  $\nu_{\text{dyn}}$  has a strong centrality dependence which arises due to its dependence on the initial gluon multiplicity [7]. According to the ‘‘Central Limit Theorem (CLT)’’ [21][22], the observable  $\nu_{\text{dyn}}^{\gamma\text{-ch}}$  has a  $A + B/\sqrt{\langle N_{\text{ch}} \rangle \langle N_{\gamma} \rangle}$  dependence on the charged particle and photon multiplicities, for the generic case of pion production. The centrality dependence of  $\nu_{\text{dyn}}$  in terms of the average experimental multiplicity observable  $\sqrt{\langle N_{\text{ch}} N_{\gamma} \rangle}$  in the context of ch- $\gamma$  correlation has been explored in this thesis for a range of energies.

The second observable  $r_{m,1}$ , also called the Minimax or the robust observable was used for the first time by the Minimax collaboration [15] for the search of DCC-like phenomenon in p+p collisions.  $r_{m,1}$  is defined in terms of charged particle and photon multiplicities and the neutral pion fraction  $f$  as

$$r_{m,1}^{\gamma\text{-ch}} = \frac{\langle N_{\text{ch}}(N_{\text{ch}} - 1) \cdots (N_{\text{ch}} - m + 1) N_{\gamma} \rangle \langle N_{\text{ch}} \rangle}{\langle N_{\text{ch}}(N_{\text{ch}} - 1) \cdots (N_{\text{ch}} - m) \rangle \langle N_{\gamma} \rangle} = \frac{\langle f(1 - f)^m \rangle \langle 1 - f \rangle}{\langle (1 - f)^{m+1} \rangle \langle f \rangle}. \quad (4.6)$$

The observable is designed to give a value of unity for Poissonian distributions, i.e statistical fluctuations for all the moments. The observable  $r_{m,1}$  for the lowest order of  $m$  ( $r_{1,1}$ ,  $m = 1$ ) can be written in terms of  $\omega_{\text{ch}}$  and  $\text{corr}_{\gamma\text{-ch}}$  as

$$r_{1,1} = \text{corr}_{\gamma\text{-ch}} / \omega_{\text{ch}} \quad (4.7)$$

So, the information carried by  $r_{1,1}$  is the same as  $\nu_{\text{dyn}}$ , but the higher order terms  $r_{2,1}$ ,  $r_{3,1}$  are more sensitive to ch- $\gamma$  correlation signals.  $r_{m,1}$  is independent of detector efficiency [7][15] and the extra sensitivity of its higher order terms towards ch- $\gamma$  correlation is the added advantage of using this observable.  $r_{m,1}$  as a function of  $m$  can be expressed as [7][15][23]



$$r_{m,1}^{\gamma\text{-ch}} = 1 - \frac{m\zeta}{(m+1)} \quad (4.8)$$

where the parameter  $\zeta$  depends on the strength of ch- $\gamma$  (anti-)correlation and its value lies between  $0 \leq |\zeta| \leq 1$ .  $\zeta > 0$  implies anti-correlation and  $\zeta < 0$  implies the presence of correlation between charged and neutral particles.  $\zeta = 0$  is the Poissonian limit for merely statistical fluctuations and this is the generic scenario, when the production of pions following isospin symmetry is in equal abundance. This leads to  $r_{m,1}^{gen} = 1$  [7][15] for the generic case. In the scenario of DCC events  $\zeta = 1$  and  $r_{m,1}^{DCC} = \frac{1}{m+1}$  [7][15]. The centrality and charge dependence of the observables  $\nu_{\text{dyn}}$  and  $r_{m,1}$  for a range of energies has been explored in this work.

#### 4.2.2 Detectors used for the analysis

The simultaneous measurement of photons and charged particles in a common  $\eta$ - $\phi$  phase space at forward rapidity is performed using the Photon Multiplicity Detector(PMD) and the Forward Time Projection Chamber(FTPC). The minimum bias trigger selection for the analysis has been done using a combination of the Zero Degree Calorimeter and the Vertex Position Detector. To prevent self-correlation, charged tracks for the  $\gamma$ -ch correlation measurement and for centrality selection have been chosen from different detector systems ensuring there is no overlap between their rapidity ranges [24]. The minimum-bias uncorrected charged particle multiplicity, also known as reference multiplicity (refmult), measured by the Time Projection Chamber in the pseudorapidity range  $|\eta| < 0.5$  has been used to determine the collision centrality for this analysis.

The pre-shower PMD detector which has already been discussed in Sec. 2.3.3 is designed to measure the multiplicity of photons in the pseudorapidity range of  $-3.7 \leq \eta \leq -2.3$ . The detector consists of two proportional counter planes separated by a lead converter of a thickness equivalent of 3 radiation lengths. The front plane or the CPV (Charged Particle Veto) plane that faces the interaction point is used as a veto plane for hadron rejection. The data from the pre-shower plane, located behind the lead converter which detects the electromagnetic shower

from the photons incident on the converter in the form of large clusters, is used for the analysis.

The two FTPC's located on either side of the collision vertex, at the forward pseudorapidity region  $2.5 < |\eta| < 4.0$ , measure the charge state and transverse momentum of charged particles. The limited space in the FTPC does not allow identification of charged tracks but the use of a radial drift field perpendicular to the magnetic field direction of the STAR magnet helps the FTPC to put up with the high track density. Simulation results show that this design helps the FTPC achieve a two-track resolution upto 2 mm [25]. The detector is described in detail in Sec. 2.3.4. Fig. 4.1 shows the common PMD-FTPC  $\eta$ - $\phi$  coverage used in this analysis for the simultaneous measurement of photons and charged particles in the overlapping pseudorapidity region  $-3.7 < \eta < -2.8$ .

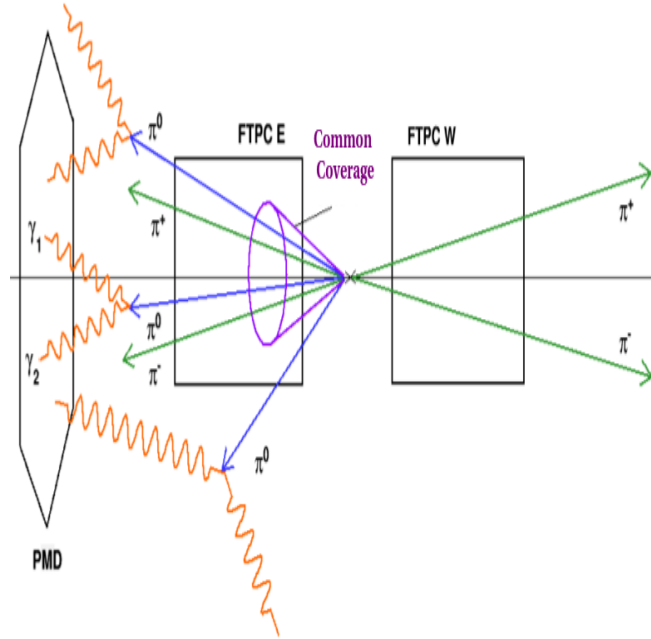


Figure 4.1: A schematic diagram of the common PMD-FTPC acceptance for the measurement of  $\gamma$ -ch correlation.

### 4.2.3 Datasets and Kinematic Cuts for the BES energies

The charged-neutral correlation has been done for Au+Au collisions at the RHIC Beam Energy Scan(BES) energies  $\sqrt{s_{NN}} = 62.4, 39, 27, 19.6$  GeV and compared with the results obtained at  $\sqrt{s_{NN}} = 200$  GeV. The details of the analysis at 200 GeV can be found in [6]. The Au+Au collisions at the four different BES energies took place over the course of two years, 2010 and 2011. The details of the datasets used for this analysis can be found in Table 4.1. As described in the previous section, the analysis was done in the common PMD-FTPC geometric acceptance. The statistics shown against the dataset of each energy is the number of events after the removal of bad runs and applying a narrow z-vertex cut ( $-5 < V_z < 5$ ). The z-vertex is the position of the collision vertex along the z-direction or the direction of the beam axis. The narrow z-vertex cut helps to minimize the variation of the combined geometric acceptance of the PMD and the FTPC detectors, event-by-event.

Table 4.1: Summary of data sets and different kinematic cuts used in this analysis.

Data Set:	Run 10, Au+Au $\sqrt{s_{NN}} = 62.4$ GeV, $\sim 0.5$ M after correction
Data Set:	Run 10, Au+Au $\sqrt{s_{NN}} = 39$ GeV, $\sim 2.2$ M after correction
Data Set:	Run 11, Au+Au $\sqrt{s_{NN}} = 27$ GeV, $\sim 1.1$ M after correction
Data Set:	Run 11, Au+Au $\sqrt{s_{NN}} = 19.6$ GeV, $\sim 0.7$ M after correction
FTPC:	Primary track : number of fit points $> 5$ $-3.7 < \eta < -2.8$ (Common $\eta - \phi$ with PMD) $0.15 < p_T < 1.5$ GeV/c $dca < 3$ cm
PMD:	Cluster ADC cut $> 8 \times \text{MIP}$ $-3.7 < \eta < -2.8$ (Common $\eta - \phi$ with FTPC) number of cells in a cluster $> 1$

The basis of this analysis is the simultaneous measurement of charged particles and photons in the common PMD-FTPC acceptance. The details of the kinematic cuts applied for the selection of charged tracks from the FTPC and the identification of photon clusters after hadron discrimination in the PMD have also been highlighted in Table 4.1. The FTPC does not have particle identification capability, so the analysis is performed on inclusive charged particles. The criteria for the validity of a charged track are at least 5 hits in the FTPC and a distance of

closest approach (dca) from the collision vertex less than 3 cm. The transverse momentum cut for the FTPC,  $0.15 < p_T < 1.5$  GeV/c facilitates the selection of pions of low momentum relevant to this analysis. As discussed in Ref. [25], the choice of the particular set of cuts used here minimizes the contribution from split tracks and keeps the contamination of charged tracks due to  $\gamma$  conversion ( $\gamma \rightarrow e^+ e^-$ ) background below  $\sim 5\%$ . A set of kinematic cuts are also imposed on the PMD for photon cluster selection. The details of the photon cluster extraction procedure can be found in [14]. Charged hadrons giving signals in the PMD affect a single cell on average, hence, the validity of a photon cluster requires the number of cells in a cluster to be more than 1, while the signal strength of the cluster has to be 8 times greater than the average signal strength of all the cells due to a minimum ionizing particle (MIP). A purity of  $\sim 70\%$  can be obtained for photon clusters using this particular set of validity criteria [8] lowering the contribution due to charged particle contamination. The purity of the sample cannot be improved upon by the use of stricter kinematic cuts and an impurity of  $\sim 30\%$  in the photon sample is inherent.

#### 4.2.4 Quality Assurance (QA) plots and Run-by-Run QA for the BES energies

Figs. 4.2 - 4.5 illustrate the plots relevant to this analysis for the energies 62.4, 39, 27 and 19.6 respectively. In these QA plots, the top-left plots shows the distribution of reference multiplicity (refmult), having characteristic shape of the minimum-bias distributions. The reference multiplicity distribution is the uncorrected charged particle multiplicity from the TPC measured in the pseudorapidity region  $|\eta| < 1$ . The top-right plot shows the z-vertex ( $V_z$ ) distribution and the accepted range. The two plots at the bottom of Figs 4.2 - 4.5 show the distributions of the minimum-bias photon cluster (left) and charged track (right) multiplicities from the PMD and FTPC detectors, respectively. These are uncorrected distributions and their ranges reduce as we go down to lower  $\sqrt{s}$  values. The shapes of the photon cluster and the charged track distributions mimic the characteristics of a minimum-bias distribution, highlighting the robustness of

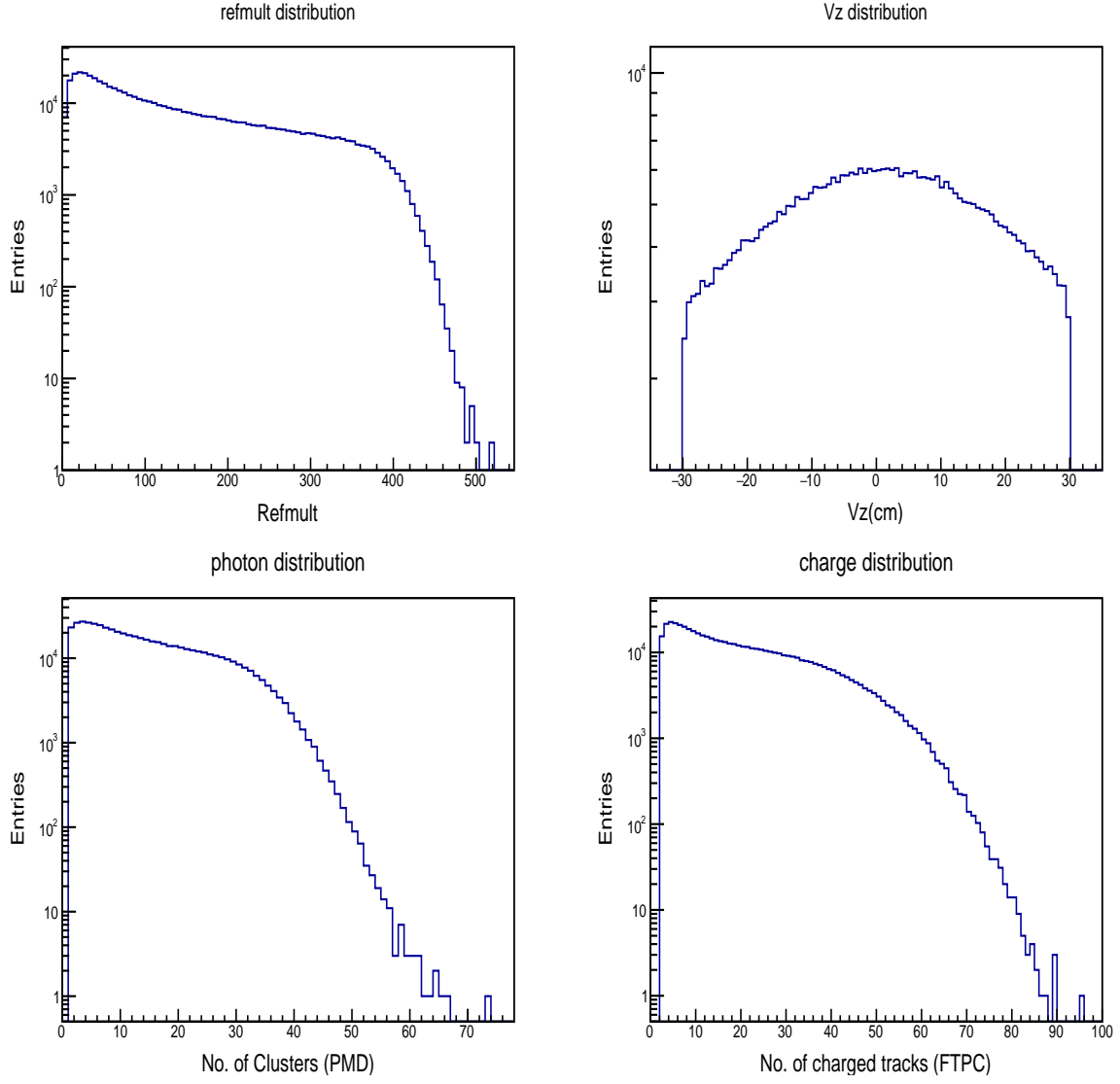


Figure 4.2: QA plots for  $\sqrt{s_{NN}} = 62.4$  GeV

the observables. The selection of event centrality [26] and the correction of the bin-width effect for this analysis have been performed using the refmult distribution. The z-vertex distribution is shown for the range  $-30 < V_z < 30$ .

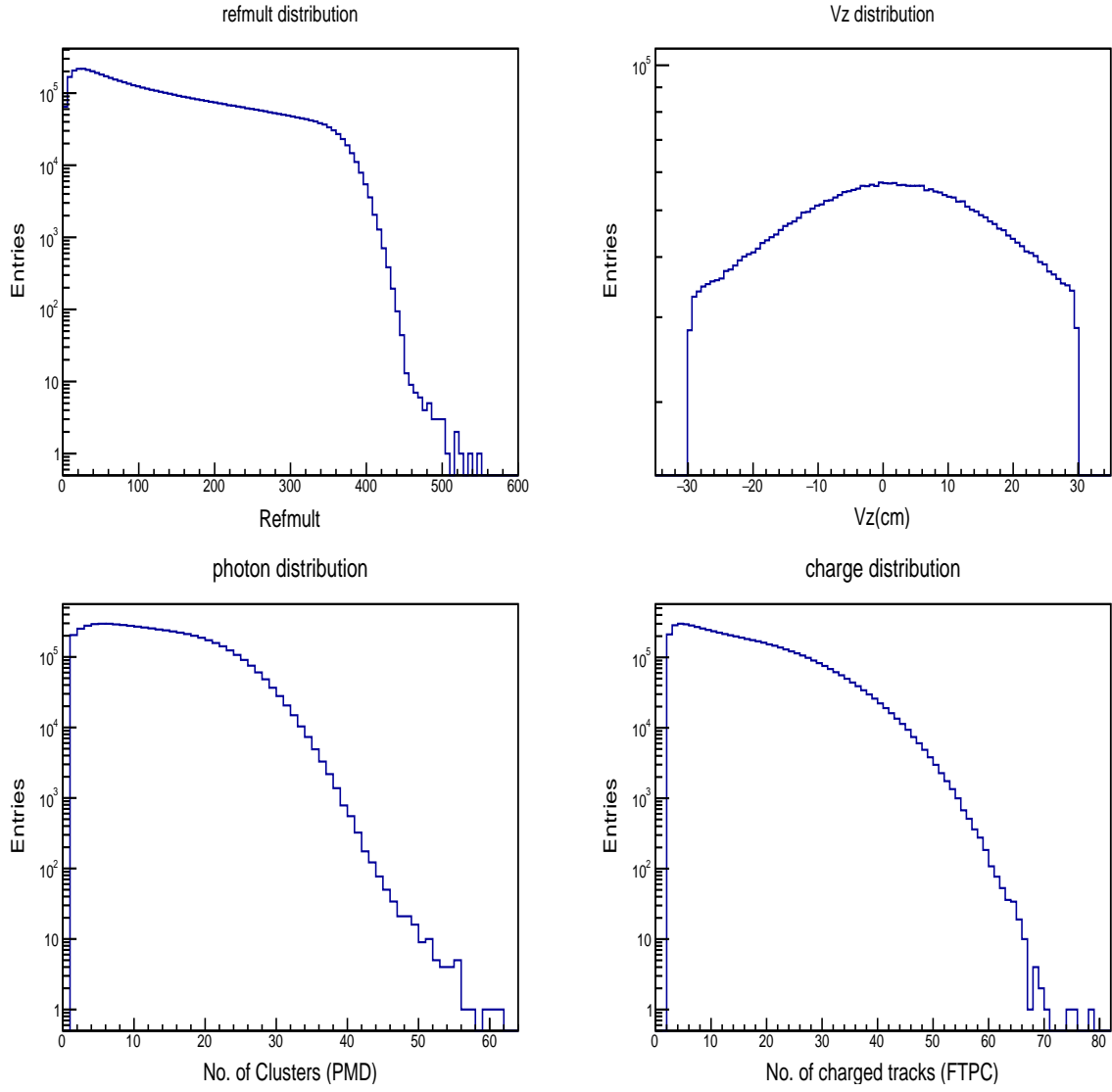


Figure 4.3: QA plots for  $\sqrt{s_{NN}} = 39$  GeV

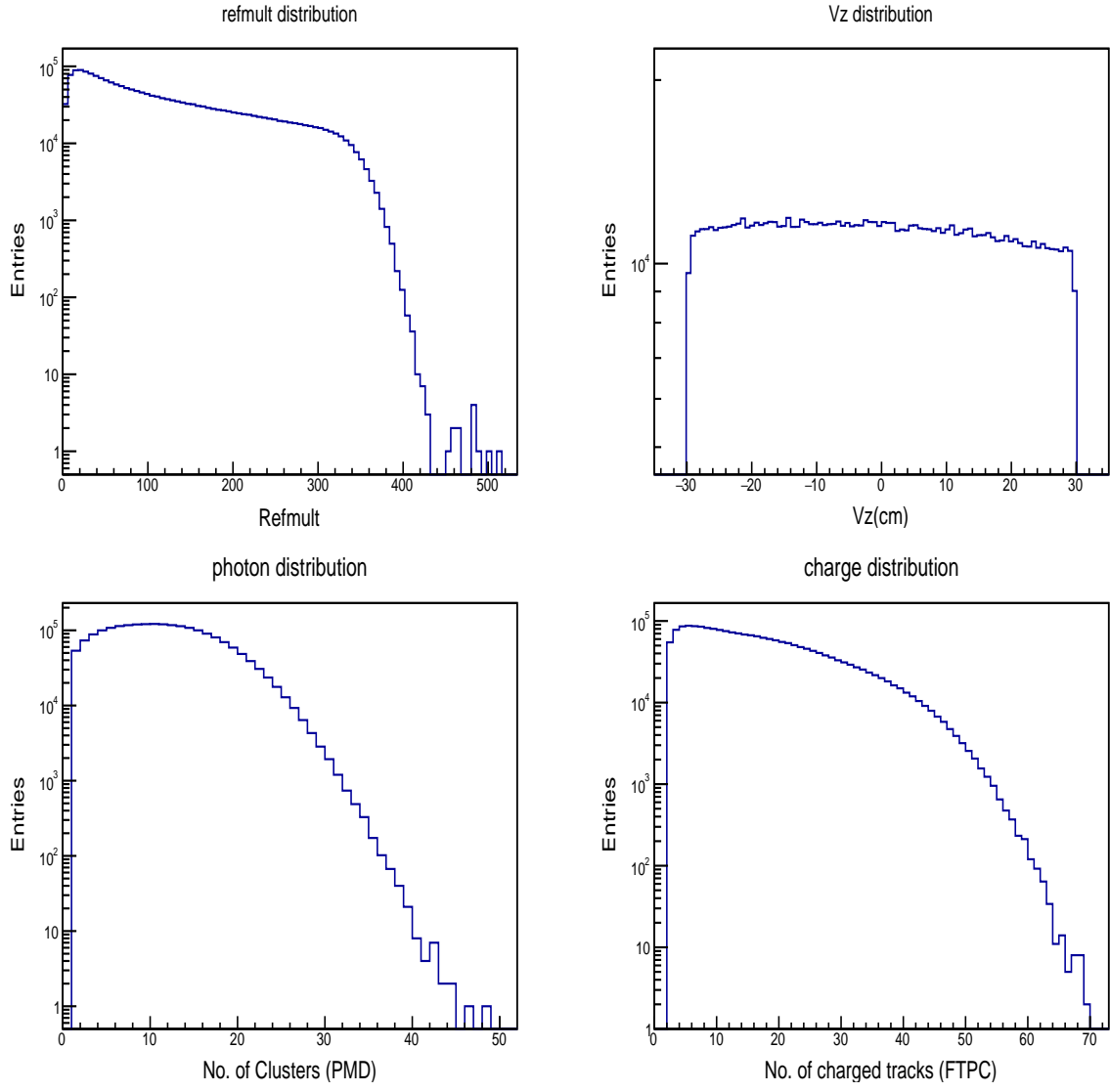


Figure 4.4: QA plots for  $\sqrt{s_{NN}} = 27$  GeV

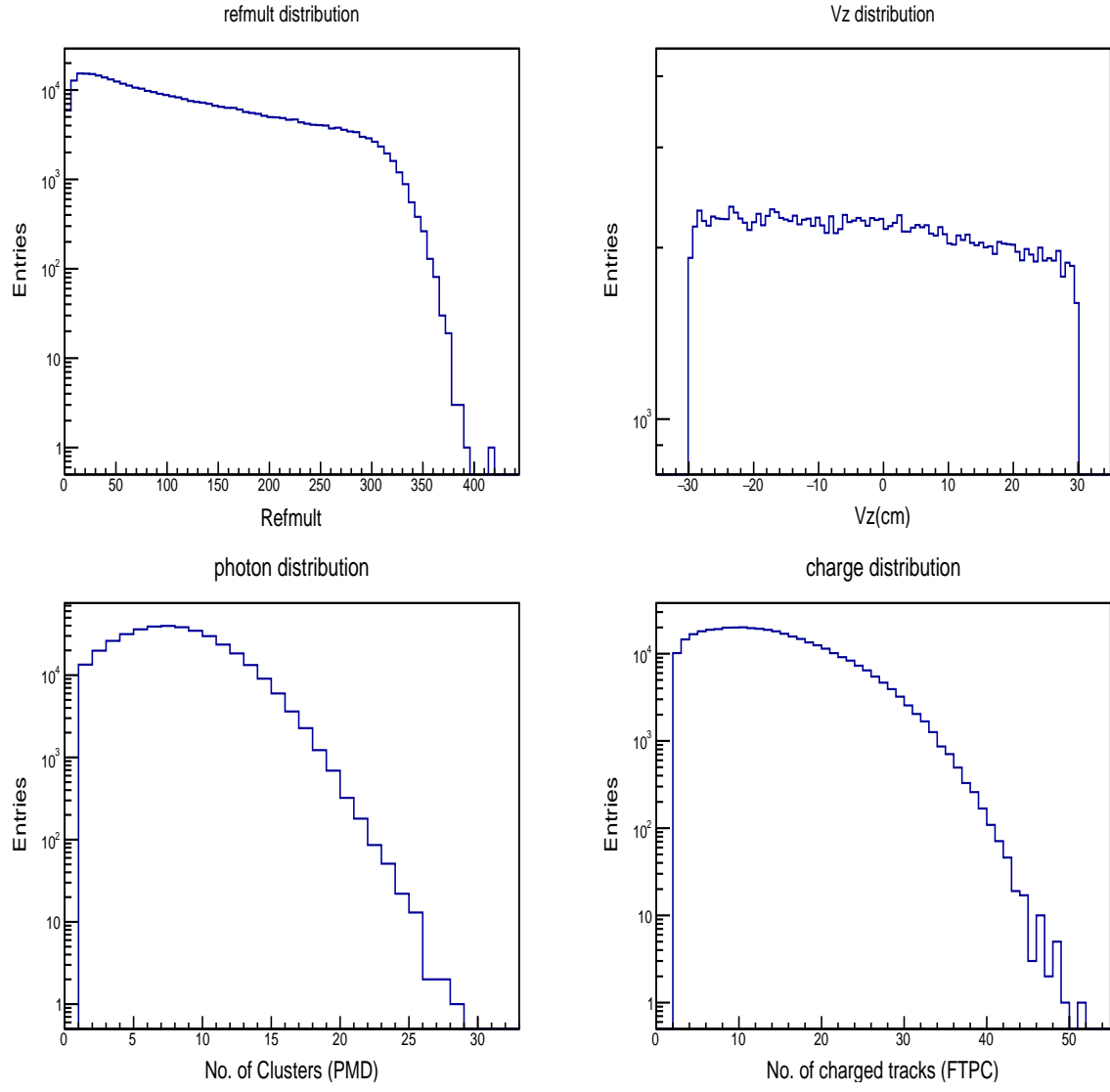


Figure 4.5: QA plots for  $\sqrt{s_{NN}} = 19.6$  GeV



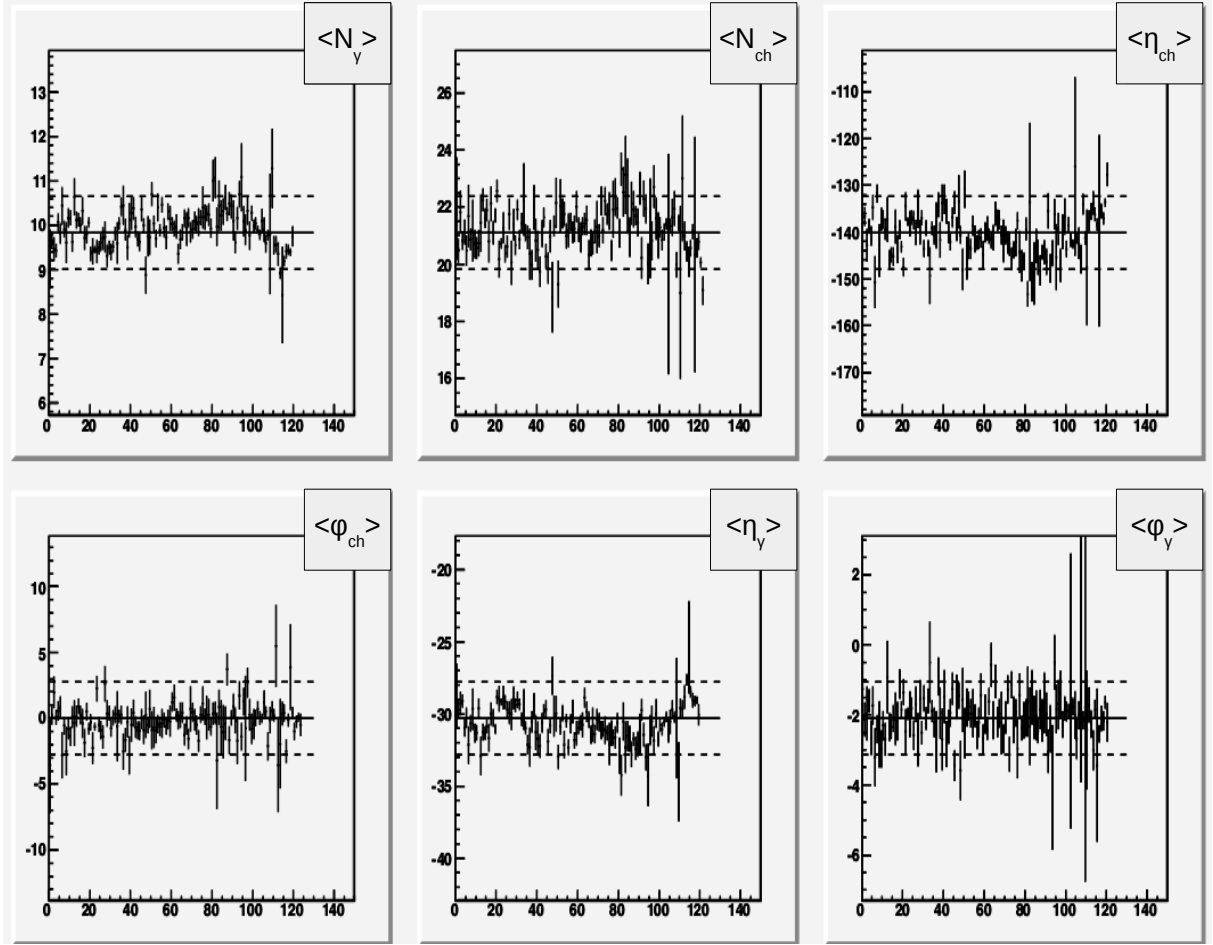


Figure 4.6: Run-by-Run QA plots for  $\sqrt{s_{NN}} = 19$  GeV

Figs. 4.6 - 4.9 illustrate the run-by-run QA plots of the photon and charged particle multiplicities alongwith the quantities related to them plotted versus the run numbers for all BES energies, from 19.6 - 62.4 GeV. The run-by-run QA over the range of run numbers has been done with a stable PMD-FTPC geometric acceptance. The x-axis of the plot shows the range of Run numbers for a particular collisional energy, converted into a Run Index for convenience. The y-axis represents the variation of the quantities  $\langle N_\gamma \rangle$ ,  $\langle N_{ch} \rangle$ ,  $\langle \eta_{ch} \rangle$ ,  $\langle \phi_{ch} \rangle$ ,  $\langle \eta_\gamma \rangle$ ,  $\langle \phi_\gamma \rangle$  averaged over the most central (0-10%) events in a particular run number. The mean of the quantities over the range of run numbers is represented by the solid line, while the two dashed lines represent a  $2\text{-}\sigma$  variation w.r.t. the mean value. A variation greater than  $2\text{-}\sigma$  from the mean-value

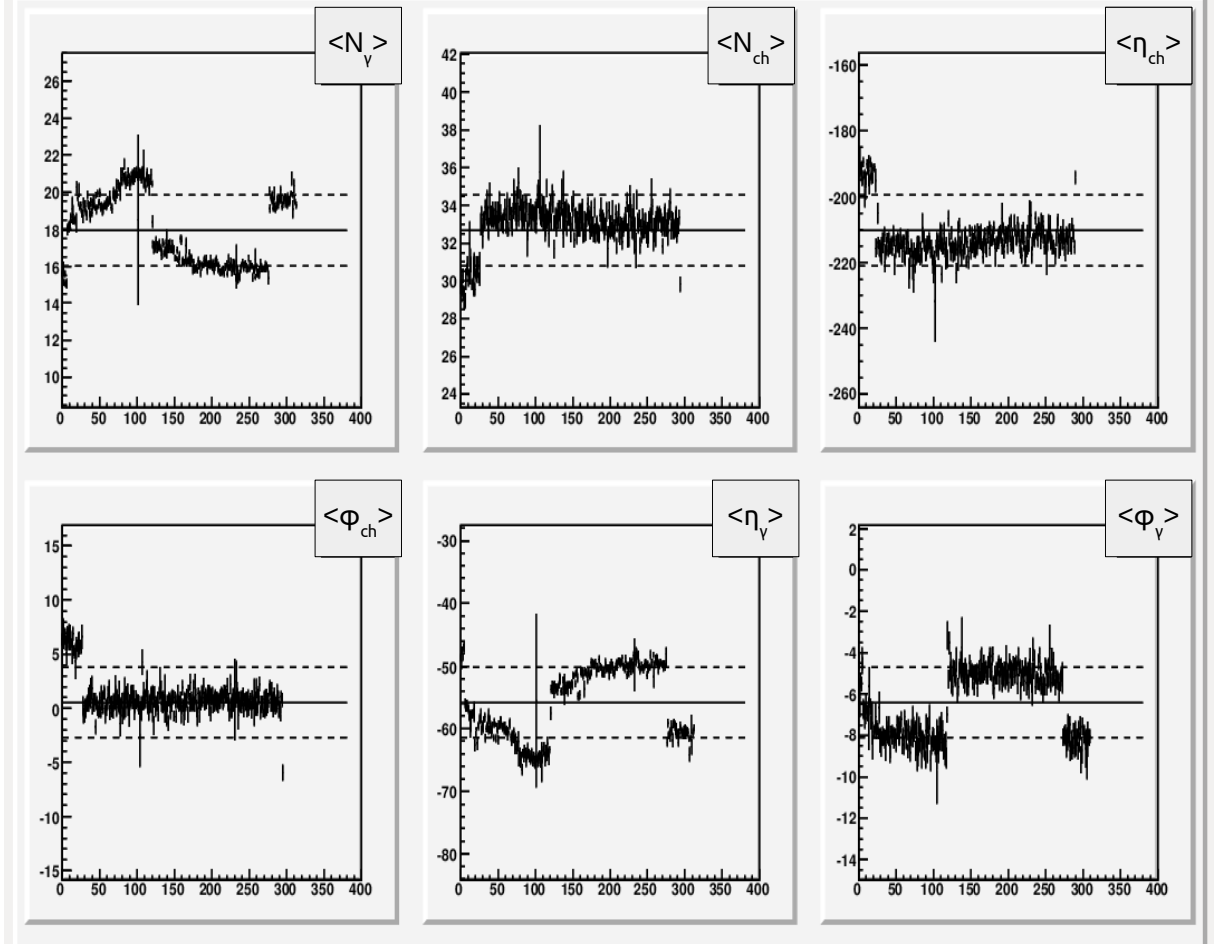


Figure 4.7: Run-by-Run QA plots for  $\sqrt{s_{NN}} = 27$  GeV

for quantities other than the charged particle and photon multiplicities is used to determine the bad runs and those runs have been rejected.

#### 4.2.5 Correction of the Bin-width effect

The selection of centrality (binning of events in terms of multiplicity) in this analysis has been performed using the uncorrected minimum-bias multiplicity distribution at midrapidity (ref-mult), measured by the TPC within ( $|\eta| < 1$ ). This minimum-bias distribution is divided into different centrality bins, but, since the distribution is not flat, this leads to an artefact known as the centrality bin-width effect. The centrality binning is done in terms of a range of the reference

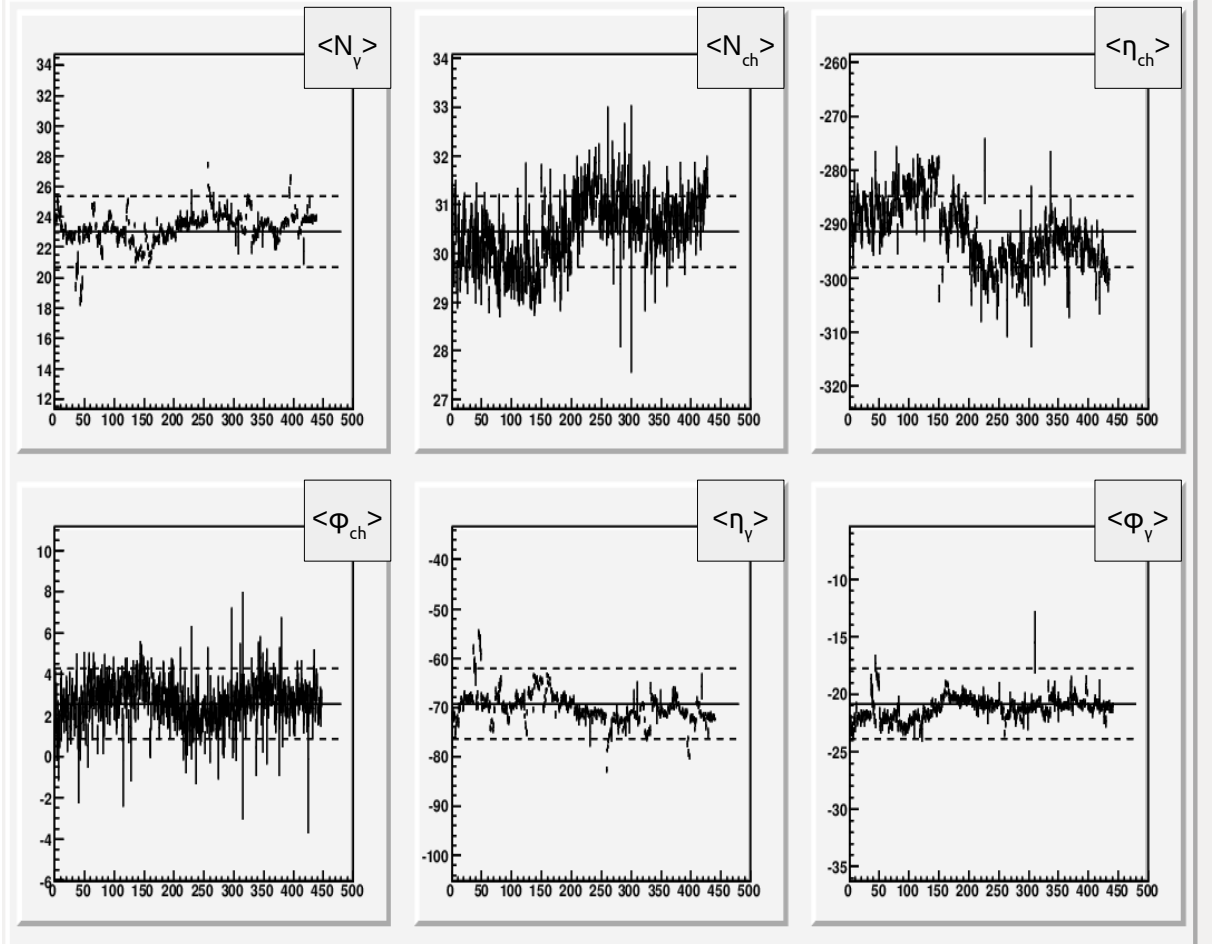


Figure 4.8: Run-by-Run QA plots for  $\sqrt{s_{NN}} = 39$  GeV

multiplicities and is done by dividing the multiplicity distribution accordingly. The distribution has a distinct falling nature at higher multiplicity. So, in the case of most central events and wide centrality bins that include greater variation of the nature of the distribution, the bin-width correction becomes critical. This artefact can thus introduce additional fluctuations by means of an artificial centrality dependence in the final observable [6][24][27][28]. Simulations using the UrQMD model clearly demonstrate the effect of bin-width [24]. The weighted averages of the event-by-event multiplicities of photons and charged particles across the min-bias reference multiplicity distribution corrects for the bin-width effect.

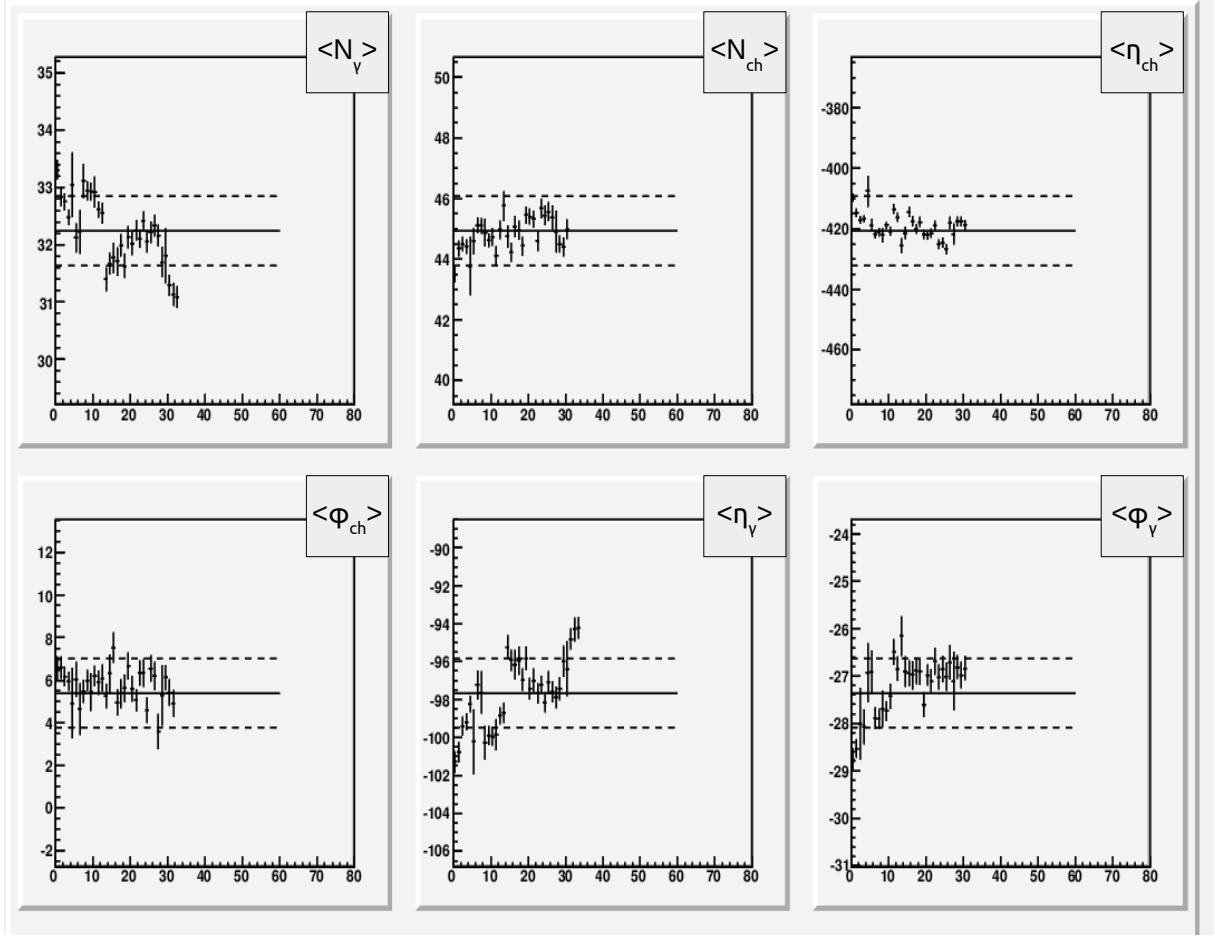


Figure 4.9: Run-by-Run QA plots for  $\sqrt{s_{NN}} = 62.4$  GeV

#### 4.2.6 Error Analysis

##### Statistical Error :

The estimation of statistical error for different observables used in this analysis has been performed using the Bootstrap method [29]. In this statistical technique, the error is estimated by multiple uses of the data sample according to the following procedure :

- ‘n’ number of identical minimum bias data samples are created by reorganizing the event numbers. The number of events in the ‘n’ samples remain the same, but, since the events are not identical, the samples give rise to statistical fluctuations in the values of the

observables.

- The relevant observables  $\nu_{\text{dyn}}$  and  $r_{m,1}$  after bin-width correction are calculated centrality-wise, individually for the 'n' event samples.
- The values of the bin-width corrected observables for the different event samples result in an approximate Gaussian distribution. The variance of this distribution provides the statistical error.

### Systematic Error :

The systematic errors for the two observables  $\nu_{\text{dyn}}$  and  $r_{m,1}$  have been calculated by varying the kinematic cuts applied on charged particles and photons, shown in Table 4.1. The sources of systematic error in this case are variation of the distance of closest approach (dca), variation of the cluster adc cut also known as the MIP cut and the z-vertex cut. The final systematic error value for the observable  $\nu_{\text{dyn}}$  is obtained by adding the three different sources of errors in quadrature as shown below :

$$sysErr(\nu_{\text{dyn}})^{total} = \sqrt{(\nu_{\text{dyn}}^{std} - (\nu_{\text{dyn}})^{\Delta dca})^2 + (\nu_{\text{dyn}}^{std} - (\nu_{\text{dyn}})^{\Delta MIP})^2 + (\nu_{\text{dyn}}^{std} - (\nu_{\text{dyn}})^{\Delta V_z})^2} \quad (4.9)$$

while the final systematic error value for  $r_{m,1}$  can be expressed as :

$$sysErr(r_{m,1})^{total} = \sqrt{(r_{m,1}^{std} - (r_{m,1})^{\Delta dca})^2 + (r_{m,1}^{std} - (r_{m,1})^{\Delta MIP})^2 + (r_{m,1}^{std} - (r_{m,1})^{\Delta V_z})^2} \quad (4.10)$$

The standard values of the observables,  $\nu_{\text{dyn}}^{std}$  and  $r_{m,1}^{std}$  have been obtained by calculating the observables after implementing the standard cuts as shown in Table 4.1.

#### 4.2.7 Limitations of the ch- $\gamma$ correlation analysis

The ch- $\gamma$  correlation in the framework of the STAR experiment certainly has its share of limitations. They have been highlighted below :

- The PMD detector does not have the capability to measure photon momentum. As such, the analysis can not be performed specifically with low momentum photons as is the requirement according to theoretical predictions [8].
- Ideally, this analysis should be restricted to photons coming from the decay of neutral pions ( $\pi^0$ ), but, due to unavailability of the momentum information, all photons are selected [8].
- Similarly, for the charged tracks, a lack of particle identification in the FTPC means all charged tracks are selected for the analysis, not just charged pions ( $\pi^\pm$ ) [8].
- Although there is an overlap in the photon and charged particle momentum ranges, their momentum ranges are not identical. The photons selected in this analysis have reasonable efficiency for  $p_T > 20$  MeV/c are selected in the analysis, while all charged particles within  $0.15 < p_T < 1.5$  GeV/c are selected [8].

So, to work around all these limitations, it is extremely crucial to have an identical  $\eta$ - $\phi$  phase space for the photons and charged particles. That is why, the analysis is done with charged particles and photons selected within the common PMD-FTPC acceptance. Moreover, for the published charged-neutral correlation results at the top RHIC energy, conclusions are derived only after detailed comparisons with particle production models like HIJING, GEANT+HIJING and Mixed event study, as will be shown in the next section [8].

### 4.3 Results for Au+Au collisions at $\sqrt{s_{NN}} = 200$ GeV and at BES energies

The centrality (multiplicity) dependence of the three individual terms  $\omega_{\text{ch}}$ ,  $\text{corr}_{\gamma-\text{ch}}$  and  $\omega_{\gamma}$  of the observable  $\nu_{\text{dyn}}^{\gamma-\text{ch}}$  have been shown in Fig. 4.10(a)-4.10(c) [8] for  $\sqrt{s_{NN}} = 200$  GeV and all three terms show a similar trend. The values of real data have been compared with mixed events. At higher values of multiplicity, all three terms approach their Poissonian limit. The mixed events are created by mixing raw charged tracks and photon clusters from different events of identical centrality and narrow z-vertex cut. The multiplicity of raw tracks and clusters is the same as that of a particular real event and similar kinematic cuts as real data are applied to it. Mixed events by design have only statistical fluctuations and the large deviation from the Poissonian limit can be attributed to finite multiplicity. Mixed event values approach their Poissonian limit for most central events. The higher values of  $\omega_{\text{ch}}$  [Fig. 4.10 (a)] and  $\omega_{\gamma}$  [Fig. 4.10 (c)] compared to mixed events indicate the presence of fluctuations other than statistical in origin.

The decay of neutral pions ( $\pi^0$ ) to photons, introduces additional fluctuations in the  $\omega_{\gamma}$  term which explains the higher difference in values between the real and mixed events for the observable, a feature seen also for the simulated HIJING events. The correlation term  $\text{corr}_{\gamma-\text{ch}}$  [Fig. 4.10(b)] is higher compared to mixed events for peripheral events, comparable at mid-central events and lower for most central events. The variation of the observable  $\nu_{\text{dyn}}^{\gamma-\text{ch}}$  as a function of  $\sqrt{\langle N_{\text{ch}} N_{\gamma} \rangle}$  is shown in Fig. 4.10(d). While real data show a non-zero, positive value of  $\nu_{\text{dyn}}$  at all centralities, mixed event values for all centralities are consistent with Poissonian expectations, as per the design of  $\nu_{\text{dyn}}$  that statistical fluctuations are eliminated. The data is fit with a function of the form  $A + B/\sqrt{\langle N_{\text{ch}} \rangle \langle N_{\gamma} \rangle}$  consistent with CLT predictions [7]. The calculations for data are also compared to results obtained for simulated events using the particle production model HIJING and HIJING simulated through GEANT to incorporate detector effects that might be present in the data sample. The simulation results are close

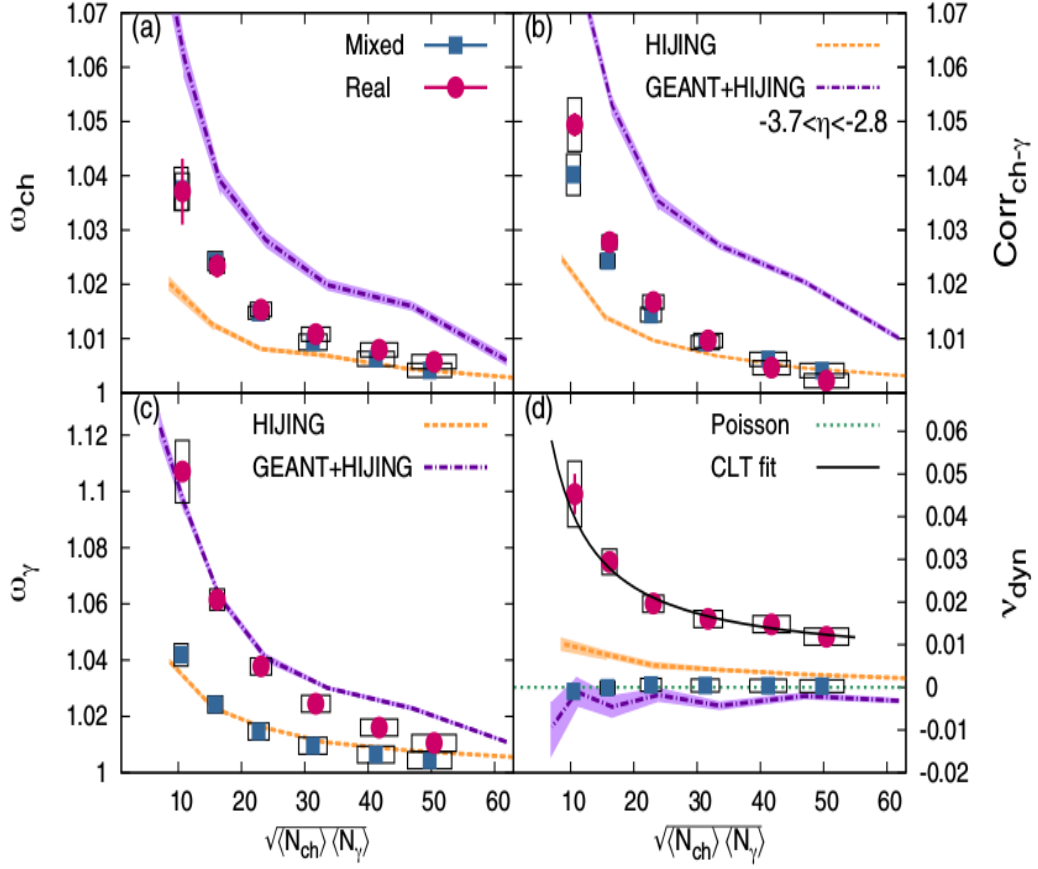


Figure 4.10: The observable  $\nu_{\text{dyn}}$  and the three individual terms plotted as a function of the multiplicity variable in the acceptance of interest  $\sqrt{\langle N_{\text{ch}} N_{\gamma} \rangle}$  at  $\sqrt{s_{NN}} = 200$  GeV. The statistical and systematic uncertainties are represented by vertical lines and boxes respectively. For model calculations, the statistican uncertainties are represented by bands [8].

to the Poissonian limit for most central events while the lower HIJING+GEANT values in the peripheral bins can be attributed to effects of mis-identification of photons [8], which the observable  $\nu_{\text{dyn}}$  is not designed to eliminate. The non-zero positive data values seen for all centralities shows the evidence of the presence of dynamical signals at all centralities and the dissimilarity in trend with the GEANT+HIJING simulation result indicates that it is not due to detector effects [8]. In the experimental setup, there are two FTPC's located on either side of the collision side. The measurements of  $\nu_{\text{dyn}}$  in Fig. 4.11(a) have been done with charged particles and photons measured in the identical pseudorapidity region  $-3.7 < \eta < -2.8$ . This



is known as the measurement on the “same side”. The measurement of photons in the range  $-3.7 < \eta < -2.8$  and charged particles in the range  $2.8 < \eta < 3.7$  is known as the “away side” measurement and is shown in Fig. 4.11(b). The reconstruction efficiency for the FTPC in the pseudorapidity range  $2.8 < \eta < 3.7$  being lower, there is a difference in multiplicity  $\sqrt{\langle N_{\text{ch}} N_{\gamma} \rangle}$  between the two sides, in spite of having the same coverage in  $\eta$ - $\phi$  space.

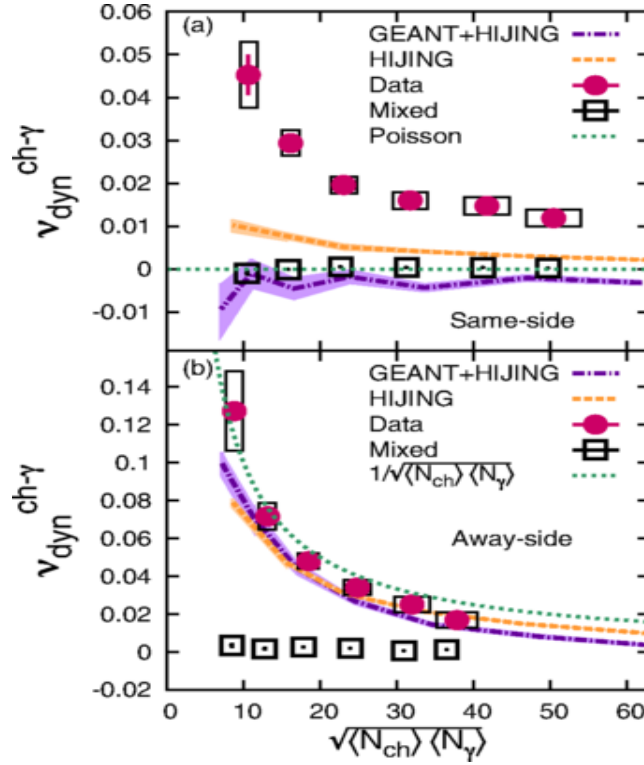


Figure 4.11: Measurement of  $\nu_{dyn}^{\gamma-\text{ch}}$  from charged particles and photons at  $\sqrt{s_{NN}} = 200$  GeV in the same pseudorapidity range  $-3.7 < \eta < -2.8$  (same side) is compared to photons measured in the range  $-3.7 < \eta < -2.8$  and charged particles measured in the range of  $2.8 < \eta < 3.7$  (away-side). Values of  $\nu_{dyn}^{\gamma-\text{ch}}$  measured for the same side are significantly different for data and model calculations, whereas,  $\nu_{dyn}^{\gamma-\text{ch}}$  values for the away side are in good agreement, ruling out detector effects as the reason and hinting strongly at dynamical origin [8].

There is a significant difference between real data and simulation results for the same side which vanishes in the case of the away side. This result bolsters the argument that the difference between real data and model studies as seen in the case of the same side is not a detector effect. The difference observed for the case of same side between the HIJING and HIJING+GEANT

curves quite obviously vanishes when photons and charged particles are measured in different acceptances as the contamination is absent. Any other artefacts related to measurement are taken care of by the robustness of the observable  $\nu_{\text{dyn}}$ . Another thing evident from the away side plot is that data and model seem to follow a universal trend with multiplicity  $\sim 1/\sqrt{\langle N_{\text{ch}} N_{\gamma} \rangle}$ . Taking the away side plot as a reference seems to suggest that the deviation between real data and model seen in the same side is dynamical in origin [8].

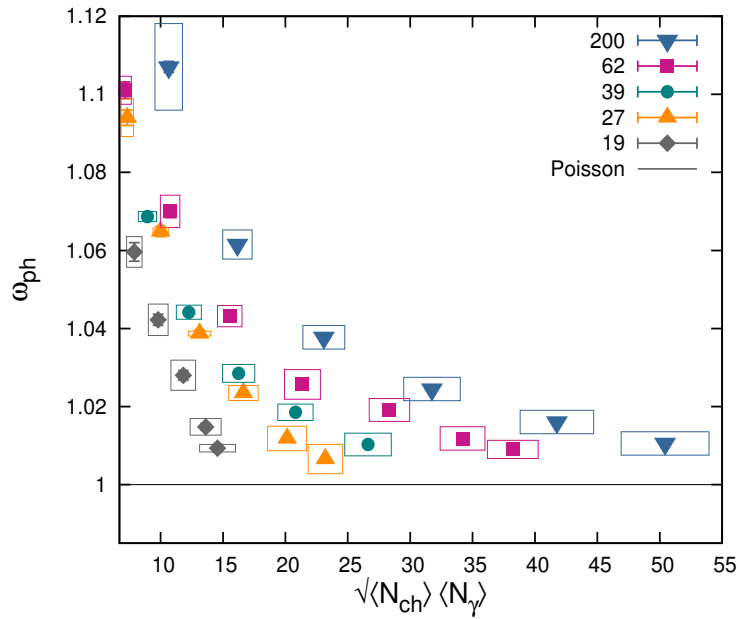


Figure 4.12:  $\omega_{\gamma}$  as a function of multiplicity at all energies ( $\sqrt{s_{NN}} = 200 \text{ GeV} - 19 \text{ GeV}$ ). The statistical error is shown by vertical lines and systematic error is represented by boxes.

Figs 4.12 - 4.14 show a comparison plot of the centrality dependence of the terms  $\omega_{\gamma}$ ,  $\omega_{\text{ch}}$  and  $\text{corr}_{\gamma-\text{ch}}$  at all energies  $\sqrt{s_{NN}} = 200, 62.4, 39, 27$  and  $19 \text{ GeV}$ . Charged particles and photons are measured in the same pseudorapidity coverage  $-3.7 < \eta < -2.8$ . The individual photon and charged particle fluctuation terms,  $\omega_{\gamma}$  and  $\omega_{\text{ch}}$  show a monotonic energy dependence and approach the Poissonian limit (unity) for higher values of multiplicity. The Correlation term  $\text{corr}_{\gamma-\text{ch}}$  shows a weak energy dependence. Compared to the top energy, the fall in the values of the observables  $\omega_{\text{ch}}$ ,  $\text{corr}_{\gamma-\text{ch}}$  and  $\omega_{\gamma}$  at lower energies is quite sharp.

Fig. 4.15 shows the comparison plot of the centrality dependence of the observable  $\nu_{\text{dyn}}^{\gamma-\text{ch}}$

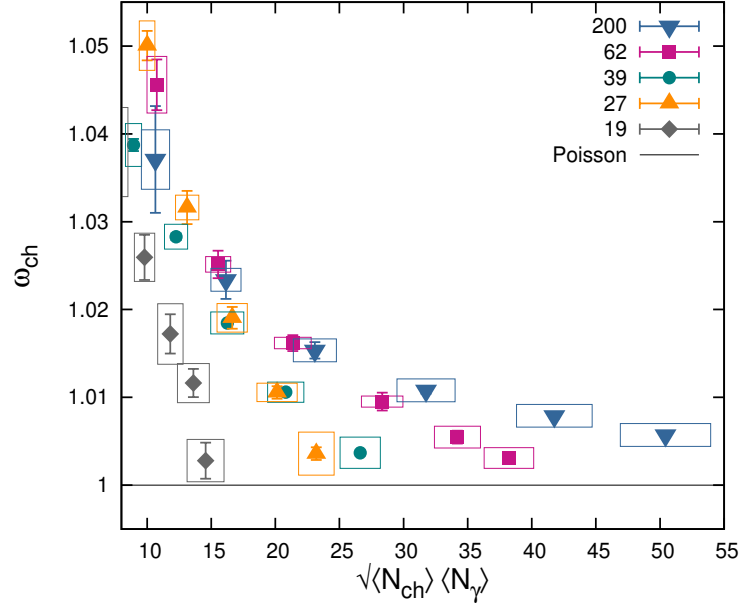


Figure 4.13:  $\omega_{\text{ch}}$  as a function of multiplicity at all energies. The statistical error is shown by vertical lines and systematic error is represented by boxes.

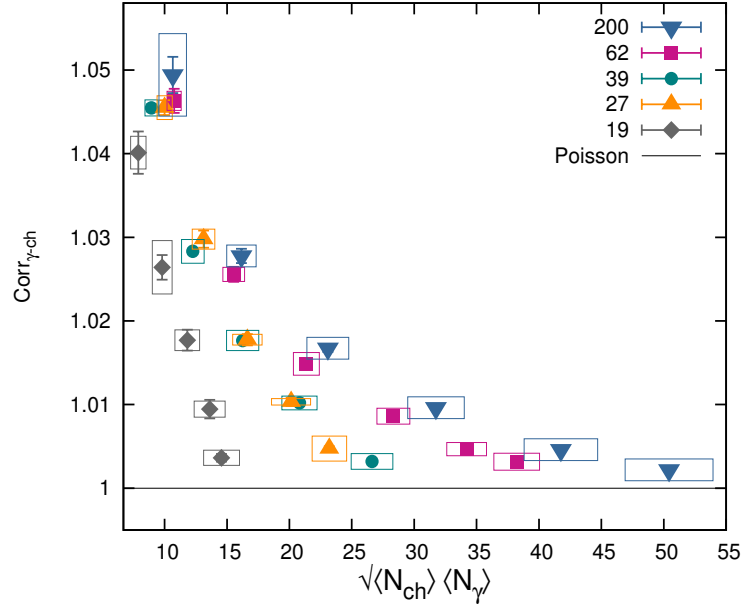


Figure 4.14:  $\text{corr}_{\gamma-\text{ch}}$  as a function of multiplicity at all energies. The statistical error is shown by vertical lines and systematic error is represented by boxes.

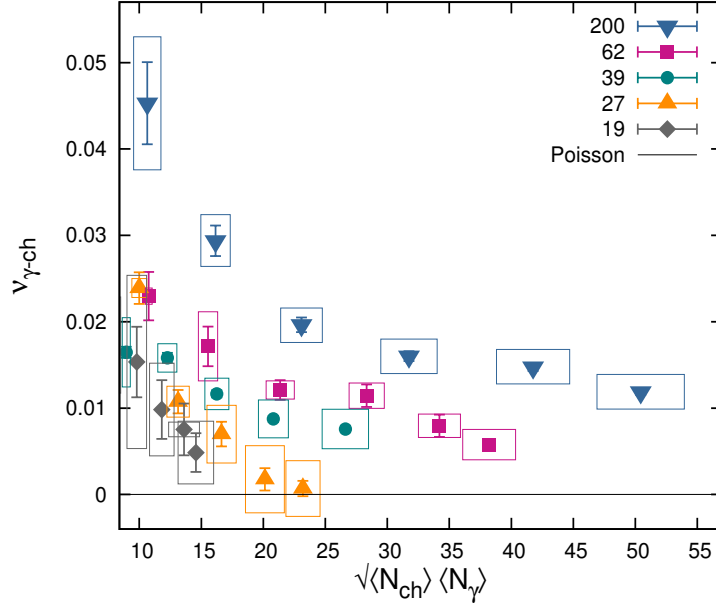


Figure 4.15: A comparison plot of the multiplicity dependence of the observable  $\nu_{dyn}^{\gamma-ch}$  as a function of the multiplicity term  $\sqrt{\langle N_{ch}N_{\gamma} \rangle}$  in the acceptance of interest at all energies. The statistical error is shown by vertical lines and the systematic error is represented by boxes.

at all energies. A non-zero, positive value of  $\nu_{dyn}^{\gamma-ch}$  is observed for all energies at all centralities along with a monotonic decrease with energy. The non-zero  $\nu_{dyn}^{\gamma-ch}$  value could be indicative of the presence of dynamical fluctuations. Although nothing firm can be concluded from the preliminary results obtained for the BES energies, the study of the energy dependence and the consistent non-zero positive signals obtained for all the energies substantiates the belief that the physics origin of the charged-neutral correlation signal is dynamical in nature. It shows that the  $\nu_{dyn}^{\gamma-ch}$  value alongwith all other terms decreases with energy, thereby showing the reduction in dynamical fluctuations.

To understand the dynamics of the ch- $\gamma$  correlation better, we have studied the correlation of positively and negatively charged particles using the observable  $\nu_{dyn}$ . The charge dependence of  $\nu_{dyn}$  has been studied for all energies. The results obtained at the top RHIC energy [8] have been shown in Fig. 4.16. The results obtained for the correlation between different combinations of charged particles and photons are very similar. However, for the combination of positively

and negatively charged particles, the value of the observable  $\nu_{\text{dyn}}^{ch^+-ch^-}$  is different both in sign and in magnitude when compared to  $\nu_{\text{dyn}}^{\gamma\text{-ch}}$ .

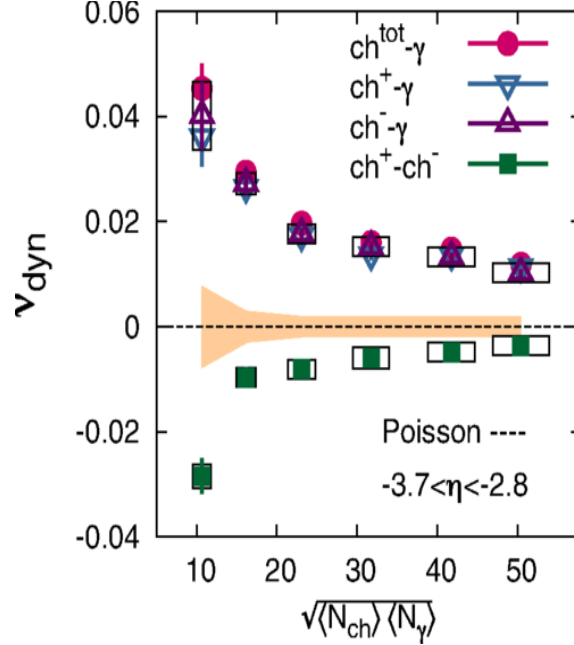


Figure 4.16: Charge dependence of the observable  $\nu_{\text{dyn}}$  at  $\sqrt{s_{NN}} = 200$  GeV as a function of multiplicity. The correlation between the charged particles and photons have been measured using the FTPC and PMD detectors in the pseudorapidity region  $-3.7 < \eta < -2.8$ . The statistical uncertainties have been represented by vertical lines while systematic uncertainties have been represented by boxes [8].

As a consequence of the correlated production of charged particles from neutral resonance decay [8], the large correlation term  $\text{corr}_{ch^+-ch^-}$  leads to negative values of the observable  $\nu_{\text{dyn}}^{ch^+-ch^-}$ . The negative values obtained for  $\nu_{\text{dyn}}$  are in good agreement with previous STAR results at  $\sqrt{s_{NN}} = 200$  for Au+Au collisions at midrapidity [30]. The nature of  $\nu_{\text{dyn}}$  to be negative has also been previously shown in simulation study with a particle production model where resonance decay heavily influences particle production [16]. The difference in the nature of  $\gamma\text{-ch}$  and  $ch^+-ch^-$  correlation clearly indicates that the decay of resonances does not contribute to the dynamical signal obtained for  $\gamma\text{-ch}$  correlation the way it does for  $ch^+-ch^-$  correlation and hints at the existence of a different correlated production mechanism for charged particles

and photons. The decay of resonances ( $\rho^\pm \rightarrow \pi^\pm + \pi^0$  or  $\omega \rightarrow \pi^+ + \pi^- + \pi^0$ ) enhances correlations between charged and neutral particles, but, at the same time possible suppression of this correlation due to the dominance of hadronic rescattering [31][32] processes like meson-meson charge exchange [31] ( $\pi^+ + \pi^- \rightarrow \pi^0 + \pi^0$ ) or baryon-meson reactions [31][32] ( $p + \pi^- \rightarrow n + \pi^0$ ) might be responsible for the nature of the correlation observed for charged and neutral particles.

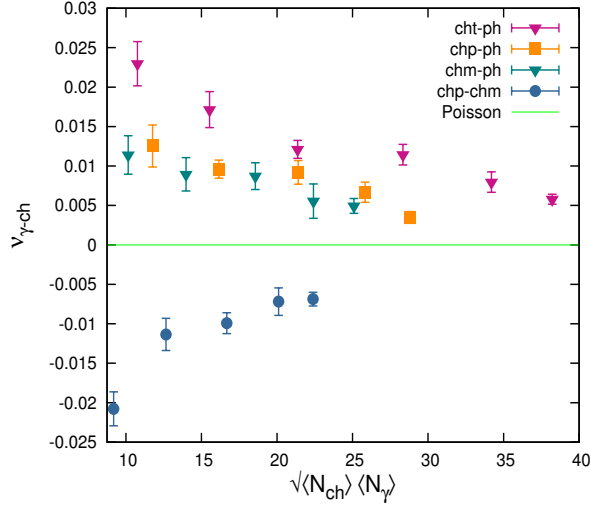


Figure 4.17: Charge dependence of the observable  $\nu_{dyn}$  for  $\sqrt{s_{NN}} = 62$  GeV as a function of multiplicity.

Consistent with observations at the top RHIC energy, the  $ch^+ - ch^-$  correlation is different in sign and magnitude from  $ch-\gamma$  correlation at all energies for all centralities as shown in Figs 4.17 - 4.20, within error bar. The study of the charge dependence of the observable  $\nu_{dyn}$  for the BES energies highlights the fact that charged-neutral correlation and net-charge correlation are different in nature and are influenced by contrasting correlation mechanisms.

The robust observable  $r_{m,1}$  that was introduced by the MiniMax Collaboration enhances our knowledge about charged-neutral correlation by extracting information about deviation of charged-neutral correlation from expectations based on generic production of pions due to isospin symmetry. This observable has a value of unity for the case of generic pion production ( $r_{m,1}^{gen} = 1$ ) as has already been discussed earlier. A deviation from unity in the value of  $r_{m,1}$  would thus be indicative of anomalous pion production, possibly due to the occurrence of DCC-like

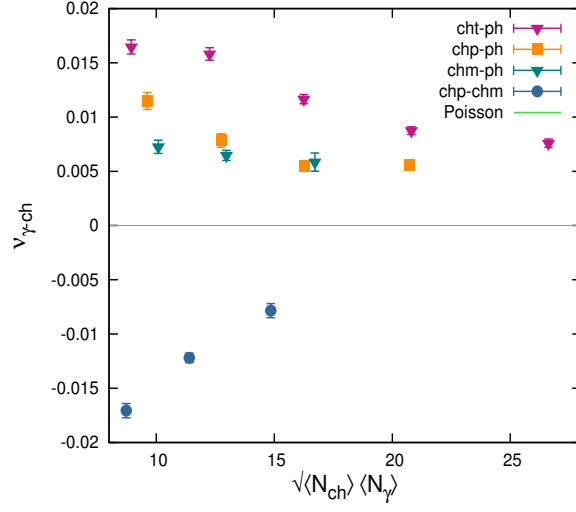


Figure 4.18: Charge dependence of the observable  $\nu_{\text{dyn}}$  for  $\sqrt{s_{NN}} = 39$  GeV as a function of multiplicity.

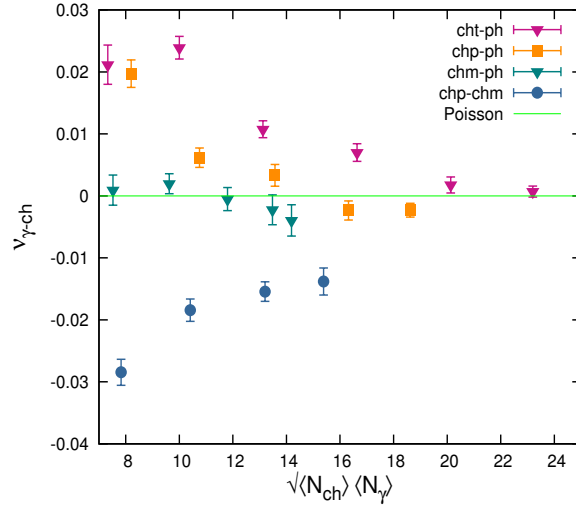


Figure 4.19: Charge dependence of the observable  $\nu_{\text{dyn}}$  for  $\sqrt{s_{NN}} = 27$  GeV as a function of multiplicity.

events. The multiplicity dependence of the first three orders  $r_{1,1}$ ,  $r_{2,1}$ , and  $r_{3,1}$  as a function of  $\sqrt{\langle N_{\text{ch}} N_{\gamma} \rangle}$  at  $\sqrt{s_{NN}} = 200$  GeV have been shown in Fig. 4.21 [8]. The figure shows the variation of  $r_{m,1}$  ( $m = 1 - 3$ ) for real data, mixed events and simulation results using HIJING and GEANT+HIJING. The value of the observable obtained for the HIJING and mixed event

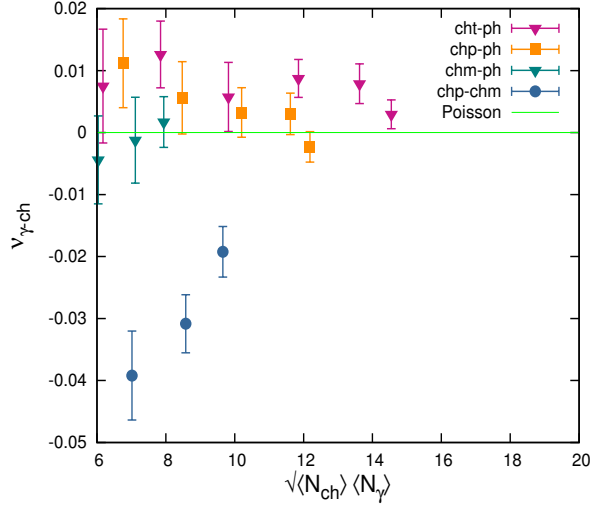


Figure 4.20: Charge dependence of the observable  $\nu_{\text{dyn}}$  for  $\sqrt{s_{NN}} = 19$  GeV as a function of multiplicity.

cases is almost constant for the three cases ( $m = 1-3$ ) and approaches the generic limit. This could essentially highlight similarities in the nature of pion production in the HIJING event generator and the generic case of pion production. Real data and GEANT+HIJING results show a similarity in trends, but, the value of the observable  $r_{m,1}$  at higher centralities is negative for data compared to GEANT+HIJING values, which is always positive. The contamination introduced in the sample when it is passed through GEANT due to detector effects like misidentification is likely responsible for the difference in HIJING and GEANT+HIJING values, which increases for higher orders of  $r_{m,1}$ . The deviation from the generic limit observed in case of data at higher centralities is  $\sim 1\%$  [8]. Fig. 4.22 shows the value of  $r_{m,1}$  plotted as a function of its order  $m$  for most central events within the multiplicity limit of  $47 < \sqrt{\langle N_{\text{ch}} N_{\gamma} \rangle} < 54$ . The trend seen for data is the opposite of model behaviour, showing a deviation  $\sim 1\%$  from generic expectation [8].

The values of the different orders of the robust observable for the BES energies have been calculated and shown in Figs. 4.23 - 4.25. Definitive conclusions cannot be drawn from the preliminary results, other than the fact that the values are close to the generic expectation over the energy range.



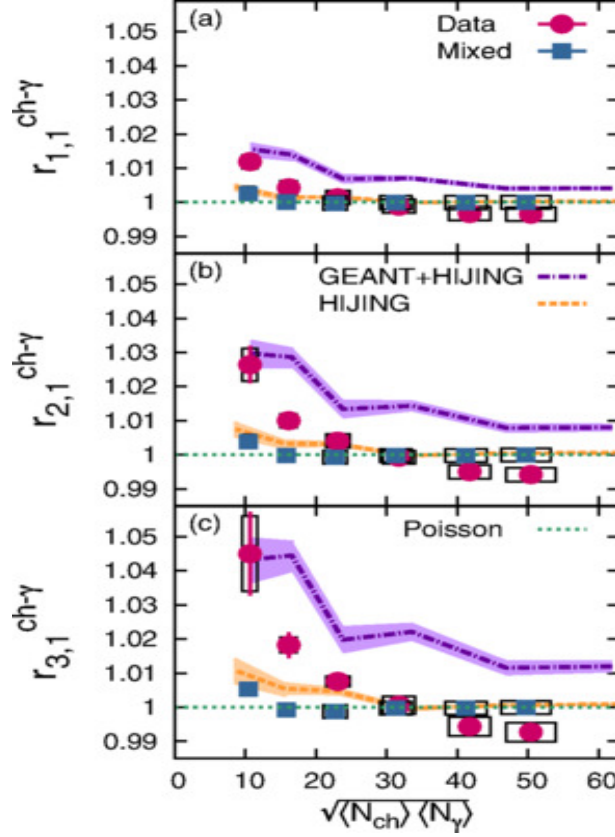


Figure 4.21: The first three orders of the observable  $r_{m,1}$  ( $m = 1 - 3$ ) as a function of multiplicity at  $\sqrt{s_{NN}} = 200$  GeV. Results obtained from real data, mixed-events and simulation results using HIJING and GEANT+HIJING have been compared. Statistical errors are represented by vertical lines and systematic errors are represented by boxes. The statistical errors for simulation results have been represented by bands [8].

## 4.4 Conclusions

The measurement of event-by-event correlations between inclusive charged particle and photon multiplicities at forward rapidity using the detectors, the FTPC and PMD respectively in the common pseudo-rapidity coverage  $-3.7 < \eta < -2.8$  has been discussed in this chapter. The results obtained for the RHIC Beam Energy Scan (BES) energies  $\sqrt{s_{NN}} = 62.4, 39, 27, 19.6$  GeV have been compared with the published results for  $\sqrt{s_{NN}} = 200$  GeV [8]. The measurement of charged-neutral (photon) correlation is a first such attempt at the RHIC energies.  $ch-\gamma$  correlation is heavily influenced by the correlated production of charged and neutral pions and

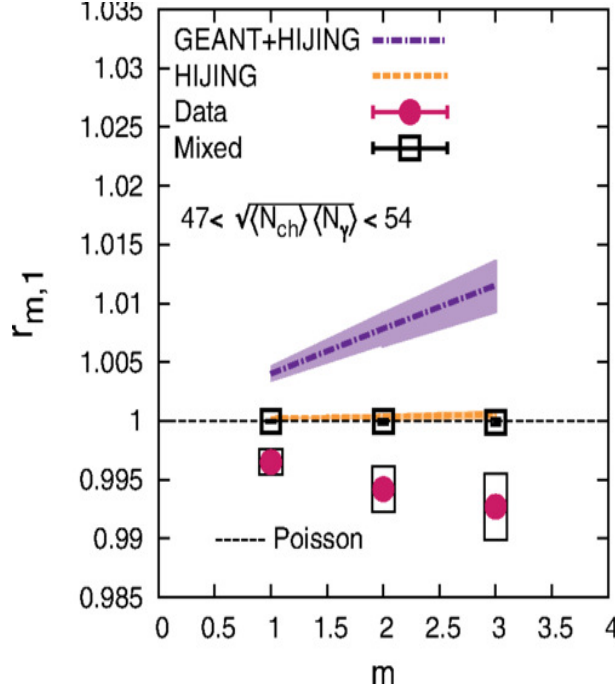


Figure 4.22:  $r_{m,1}$  plotted as a function of its order  $m$  within the multiplicity range  $47 < \sqrt{\langle N_{ch} \rangle \langle N_{\gamma} \rangle} < 54$  compared with mixed events, HIJING and GEANT+HIJING results for  $\sqrt{s_{NN}} = 200$  GeV [8].

the objective of this analysis is to look for manifestations of dynamical physics signals beyond generic expectations for pion production following isospin symmetry. The observables  $\nu_{dyn}$  and  $r_{m,1}$ , created from factorial moments of charged particle and photon multiplicities, designed to study  $ch-\gamma$  correlation have been used for this analysis. The datasets for the analysis have been selected after extensive cleanup. The analysis has been performed in the overlapping PMD-FTPC  $\eta-\phi$  phase space and to take care of the non-uniformity in the detector acceptance, a run-by-run QA has been performed to ensure data quality. The bad run numbers have been extracted by putting a  $2-\sigma$  cut on the averages of quantities related to charged particle and photon multiplicities. Statistical and Systematic uncertainties have been estimated and binwidth correction has been performed. The value of the observable  $\nu_{dyn}^{\gamma-ch}$  at  $\sqrt{s_{NN}} = 200$  GeV has been measured for two distinct scenarios, charged particles and photons measured in the identical  $\eta-\phi$  acceptance ( $-3.7 < \eta < -2.8$ )[same side] and charged particles measured in the acceptance ( $3.7 <$

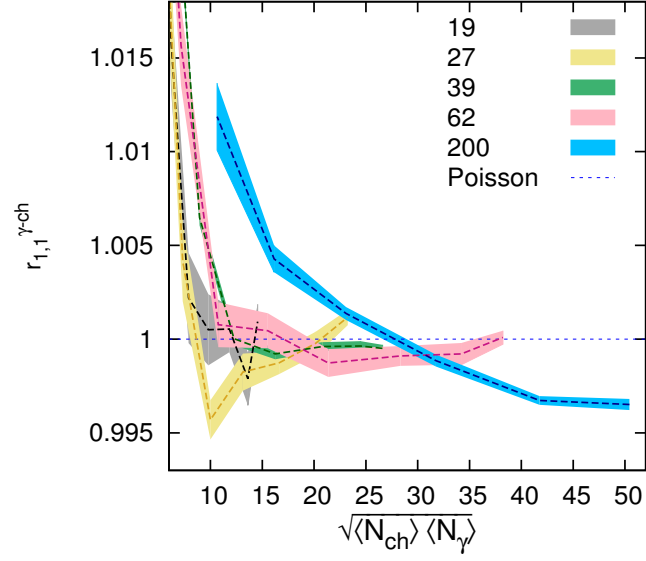


Figure 4.23:  $r_{1,1}$  as a function of multiplicity for the BES energies compared to  $\sqrt{s_{NN}} = 200$  GeV.

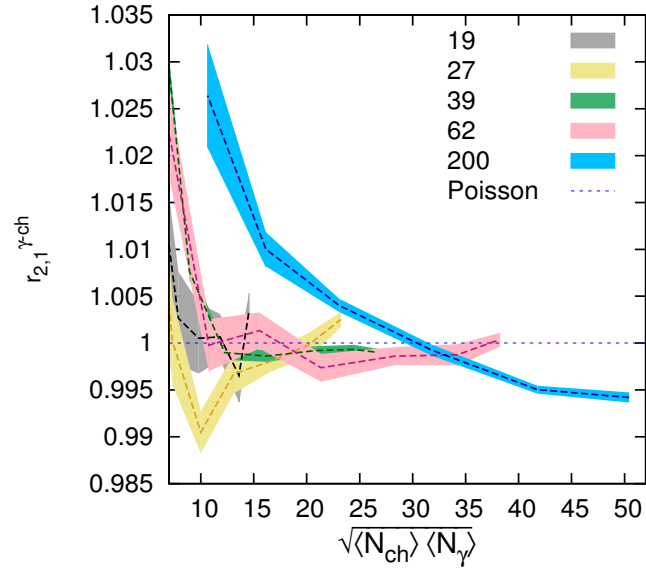


Figure 4.24:  $r_{2,1}$  as a function of multiplicity for the BES energies compared to  $\sqrt{s_{NN}} = 200$  GeV.

$\eta < 2.8$ ) and photons in the acceptance  $(-3.7 < \eta < -2.8)$ [away side]. The  $\nu_{dyn}^{\gamma\text{-ch}}$  value obtained for the same side is non-zero and positive at all centralities beyond model predictions, while

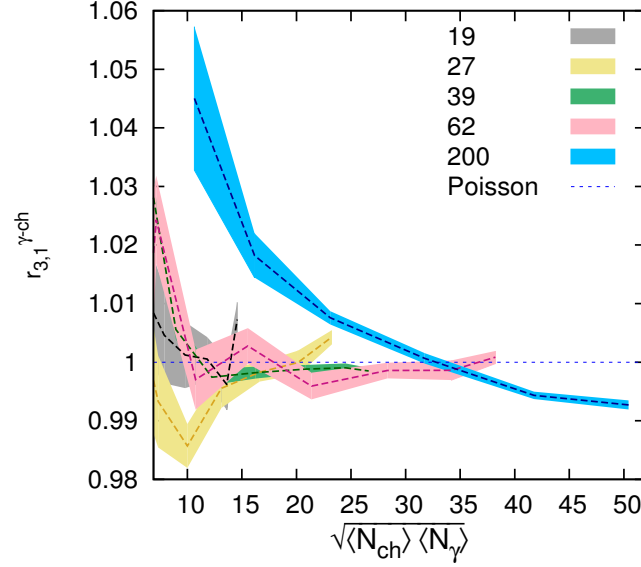


Figure 4.25:  $r_{3,1}$  as a function of multiplicity for the BES energies compared to  $\sqrt{s_{NN}} = 200$  GeV.

no significant deviation in the  $\nu_{dyn}^{\gamma\text{-ch}}$  value from model predictions has been observed for the away side. This is possibly indicative of the fact that signals of ch- $\gamma$  correlation are dynamical in origin [8]. The study of the centrality dependence of the  $\nu_{dyn}^{\gamma\text{-ch}}$  observable reveals an  $A + B/\sqrt{\langle N_{\text{ch}} N_{\gamma} \rangle}$  dependence as per Central Limit Theorem (CLT) predictions [8].  $\nu_{dyn}^{\gamma\text{-ch}}$  shows an energy dependence for the BES energies and is non-zero and positive for all centralities and all energies. As we go down to lower energies ( $\sqrt{s_{NN}}$ ), the fall in the value of  $\nu_{dyn}$  as a function of multiplicity is very sharp. In order to understand ch- $\gamma$  correlation dynamics better, the correlation between positively and negatively charged particles measured in the same acceptance has also been studied. The  $\nu_{dyn}^{ch^+-ch^-}$  term is qualitatively and quantitatively different from  $\nu_{dyn}^{\gamma\text{-ch}}$ , in sign and magnitude [8]. The negative values of  $\nu_{dyn}^{ch^+-ch^-}$  can be attributed to the large  $\text{corr}_{ch^+-ch^-}$  term arising due to correlated production of charged particles from resonance decays. The difference in the nature of the values of the observable  $\nu_{dyn}$  for the two cases emphasises on different production mechanisms for positively and negatively charged particles and charged particles and photons. While there is a predominance of decay correlation in case of net-charge

correlation,  $\text{ch-}\gamma$  correlation seems to be influenced by hadronic rescattering processes [8]. The charge dependence of the observable  $\nu_{\text{dyn}}$  has been studied at the BES energies and the results obtained are consistent with observation at the top RHIC energy. Correlations between different combinations of charged particles and photons yield results different in sign and magnitude from correlations between positively and negatively charged particles at all energies. The robust or the MiniMax observable  $r_{m,1}$  that has been used in this analysis is specially designed to highlight differences arising in  $\text{ch-}\gamma$  correlation beyond expectations from the isospin symmetry dominated generic production of charged and neutral pions. The centrality dependence of the first three orders of the observable  $r_{m,1}$  at  $\sqrt{s_{NN}} = 200$  GeV indicates an opposite trend to model calculations and its value at higher centralities is lower than the generic expectation ( $r_{m,1}^{\text{gen}} = 1$ ) [8]. In the multiplicity limit of  $47 < \sqrt{\langle N_{\text{ch}} N_{\gamma} \rangle} < 54$  for most central events, the value of  $r_{m,1}$  plotted versus its order  $m$  indicates a slight deviation, less than 1% from expectation based on generic pion production [8]. Results obtained using the  $r_{m,1}$  observable for the BES energies is close to the Poissonian/generic (unity) limit and inconclusive as far as any deviation from generic pion production expectation is concerned.

# Bibliography

- [1] J. Adams et al. [STAR Collaboration], Phys. Rev. Lett. 95, 062301 (2005).
- [2] J. D. Bjorken, in In Conclusion (World Scientific, Singapore, 2003), Chp. 28, pp. 395–406.
- [3] J. P. Blaizot and A. Krzywicki, Phys. Rev. D 46, 246 (1992).
- [4] K. Rajagopal and F. Wilczek, Nucl. Phys. B 399, 395 (1993).
- [5] K. Rajagopal, in Quark-Gluon Plasma 2 (World Scientific, Singapore, 1995), Chp 9, pp. 484–554.
- [6] P. Tribedy, PhD. Thesis, Homi Bhabha National Institute, India, 2014.
- [7] P. Tribedy et al. Phys. Rev. C 85, 024902 (2012). [arXiv:1108.2495 [nucl-ex]]
- [8] P. Tribedy et al. [STAR Collaboration], Phys. Rev. C 91, 034905 (2015).
- [9] K. H. Ackermann et al., Nucl. Instrum. Methods Phys. Res., Sect. A 499, 624 (2003).
- [10] M. Anderson et al., Nucl. Instrum. Methods Phys. Res., Sect. A 499, 659 (2003)
- [11] M. Beddo et al., Nucl. Instrum. Methods Phys. Res., Sect. A 499, 725 (2003).
- [12] R. Bellwied, S. Gavin and T. Humanic, nucl-th/9811085.
- [13] K. H. Ackermann et al., Nucl. Instrum. Methods Phys. Res., Sect. A 499, 713 (2003).

- [14] M. M. Aggarwal et al., Nucl. Instrum. Methods Phys. Res., Sect. A 499, 751 (2003); Nucl. Instrum. Methods Phys. Res., Sect. A, 488, 131 (2002).
- [15] T. C. Brooks et al. [MiniMax Collaboration], Phys. Rev. D 61, 032003 (2000); T. C. Brooks et al. [MiniMax Collaboration], Phys. Rev. D 55, 5667 (1997) [arXiv:hep-ph/9609375].
- [16] C. Pruneau, S. Gavin and S. Voloshin, Phys. Rev. C 66, 044904 (2002) [arXiv:nucl-ex/0204011].
- [17] B. I. Abelev et al. [STAR Collaboration], Phys. Rev. Lett. 103, 092301 (2009) [arXiv:0901.1795 [nucl-ex]].
- [18] S. M. Dogra [STAR Collaboration], J. Phys. G 35, 104094 (2008).
- [19] S. A. Voloshin, V. Koch and H. G. Ritter, Phys. Rev. C 60, 024901 (1999) [nucl-th/9903060].
- [20] P. Christiansen et al. Phys. Rev. C 80, 034903 (2009). [arXiv:0902.4788 [hep-ex]].
- [21] T. A. Trainor, [hep-ph/0001148].
- [22] X. F. Luo, B. Mohanty, H. G. Ritter and N. Xu, J. Phys. G 37, 094061 (2010) [arXiv:1001.2847 [nucl-ex]].
- [23] B. Mohanty and J. Serreau, Phys. Rept. 414, 263 (2005) [arXiv:hep-ph/0504154].
- [24] X. Luo, J. Xu, B. Mohanty, and N. Xu, J. Phys. G 40, 105104 (2013).
- [25] J. Adams et al. (STAR Collaboration), Phys. Rev. C 73, 034906 (2006).
- [26] H. Masui and A. Schmah, “StRefMultCorr”, (2011).
- [27] L. Adamczyk et al. (STAR Collaboration), Phys. Rev. Lett. 112, 032302 (2014).
- [28] L. Adamczyk et al. (STAR Collaboration), Phys. Rev. Lett. 113, 092301 (2014).
- [29] B. Efron, SIAM Rev. 21, 460 (1979).

- [30] B. I. Abelev et al. (STAR Collaboration), Phys. Rev. C 79, 024906 (2009)
- [31] S. Jeon and V. Koch, Phys. Rev. Lett. 83, 5435 (1999).
- [32] M. Kitazawa and M. Asakawa, Phys. Rev. C 85, 021901 (2012).



## Chapter 5

# Results and Discussions

It is widely believed that primordial matter that was existent at the earliest stages of the creation of the Universe, less than a few microseconds after the Big Bang can be created experimentally in relativistic heavy ion collisions under extreme conditions of temperature and energy density. The Relativistic Heavy Ion Collider at BNL, USA has undertaken heavy-ion, proton-proton and proton-ion collisions for the past 15 years to create and investigate the new phase of de-confined matter commonly referred to as the Quark Gluon Plasma (QGP). This new state of strongly interacting matter is characterised by asymptotically free quarks and gluons. The measurements at RHIC over the last few years have set forward conclusive evidences towards the formation of QGP. The STAR (Solenoidal Tracker at RHIC) experiment at RHIC is designed to search for the existence of the QGP and to explore its properties. Experimentally, this new state of matter is studied via the detection of the products of heavy-ion collisions. Suitable observables constructed from the different properties of the particles detected are used to understand the underlying mechanisms. This thesis work is mainly aimed at probing the matter created at RHIC heavy-ion collisions using di-muons and photons at mid and forward rapidities. This work is partly focussed on fabricating and testing Multi-gap Resistive Plate Chambers (MRPC) for the Muon Telescope Detector (MTD) upgrade of the STAR experiment at midrapidity, whose objective is to detect muons using excellent timing and position resolution of the MRPC's. This

thesis work has also emphasized on studying the correlation between charged particles and photons measured in the common  $\eta - \phi$  phase space of the two forward detectors at STAR, the Forward Time Projection Chamber (FTPC) and the Photon Multiplicity Detector (PMD), respectively, at a wide range of Au+Au collision energies. This work is performed to search for possible evidences of the QCD chiral phase transition from the QGP phase to the Hadronic Gas (HG) phase.

## 5.1 Fabrication and testing of Multi-gap Resistive Plate Chambers (MRPC) for the STAR-MTD project

The Muon Telescope Detector(MTD) installed at mid-rapidity at STAR wishes to probe the new state of matter created in RHIC heavy-ion collisions characterised by partonic degrees of freedom referred to as the Quark Gluon Plasma (QGP), by studying the di-muon spectra at different mass regimes. Data taken by the MTD detector will help the scientific community to understand the elementary properties of the QGP such as the temperature and color screening aspects [1][2]. The MTD is a large area detector that has a pseudorapidity coverage of  $|\eta| < 0.5$  and an azimuthal coverage of  $\sim 45\%$  [3]. It is located at a distance of  $\sim 400$  cm from the STAR interaction point. In order to meet the desired physics goals, the MTD relies on clean muon identification and triggering using precise timing and hit position measurement and hence uses the inexpensive and reliable MRPC technology, well known for its excellent timing and spatial resolution. The gas-tight Aluminium trays that enclose the MTD-MRPC's are specifically mounted on the PMT boxes of the STAR-BEMC detector behind the steel backlegs of the STAR magnet to achieve excellent hadron rejection. The fabrication of the large-sized, 5-gap glass MRPC modules of dimensions  $87 \text{ cm} \times 58 \text{ cm}$  having  $250 \text{ }\mu\text{m}$  gas gaps defined by Nylon monofilament fishing lines was the responsibility of two Chinese institutes (Tsinghua University and USTC) and VECC, Kolkata. The materials for detector fabrication were sent to VECC by the Chinese Institutes to ensure uniformity. 10 MTD-MRPC modules that make up

$\sim 10\%$  of the total modules installed at STAR from the year 2011 to 2014 have been fabricated and tested successfully at VECC. The modules have been tested in the Avalanche mode with a gas mixture of Freon (R134A) and Isobutane ( $i\text{-C}_4\text{H}_{10}$ ) in the ratio 95 : 5 and operated at a voltage of  $\pm 6300$  Volts ( $\sim 100$  kV/cm). Double-ended PCB pickup strips of size 3.8 cm, with an inter-strip separation of 0.6 cm are used to read-out detector signals. Each of the 10 modules has been seasoned and data taken for I-V characteristic, efficiency and noise rate. Modules are finally shipped to UT Austin, USA for further tests. The timing and spatial resolution of the MTD-MRPC's have been measured at STAR using cosmic ray muons. The average transverse momentum ( $p_T$ ) of muons traversing through the detectors is 6 GeV/c and contribution due to multiple scattering of the muons in the material budget of the STAR detector is negligible [3]. Hence the muons serve as clean triggers for the MTD-MRPC's and a timing resolution of  $\sim 100$  ps and a spatial resolution of  $\sim 1\text{-}2$  cm has been measured [3].

## 5.2 Charged-neutral ( $\gamma$ ) correlation analysis for the STAR experiment

During the transition from the chirally symmetric Quark Gluon Plasma [4–7] phase to the symmetry broken Hadronic gas phase in heavy-ion collisions, the medium undergoes a chiral phase transition [4–7]. The signature of a phase transition is an enhancement in the fluctuations of conserved quantities. The charged-to-neutral pion ratio is influenced by the chiral phase transition and dynamical fluctuations of this observable can be used as a suitable probe to study this phase transition [8–11]. The detection of charged and neutral particles in high energy experiments is predominantly in the form of charged ( $\pi^\pm$ ) and neutral pions ( $\pi^0$ ) [12] respectively. Neutral particles detected experimentally are primarily in the form of photons coming from the decay of neutral pions. Therefore, the actual observable used to study chiral phase transition is the correlation between charged particles and photons. Pions of different isospins are produced in equal abundances in heavy-ion collisions due to isospin symmetry. It is theoretically predicted

that during chiral phase transition, the rapid cooling of the evolving system can create metastable domains of Disoriented Chiral Condensates (DCC) [8–11]. The decay of these domains of DCC can lead to anomalous production of pions of a particular isospin which leads to modifications of the neutral pion fraction distribution, differing vastly from the case of generic pion production [9][11]. The manifestation of this anomaly in pion production is in the form of an anti-correlation between the multiplicities of charged and neutral pions [10]. In the context of Au+Au collisions at the STAR experiment, the analysis of charged-neutral(ch- $\gamma$ ) correlation is unique and has never been done before. Correlations between inclusive charged particle and photon multiplicities has been measured event-by-event at the forward rapidity using the FTPC and PMD detectors to simultaneously measure charged particles and photons respectively. The analysis has been done for Au+Au collisions at the RHIC Beam Energy Scan (BES) energies  $\sqrt{s_{NN}} = 62.4, 39, 27, 19.6$  GeV in the common PMD-FTPC pseudo-rapidity coverage  $-3.7 < \eta < -2.8$ . The published results for ch- $\gamma$  correlation at  $\sqrt{s_{NN}} = 200$  GeV [13] have been discussed and a comparative study has been done for all the energies. The observables  $\nu_{dyn}$  and  $r_{m,1}$  specially designed for the study of ch- $\gamma$  correlation have been used in this analysis. The datasets for the respective energies have been selected after detailed quality assurance checks and after applying requisite kinematic cuts. The observable  $\nu_{dyn}^{\gamma-ch}$  at  $\sqrt{s_{NN}} = 200$  GeV yields a non-zero, positive value at all centralities beyond predictions from model calculations, when charged particle and photon multiplicities are measured in the identical pseudorapidity coverage  $-3.7 < \eta < -2.8$ . In the scenario of charged particle multiplicity measurement using the FTPC in the pseudorapidity coverage  $3.7 < \eta < 2.8$  and photon multiplicity measurement using the PMD in the pseudorapidity coverage  $-3.7 < \eta < -2.8$ , yields a  $\nu_{dyn}^{\gamma-ch}$  value that has no significant deviation from from model calculations. The results obtained at the top RHIC energy thus possibly indicate that the origin of the signals of ch- $\gamma$  correlation are dynamical in nature [13]. As per predictions of the Central Limit Theorem (CLT) the data at  $\sqrt{s_{NN}} = 200$  GeV has a centrality dependence of the form  $A + B/\sqrt{\langle N_{ch} N_{\gamma} \rangle}$  for the  $\nu_{dyn}^{\gamma-ch}$  observable [13]. Calculation of the observable  $\nu_{dyn}^{\gamma-ch}$  for the BES energies reveals an energy dependence and the observable is non-zero and positive for

all centralities at all energies. There is a sharp fall in the value of  $\nu_{dyn}^{\gamma-\text{ch}}$  with multiplicity at the lower energies. The comparison of the ch- $\gamma$  and the net-charge correlations studied in the same geometric detector acceptance provides a clearer picture of the nature of the ch- $\gamma$  (anti-)correlation signal. Since net-charge correlation is heavily influenced by the correlated production of oppositely charged particles from the decay of resonances, the value of  $\nu_{dyn}^{ch^+-ch^-}$  is negative due to the large  $\text{corr}_{ch^+-ch^-}$  term.  $\nu_{dyn}^{\gamma-\text{ch}}$  is completely different from  $\nu_{dyn}^{ch^+-ch^-}$  in sign and magnitude [13] and this difference can be attributed to their respective production mechanisms. While net-charge correlation is dominated by resonance decay, ch- $\gamma$  correlation seems to be influenced by hadronic rescattering [13]. A study of the charge dependence of the observable  $\nu_{dyn}$  at the BES energies shows consistency with the results obtained at 200 GeV and results obtained for different combinations of charged particles and photons are different in sign and magnitude compared to the combination of positively and negatively charged particles at all energies. The robust or the MiniMax observable  $r_{m,1}$  is well-suited to study the occurrence of DCC phenomena as it indicates noticeable deviations from generic case of pion production in the results obtained for ch- $\gamma$  correlation, if any. The value of  $r_{m,1}$  obtained is close to the Poissonian/generic (unity) limit over the BES energy range. At  $\sqrt{s_{NN}} = 200$  GeV, the centrality dependence of the observable  $r_{m,1}$  has been studied and the first three orders  $r_{1,1}$ ,  $r_{2,1}$  and  $r_{3,1}$  reveal a trend opposite to model calculations. At higher centralities, all three terms have values lower than unity which is the generic limit of the observable [13]. A deviation from generic expectation less than 1% is obtained when  $r_{m,1}$  is plotted as a function of its order  $m$  for most central events within the multiplicity limit  $47 < \sqrt{\langle N_{\text{ch}} N_{\gamma} \rangle} < 54$  [13]. No conclusive evidences have been found from the results obtained using the  $r_{m,1}$  observable for the BES energies.  $r_{1,1}$ ,  $r_{2,1}$  and  $r_{3,1}$  all have values close to the Poissonian/generic limit (unity) over the BES energy range.

### 5.3 Use of MRPC for TOF-PET (Time-of-Flight Positron Emission Tomography)

As a spin-off benefit of the Detector R&D for STAR, efforts have been undertaken to build prototype MRPC detectors and test the feasibility of MRPC's for medical imaging applications. Positron Emission Tomography (PET) is one such biomedical imaging technique that can benefit from advancements in detector technology to enhance the existing techniques of detection. In this particular modality, a radiopharmaceutical (e.g FDG, Fluorodeoxyglucose) labelled with a positron emitter ( $^{18}\text{F}$ ) are administered into the object of study. After traversing a short path length, the positron annihilates with an electron of the medium and emits a pair of collinear 511 keV photons travelling in opposite direction due to momentum conservation. The coincident detection of the photon pair in a certain time window establishes the occurrence of the annihilation event along the Line of Response (LOR), the line connecting the two detection events. The LOR events for all possible angles are collected to enable the reconstruction of three-dimensional tomographic images. The availability of the Time-of-Flight information helps in the image reconstruction procedure. The localisation of the annihilation event to a smaller region on the LOR results in less noise propagation and random coincidences, thus improving the signal to noise ratio and the image quality. The localisation accuracy achievable in case of a TOF-PET system which influences the sensitivity of the measurement, is a function of the detector timing resolution. Multigap Resistive Plate Chambers (MRPC) are being used around the world for the detection of charged particles and are well-known for their excellent timing and position resolution. The major drawback of the MRPC detectors is their low gamma-detection efficiency, which if we manage to overcome, will make MRPC's excellent alternatives to the expensive scintillator-based PET systems currently being used. Extensive research is being carried out worldwide to explore the feasibility of MRPC's in TOF-PET systems. A 6-gap MRPC prototype [14] fabricated with 600  $\mu\text{m}$  float glass plates and a gas gap of 200  $\mu\text{m}$  defined with polycarbonate spacers has been tested. The detector has been tested with a positron emitting

$^{22}\text{Na}$  source in the Avalanche mode with a Freon (R134A) and Isobutane ( $\text{i-C}_4\text{H}_{10}$ ) gas mixture in the ratio 95 : 5. The pair of anti-parallel 511 keV photons emitted by the source created via positron-electron annihilation have been detected by a coincidence set-up of the 6-gap MRPC and a plastic scintillator of  $5\text{ cm} \times 1.2\text{ cm}$  dimensions. The measurement has been performed with source and non-source configurations to remove cosmic muon background. The contribution due to the source was clearly distinguishable by the detection of photon pairs above background [15]. A photon detection efficiency of 0.9% is obtained at the operating voltage of 15kV [15] which is comparable to values existing in literature [16][17]. An effort was made to locate the position of the source using coincident timing distribution measurement of the MRPC and the scintillator and comparing the value obtained with simple calculations using known distances and the photon velocity. Given the large error bars in the measurement, the measured and calculated values showed a similar trend [15]. A coincidence set-up has been built with two  $18\text{ cm} \times 18\text{ cm}$ , 5-gap glass MRPC prototypes having a gas gap of  $250\text{ }\mu\text{m}$ , using nearly similar materials and following identical detector technology as the MTD MRPC's. The two-MRPC set-up, due to better timing resolution is expected to improve the sensitivity of the TOF-PET system towards the coincident detection of 511 keV photon pairs compared to what is achievable with the existing scintillator - MRPC system. The prototypes have been characterised via cosmic rays and a timing resolution of  $\sim 120\text{ ps}$  at the operating voltage of 15.8 kV has been obtained.

# Bibliography

- [1] STAR Muon Telescope Detector Proposal:  
[http://www.star.bnl.gov/~ruanlj/MTDreview2010/MTD\\_proposal\\_v14.pdf](http://www.star.bnl.gov/~ruanlj/MTDreview2010/MTD_proposal_v14.pdf).
- [2] L. Ruan et al., J. Phys. G 36, 095001 (2009).
- [3] C. Yang et al for the STAR Collaboration, Calibration and performance of the STAR Muon Telescope Detector using cosmic rays, Nucl. Instrum. Meth. A 762 (2014) 1.
- [4] J. Adams et al. (STAR Collaboration), Nucl. Phys. A 757, 102 (2005).
- [5] B. B. Back et al. (PHOBOS Collaboration), Nucl. Phys. A 757, 28 (2005).
- [6] K. Adcox et al. (PHENIX Collaboration), Nucl. Phys. A 757, 184 (2005).
- [7] I. Arsene et al. (BRAHMS Collaboration), Nucl. Phys. A 757, 1 (2005).
- [8] J. D. Bjorken, in In Conclusion (World Scientific, Singapore, 2003), Chap. 28, pp. 395–406.
- [9] J. P. Blaizot and A. Krzywicki, Phys. Rev. D 46, 246 (1992).
- [10] K. Rajagopal and F. Wilczek, Nucl. Phys. B 399, 395 (1993).
- [11] K. Rajagopal, in Quark-Gluon Plasma 2 (World Scientific, Singapore, 1995), Chap 9, pp. 484–554.
- [12] J. Adams et al. [STAR Collaboration], Phys. Rev. Lett. 95, 062301 (2005).



- [13] P. Tribedy et al. [STAR Collaboration], Phys. Rev. C 91, 034905 (2015).
- [14] A. Banerjee et al., Nucl. Instrum. Meth. A. 718 (2013) 138.
- [15] A. Roy et al., 2014 JINST 9 C10030.
- [16] F. Sauli et al., Nuclear Instruments and Methods in Physics Research A 778 (2015) 85–91.
- [17] P. Fonte et al., Nucl. Instrum. Meth. A. 602 (2009) 780.